Unraveling the Weddell Gyre: Exploring its dynamics and influence on Southern Ocean ventilation

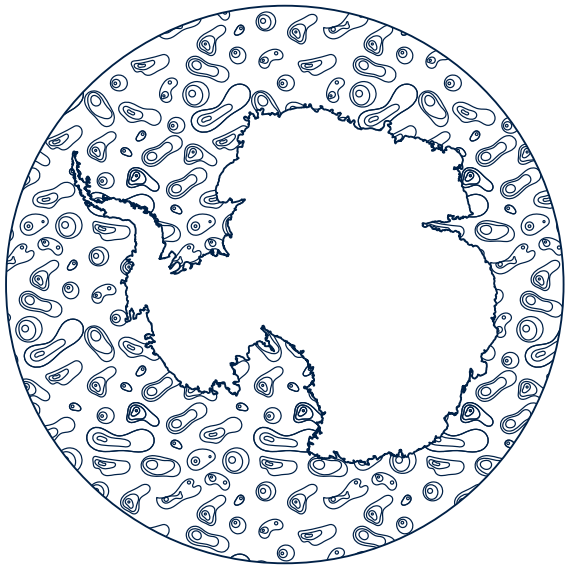

Andrew Styles

Linacre College

University of Oxford

A thesis submitted for the degree of

Doctor of Philosophy

Trinity 2023

Acknowledgements

Straight out of the gate I would like to thank my two incredible supervisors, David and Mike, for their guidance and support. Because of them, every step of the DPhil journey has been an intriguing opportunity to explore and learn. I must also thank Graeme MacGilchrist for an enjoyable collaboration and his words of wisdom on Lagrangian trajectories. Thank you to David Storkey, Andrew Coward, and Julian Mak for their insight into the weird, wonderful, and sometimes frustrating world of ocean modelling. Going back in time to secondary school, I would like to thank Deborah Mouat for teaching me that science is something to take seriously and Philip Shepherd for showing me that science can also be very funny.

Behind the scenes I have been supported by incredible friends from the Environmental Research DTP. In particular, I would like to thank Tim Hempel, Edmund Derby, Emily Van de Koot, Matt Sutton, and Andrew Williams for putting up with my antics. The biggest thanks of all must go to my parents and my brother, I do not know where I would be without their love and support.

Abstract

The Southern Ocean is an area of great importance when considering anthropogenic climate change but also an area of great uncertainty. Between climate projections, the Southern Ocean is where one finds the most disagreement in both heat and carbon uptake. The Weddell Gyre is the largest coherent circulation south of the Antarctic Circumpolar Current (ACC) and mediates the transport of water to and from the Antarctic shelf. Here we use a diverse range of methods to study the dynamics of the Weddell Gyre and its role in Southern Ocean ventilation.

An idealized model of the Weddell Gyre and the ACC is used to investigate the gyre's sensitivity to mesoscale eddies. The gyre is particularly strong at eddy-permitting resolutions (45 Sv with a noisy bathymetry) and weakest at eddy-parameterized resolutions (12 Sv). Simulations with partially resolved eddies have the largest horizontal density gradients. The steep isopycnals intensify the gyre's thermal wind transport and fuel tall columns of eddy kinetic energy which excite the gyre circulation at the sea floor.

The vorticity budget of a realistic Weddell Gyre simulation is calculated to identify important forces for the circulation. The gyre's vorticity budget is dominated by a spurious component of the Coriolis force which emerges from the C-grid geometry. We identify two topographic and two non-topographic components of the spurious force. The topographic components can be mitigated by using a terrain-following coordinate and all components vanish when the B-grid is adopted.

Backwards-in-time trajectories are used to identify spatial and temporal patterns of Southern Ocean ventilation on a thirty-year timescale. Practically all ventilation occurs between August and November. Sites of deep convection are responsible for 60% of open ocean ventilation. Almost no ventilation occurs within the subpolar gyres but their western boundary currents are the primary export pathway for shelf-ventilated water.

Contents

x

List of Abbreviations

AABW . . . . Antarctic Bottom Water

ACC . . . . . Antarctic Circumpolar Current

ASC . . . . . Antarctic Slope Current

ASF . . . . . Antarctic Slope Front

CDW . . . . . Circumpolar Deep Water

CMIP . . . . . Coupled Model Intercomparison Project

CMIP5 . . . . Phase 5 of the Coupled Model Intercomparison Project

CMIP6 . . . . Phase 6 of the Coupled Model Intercomparison Project

EEN . . . . . The energy and enstrophy conserving scheme for calculating the Coriolis acceleration described by Arakawa and Lamb (1981)

ENE . . . . . The energy conserving scheme for calculating the Coriolis acceleration described by Sadourny (1975)

ENS . . . . . The enstrophy conserving scheme for calculating the Coriolis acceleration described by Sadourny (1975)

GM . . . . . The eddy parameterization described by Gent and McWilliams (1990)

GCM . . . . . General circulation model

JEBAR . . . . Joint effect of baroclinicity and relief

MOC . . . . . Meridional overturning circulation

SAM . . . . . Southern Annular Mode

1 Introduction

Contents

1.1 The Southern Ocean and subpolar gyres

The Southern Ocean is responsible for approximately half of the ocean's uptake of CO_2 (Gruber et al., 2009; Khatiwala et al., 2013; Sabine et al., 2004) and 40-100% of the excess heat absorbed by the ocean (e.g. Cheng et al., 2022; Frölicher et al., 2015; Meredith et al., 2022). From these two statements we can see that the Southern Ocean is an area of great importance when considering anthropogenic climate change but also an area of great uncertainty. Between CMIP5 climate projections (phase 5 of the Coupled Model Intercomparison Project), the Southern Ocean is where one finds the most disagreement in both heat and carbon uptake (Canadell et al., 2021; Fox-Kemper et al., 2021; Frölicher et al., 2015).

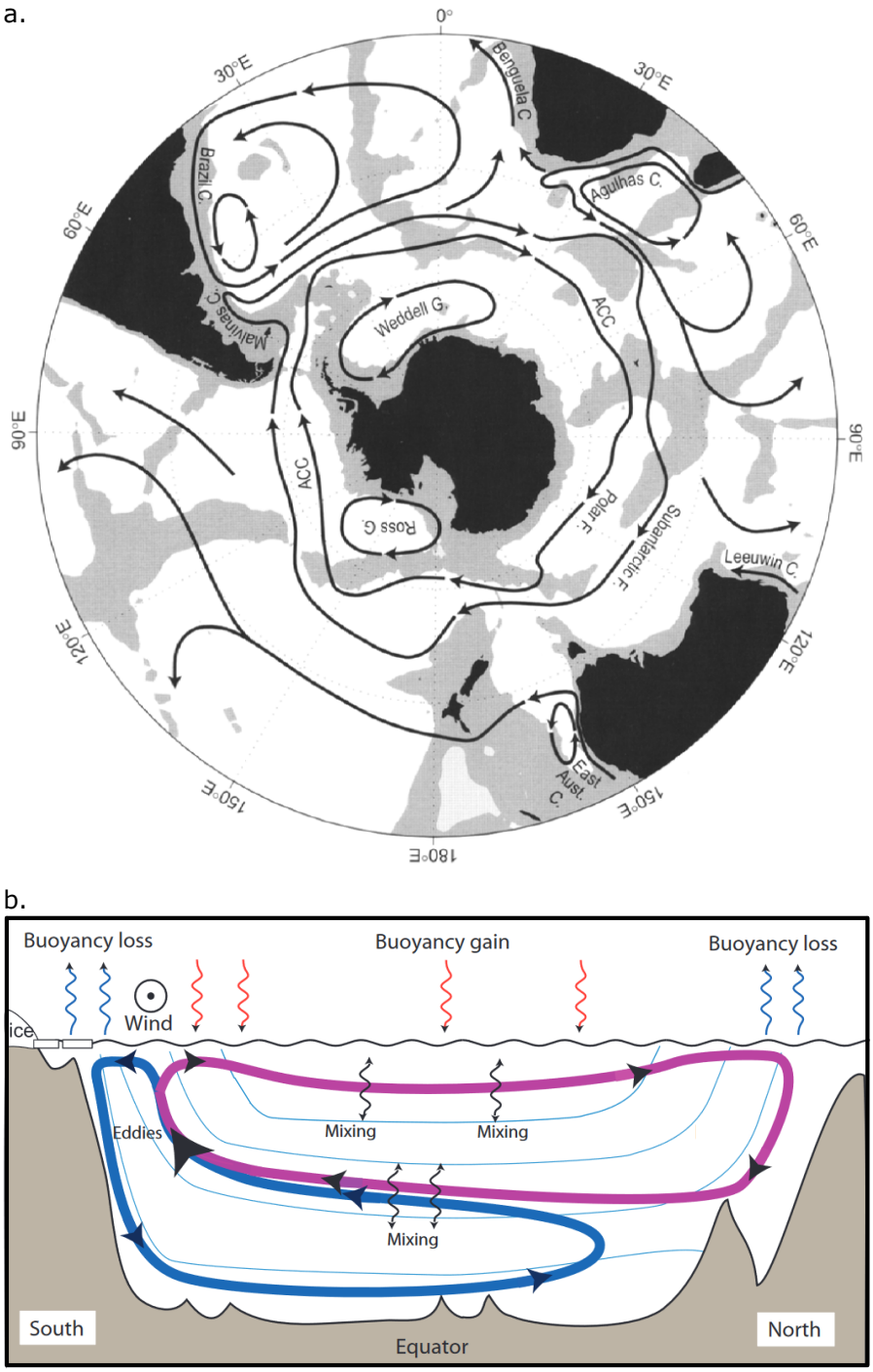

Figure 1.1: (a) A schematic map of the major depth-integrated currents south of 20°S from Rintoul et al. (2001). The two fronts of the ACC are shown, the Subantarctic Front and the Polar Front. Other abbreviations used are F for front, C for current, and G for gyre. (b) A two-dimensional sketch of the MOC from Vallis (2017) which is most representative of Atlantic longitudes. Labelled are the main processes that drive the overturning - winds, diapycnal mixing, baroclinic eddies, and surface buoyancy fluxes. The blue lines represent isopycnals.

The Southern Ocean is a central component of the global ocean's meridional overturning circulation (MOC). The MOC arises from surface water sinking mostly at polar latitudes and upwelling elsewhere. Figure 1.1b illustrates a two-dimensional textbook description of the MOC (Vallis, 2017) which is most representative of Atlantic longitudes. Water on the Antarctic margins experiences buoyancy loss and sinks in the lower cell of the MOC where the densest water masses are found. Surface water also experiences buoyancy loss in the Arctic and sinks as part of an upper overturning cell.

Significant amounts of upwelling for both the upper and lower cell takes place in the open Southern Ocean (Gebbie and Huybers, 2010) as a result of buoyancy forcing, eddy processes, diapycnal mixing, and wind stresses (Abernathey et al., 2011; Garabato et al., 2007; Speer et al., 2000; Zika et al., 2009). As illustrated in Figure 1.1b, the upwelling tilts the isopycnals which enables a strong zonal jet via thermal wind balance. This jet is the Antarctic Circumpolar Current (ACC) and is the strongest current in the global ocean (shown in Figure 1.1a). The tilted isopycnals also fuel baroclinic instabilities which flatten the density surfaces and influence the ACC transport. Eddy activity can also induce an eddy overturning which opposes the time-averaged upwelling in the centre of the ACC (Abernathey and Ferreira, 2015; Danabasoglu et al., 1994; Johnson and Bryden, 1989).

The ventilation of the abyssal ocean is dependent on complex formation process on the Antarctic shelf and gravity-driven outflows (Nicholls et al., 2009). Consequently, accurately representing water masses such as Antarctic Bottom Water (AABW) is difficult in ocean simulations (Heuzé et al., 2013). An important dynamic feature of the Antarctic shelf is the Antarctic Slope Front (ASF). The ASF is a sharp gradient in temperature and/or salinity that surrounds the Antarctic margins. Associated with the ASF is the Antarctic Slope Current (ASC), a coherent current that is largely controlled by the strength of westward winds. Thompson et al. (2018) define three regional classifications for the Antarctic shelf in an extensive review of the ASC. Here, we consider these classes to identify the relevant water masses, flows, and physical processes of the Antarctic shelf.

The three classes proposed by Thompson et al. (2018) are the following: fresh shelf, dense shelf, and warm shelf. The locations and properties of the classes are shown in Figure 1.2. In the fresh shelf regime (Figure 1.2b), strong easterly winds cause onshore Ekman transport and the ASC is particularly intense. Consequently, a sharp density front forms that separates cold and fresh shelf water from warm and salty Circumpolar Deep Water (CDW). Cross-shelf exchange can only occur via diapycnal mixing which modifies the water mass properties. On a dense shelf (Figure 1.2c), the extreme buoyancy forcing from coastal polynyas forms dense shelf water which flows across the shelf break. The isopycnals adopt a characteristic 'V-shape' (e.g. Gill and Niller, 1973; Thompson and Heywood, 2008) which allows a larger range of densities to access the shelf. On a warm shelf, the density front and ASC is weak and the shelf is flooded with warm CDW. When considering the warm shelf, it is important to note that the ASC is not a circumpolar feature. In some areas, the ASC can be weakened or reversed by its proximity to the ACC, weaker wind patterns (e.g. Turner et al., 2013), limited buoyancy forcing, and distance from the subpolar gyres.

Sandwiched between the upwelling in the ACC and the downwelling on the Antarctic shelf are the two subpolar gyres of the Southern Ocean. The Weddell Gyre and the Ross Gyre (shown in Figure 1.1a) are coherent circulations that mediate the transport of water between the Antarctic shelf and the ACC. This zonally asymmetric process is overlooked in two-dimensional models of the MOC but plays an important role in the regional uptake of carbon (MacGilchrist et al., 2019) and the ventilation of the abyssal ocean (van Sebille et al., 2018). CDW traverses the Weddell Gyre at intermediate depths, so the upper layers of CDW are progressively cooled and freshened via vertical diffusion and mixing (Martinson, 1990; Reeve et al., 2019; Wilson et al., 2019). This ventilation process effectively insulates the Antarctic margins from the warm currents of the ACC. However, the Weddell Gyre also acts as a large standing eddy that enhances the volume exchange between the Antarctic shelf and circumpolar water (Klatt et al., 2005; Reeve et al., 2019; Schröder and Fahrbach, 1999). The combined effect of these

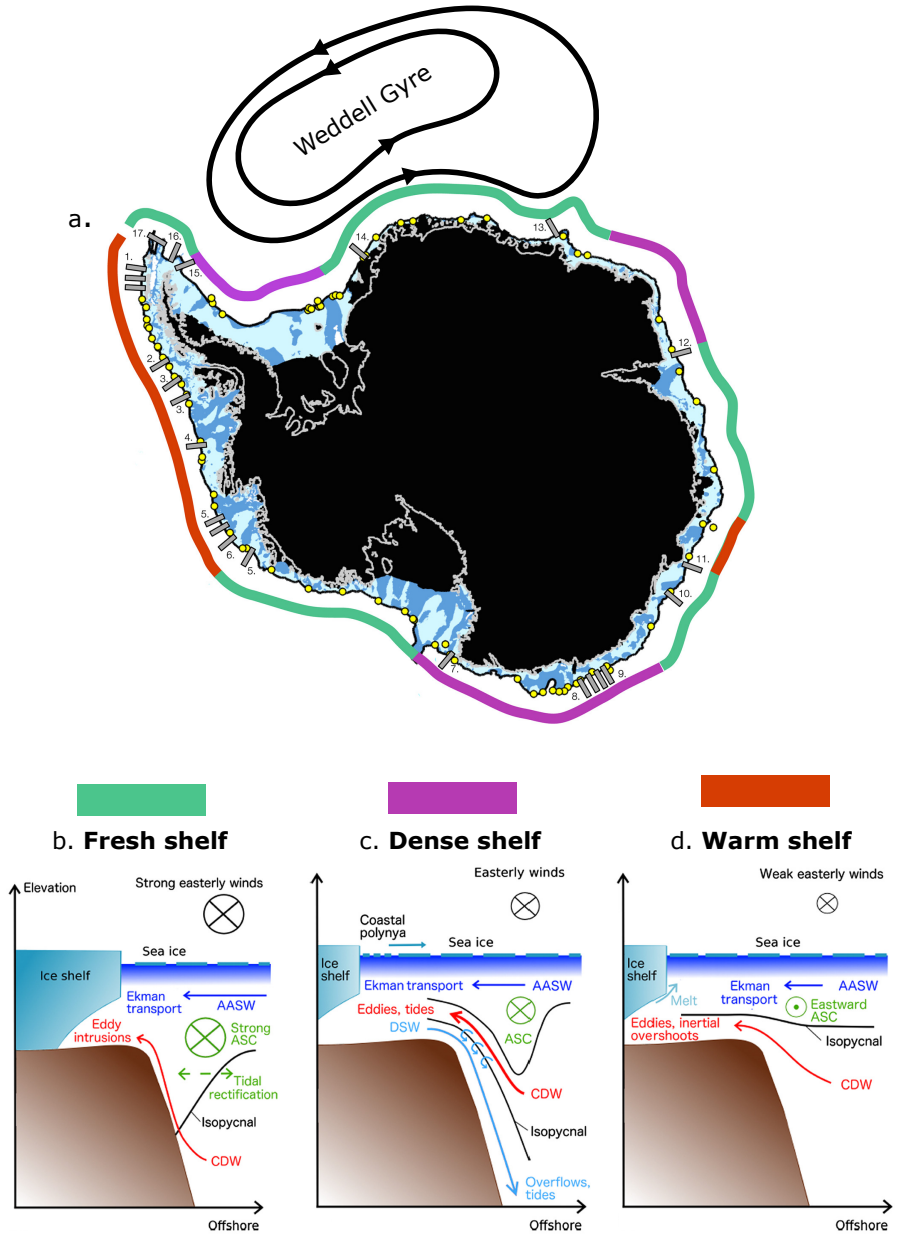

Figure 1.2: Figure from Thompson et al. (2018) illustrating the three classes of shelf surrounding Antarctica. (a) Shows the spatial distribution of the three classes. The black contour is the shelf break, represented by the 1000 m isobath. The blue shading indicates the bathymetry of the continental shelf. Light blue indicates a depth less than 500 m and dark blue indicates a depth greater than 500 m. The yellow circles show the position of historical hydrographic measurements (detailed in Thompson et al. (2018)). The gray bars indicate the positions of recent hydrographic sections used in determining the shelf classifications in Thompson et al. (2018). Key water masses, flows, and physical processes for (b) fresh, (c) dense, and (d) warm shelves.

two opposing processes is poorly understood and it is unclear if the subpolar gyres are a bridge or barrier to the poleward flow of CDW.

While the global relevance of the southern subpolar gyres is now appreciated, their dynamics and role in the wider Southern Ocean remains understudied, certainly compared to the northern subpolar gyres (e.g. Desbruyères et al., 2019; Lohmann et al., 2009; MacGilchrist et al., 2020; Petit et al., 2020; Sun et al., 2021; Tooth et al., 2023; Zhang, 2008). In this thesis, we work to restore hemispheric balance by taking a deep dive into the dynamics of the Weddell Gyre and its role in Southern Ocean ventilation.

1.2 The Weddell Gyre

The Weddell Gyre is the largest subpolar gyre in the southern hemisphere and spans an area of approximately six million square kilometers in the Atlantic sector of the Southern Ocean. The gyre is exposed to extreme buoyancy forcing, steered by sharp topographic features at the sea floor, and lies south of the ACC. Consequently, the Weddell Gyre is both an important limb of the global climate system and a unique case study in geophysical fluid dynamics.

The buoyancy forcing in this region is intense. Atmospheric temperatures are low and sea ice formation is extensive. Sea ice insulates the ocean from the cold atmosphere above but offshore winds can sustain coastal polynyas which enable buoyancy forcing via brine rejection (Abernathey et al., 2016; Haid and Timmermann, 2013). Some of the densest water masses are formed in the Weddell Sea. Of particular interest is the production and export of AABW, which contributes to the southern closure of the global overturning circulation when exported northwards (Lumpkin and Speer, 2007; Marshall and Speer, 2012; Sloyan and Rintoul, 2001; Talley et al., 2003). Recent evidence suggests that the variability of dense slope water export is closely tied to the wind-driven acceleration of the Weddell Gyre's western boundary current (Meijers et al., 2016). The Weddell Gyre strength therefore has the potential to influence global overturning by modifying the ocean's density budget.

There is some debate about exactly how much AABW is produced and exported by the Weddell Gyre. Orsi et al. (1999) and Orsi et al. (2002) suggest 60-70% of all AABW originates from the gyre while Jullion et al. (2014) argues that such high estimates are overstated as up to 30% of the AABW exported by the gyre originated from the Southern Ocean Indian sector. A more complete review of the debate can be found in Vernet et al. (2019).

The surrounding coastline and local topographic features shape the Weddell Gyre. The southern limb of the gyre follows the border of the Antarctic mainland and is steered north by the Antarctic Peninsula. In contrast, the eastern boundary of the Weddell Gyre is a dynamic feature and it is uncertain whether any topographic feature constrains it. Estimates of the eastern boundary location range from 30°E (Deacon, 1979) to as far as 70°E. Within this longitudinal range there is an abundance of eddies that allow exchange between the gyre and the ACC (Park et al., 2001; Ryan et al., 2016; Schröder and Fahrbach, 1999).

Warm and salty CDW from the ACC is an essential component of the Weddell Gyre's density budget. There are two known routes for CDW to enter the gyre. Firstly, there is a direct eddy-driven route across the gyre's eastern boundary (Jullion et al., 2014; Leach et al., 2011; Ryan et al., 2016; Schröder and Fahrbach, 1999). The second route emerges from the ASC (Thompson et al., 2018), which brings CDW from the far east to the gyre (Cisewski et al., 2011) in addition to imported AABW (Jullion et al., 2014; Naveira Garabato et al., 2014).

Two zonally elongated ridges act as partial barriers between the ACC and Weddell Gyre: the South Scotia Ridge in the west and the North Weddell Ridge in the east (Vernet et al., 2019). These ridge systems are typically within 1500 to 2000 m of the sea surface and play a major role in setting the stratification of the entire region (Orsi et al., 1993; Wilson et al., 2022). The South Scotia Ridge contains a series of narrow gaps. These gaps (the Orkney Passage in particular) are the main pathway for bottom water export from the Weddell Gyre (Franco et al., 2007; Jullion et al., 2014; Naveira Garabato et al., 2002).

Often the Weddell Gyre and the neighbouring Ross Gyre are considered to be separate circulations. However, it has been proposed that there is a 'supergyre' south of the ACC rather than two separated subpolar gyres (Sonnewald et al., 2023). The supergyre can also been simulated in specific CMIP5 and CMIP6 models (Wang, 2013).

1.3 Observational challenges

The strength and properties of the Weddell Gyre remain poorly constrained by observations as the circulation lies in such a remote and inaccessible location. In winter, it is a challenging environment for research vessels and the extensive sea ice reduces the information available to satellites.

Measurements of the Weddell Gyre transport are limited and vary widely. Gordon et al. (1981) use wind stress data and apply Sverdrup balance to estimate the Weddell Gyre transport as 75 Sv (1 Sv = 10^6 m^3s^{-1}) while questioning the validity of Sverdrup dynamics. Moorings and ship data provide lower estimates of the transport, for example, 20-56 Sv from Fahrbach et al. (1991) and 30 Sv from Yaremchuk et al. (1998). In Reeve et al. (2019), the Weddell Gyre transport is estimated to be 32 $\pm$ 5 Sv using Argo data (Argo, 2020). While recent Argo data has significantly increased the number of available observations, coverage is still fairly limited within the Weddell Gyre. Argo floats have collected approximately 28,000 hydrographic profiles (south of 60°S) over a time period of 14 years with no measurements taken at pressures grater than 2000 dbar. Reeve et al. (2019) use the thermal wind relation to estimate the geostrophic velocity in the upper 2000 dbar of the Weddell Gyre, extrapolate over depth to estimate the full volume transport, and use ship-based observations to estimate the extrapolation error.

For most of the global ocean, satellite radar altimeter measurements have provided regular estimates of the sea surface height and surface geostrophic currents (Cazenave et al., 2014). Winter sea ice cover in the Southern Ocean severely limits this coverage but retrievals from openings in the ice can be combined with open ocean measurements to measure the Weddell Gyre year-round. This method was

originally deployed in the Arctic (Armitage et al., 2016; Giles et al., 2012) but has now been extended to the Southern Ocean (Armitage et al., 2018). The data from Armitage et al. (2018) suggest that the month-to-month variability of the Weddell Gyre transport is largely influenced by the local wind stress curl. The annual average of the gyre transport is found to be sensitive to the Southern Annular Mode (SAM), a leading mode of atmospheric variability in the Southern Ocean. Positive phases of the SAM involve a contraction and strengthening of the westerly winds in the Southern Ocean and intensify the northern limb of the Weddell Gyre (Armitage et al., 2018). Long term changes in the SAM might have an opposite effect on the southern limb of the gyre as the ASC is weakened by positive SAM values.

1.4 Modelling challenges

Climate models disagree on the strength and shape of the Weddell Gyre and the limited winter-time observations make it difficult to assess model accuracy in this region. Wang (2013) studies fourteen CMIP5 simulations with horizontal grid spacings of 1° or larger and finds that the time-averaged Weddell Gyre transport ranges from 10 to 80 Sv. When considering coupled climate models, this variability could originate from many sources including: the atmospheric model, the representation of sea ice, the numerics of the ocean model, and the boundary conditions used. This variability is troubling as Meijers et al. (2016) suggest that variability in the export of dense Weddell Sea slope water is closely tied to wind-driven acceleration of the Weddell Gyre's western boundary current. Inconsistent Weddell Gyre circulations between climate models may lead to inconsistent descriptions of the global overturning circulation and consequently inconsistent global heat, carbon, and freshwater budgets.

Long time integrations of numerical ocean models under different climate forcing scenarios are prohibitively expensive to run at mesoscale eddy-resolving resolutions, but high resolution simulations are becoming increasingly affordable. Hewitt et al. (2020) comment that the average horizontal resolution of the ocean has increased with each iteration of CMIP and this corresponds to an approximate doubling of

horizontal resolution every ten years (Fox-Kemper, 2018). The majority of centres participating in CMIP6 parameterize the effect of unresolved eddies, but there are now several 'eddy-permitting' models. These models at least partially resolve the mesoscale eddies (Hewitt et al., 2020), taking into account the small Rossby deformation radius at these high latitudes (Hallberg, 2013).

When studying the role of mesoscale eddies in the Weddell Gyre, a hierarchy of models with different resolutions can be a powerful tool. Neme et al. (2021) study the Weddell Gyre in a hierachy of ocean-ice models, ACCESS-OM2 (Kiss et al., 2020), and find that the time-averaged gyre transport increases from 34 to 41 Sv when the horizontal grid spacing is reduced from 1° to 0.1°. Similarly, the seasonal range of the gyre transport increases from 9 to 15 Sv. In Neme et al. (2021), 35-45% of the gyre strength variability originates from the seasonal cycle, consisting of winter intensification and summer weakening. The interannual variability of the gyre transport is also significant and becomes even more pronounced at higher resolutions.

In the Met Office's global ocean simulations the Weddell Gyre is extremely sensitive to the horizontal resolution. This is true for both forced ocean models and simulations that are coupled to atmospheric models. Figure 1.3 shows the time-averaged depth-integrated stream function of the subpolar gyres in an eddy-parameterized (1°), eddy-permitting (1/4°), and eddy-rich (1/12°) ocean simulation which are all coupled to the same atmospheric model. These three stream functions are calculated from the final 10 years of the ML, MM, and MH spinup simulations described in Roberts et al. (2019). The simulations are designed to be as consistent with each other as possible and form a hierarchy of model resolutions. The exact parameters used in these simulations are given in Table 2 of Roberts et al. (2019) and more general details can be found in Storkey et al. (2018). Immediately, one can see that the Weddell Gyre is particularly strong and extensive in the eddy-permitting simulation and weakest in the eddy-parameterized case. All three simulations in Figure 1.3 use NEMO (Madec et al., 2019), an ocean model that is used in a wide range of climate projections for CMIP5 and CMIP6 (phase 6 of the Coupled Model Intercomparison Project). This behaviour is explored in

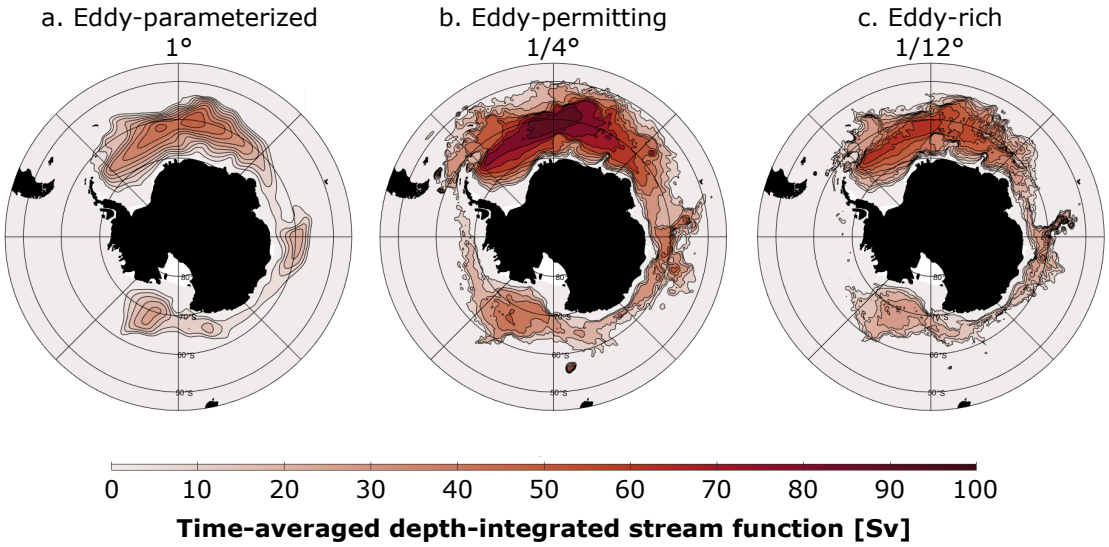

Figure 1.3: Figure by David Storkey (Met Office). The time-averaged depth-integrated stream function of the subpolar gyres in an (a) eddy-parameterized, (b) eddy-permitting, and (c) eddy-rich forced global ocean model. The horizontal resolutions are 1°, 1/4°, and 1/12° respectively.

Chapter 2, where we study the gyre's sensitivity to mesoscale eddies and horizontal resolution using an idealized model built with NEMO.

Finally, the discretization of numerical models should always be considered. How variables are distributed and calculated on a model grid determine what conservation laws are respected by the simulation and the nature of the forcing applied. For example, Hecht (2010) found that severe amounts of spurious cooling can occur when a dispersive advection scheme is used with the Gent and McWilliams (1990) eddy parameterization. In another example, Adcroft and Marshall (1998) found that the orientation of a model grid relative to coastlines can generate spurious form stresses. This effect can also influence the domain-wide vorticity budget (Dupont et al., 2003) and mitigation strategies are discussed in Nasser et al. (2023). In Chapter 3, we discover a limitation to vorticity budgets for gyres on the C-grid (Mesinger and Arakawa, 1976).

1.5 Aims of the thesis

This thesis aims to address three distinct but related questions about the Weddell Gyre.

- How do mesoscale eddies and the dynamics of the ACC influence the Weddell Gyre?
- What are the important forces acting on the Weddell Gyre?
- What are the large scale spatial and temporal patterns of ventilation in the Southern Ocean and how is the Weddell Gyre involved?

We tackle each of these question in Chapters 2, 3, and 4 respectively and summarize our findings in Chapter 5.

1.6 Thesis structure

Throughout this thesis we will explore the dynamics of the Weddell Gyre and its influence on Southern Ocean ventilation. In Chapter 2, we use an idealized model of the Weddell Gyre to investigate the gyre's sensitivity to mesoscale eddies and the ACC strength. In this experiment, we find that the Weddell Gyre is extremely sensitive to horizontal resolution and is particularly strong at eddy-permitting resolutions. The eddy-permitting simulations exhibit the largest horizontal density gradients which induce a significant thermal wind transport for the gyre and fuel mesoscale eddy activity which intensifies the circulation at the sea floor via non-linear dynamics.

Vorticity diagnostics are a powerful tool for understanding how simulated forces generate local rotation in models. In Chapter 3, we take a deep dive into the vorticity budget of a realistic simulated Weddell Gyre and a commonly used double gyre experiment. In doing so, we identify a large spurious force which emerges from the C-grid discretization. In the case of the Weddell Gyre, this spurious term dominates the vorticity budget and is similar in magnitude to the wind stress. This is an alarming result which questions the validity of vorticity budget methods in C-grid models. For the benefit of the ocean modelling community, we explore the origins of the spurious force and discuss potential methods of mitigation.

In Chapter 4, we take a step back from the fine details of model numerics and the mesoscale to study the ventilation of the Southern Ocean. We conduct an extensive

backwards-in-time trajectory experiment to identify spatial and temporal patterns of ventilation. Temporally, we find that almost all ventilation occurs between August and November in the Southern Ocean. Spatially, we identify a circumpolar pattern of ventilation alongside various hotspots of ventilation in the open Southern Ocean. A fraction of shelf-based ventilation is local to known dense water formation sites but the remaining ventilation is distributed more evenly across East Antarctica. In contrast, practically zero ventilation occurs within the subpolar gyres. In our experiment, we find that the western boundary currents of the subpolar gyres are important export pathways for shelf-ventilated water. We also find that volumes within the streamlines of the Weddell Gyre ventilate remotely on the Antarctic shelf and at a site of deep convection in the ACC.

In Chapter 5, we make some concluding remarks and summarize the main findings of the thesis. Appendix A adds to the detail of Chapter 3, including a derivation of the vorticity equation and additional details on the discretization.

2

The Sensitivity of an Idealized Weddell Gyre to Horizontal Resolution

Contents

In this chapter, we use an idealized model of the Weddell Gyre to explore the gyre's sensitivity to mesoscale eddies. The idealized model includes an ACC, so this chapter is also an opportunity to study how the Weddell Gyre and the ACC are coupled. The content of this chapter is based on a published paper in the *Journal of Geophysical Research - Oceans* (Styles et al., 2023d). I took the lead for this project by designing and developing the idealized model, conducting

the experiments, and writing the paper.

2.1 Introduction

As discussed in Chapter 1, the Weddell Gyre is an important component of the global overturning circulation. In light of recent evidence that the export of Weddell Sea slope water is closely tied to the acceleration of the gyre's boundary current (Meijers et al., 2016), it is imperative to accurately describe the Weddell Gyre in climate projections. Unfortunately, observational estimates of the Weddell Gyre strength vary widely (see Section 1.3) and estimates of the gyre strength in climate models are similarly varied (see Section 1.4). The majority of climate models in CMIP5 and CMIP6 parameterize the effect of eddies; however, eddy-permitting models are becoming increasingly affordable to run for climate projections (see Section 1.4). This prompts the question, would the inclusion of explicit eddies improve the agreement between climate simulations of the Weddell Gyre?

To assess how mesoscale eddies influence the Weddell Gyre transport in the real ocean, we need more observational constraints. To accurately estimate the gyre transport, the number of ARGO floats in this region would need to be increased by an order of magnitude (Reeve et al., 2019). Measuring the eddy activity of the Weddell Gyre could also be achieved using ARGO floats, but is an even greater challenge as mesoscale eddies would need to be sampled across the eastern limb of the gyre. This is an area larger and more observationally-hostile than other eddy hotspots such as the Gulf Stream. With present observational data sets it seems impossible to connect the Weddell Gyre strength to the mesoscale eddy activity.

There are not enough eddy-permitting climate simulations in CMIP6 to accurately assess how explicit eddies influence the Weddell Gyre in climate projections. When studying the role of mesoscale eddies in the Weddell Gyre, a hierarchy of models with different resolutions can be a powerful tool. In Adcroft et al. (2019), the results of a 0.5° and a 0.25° ocean-ice model (GFDL OM4.0) are compared. These two models only differ in resolution and physical parameterization and produce similar density structures in the Weddell Sea at 42°W. Neme et al. (2021) study

the Weddell Gyre more directly in another hierarchy of ocean-ice models, ACCESS-OM2 (Kiss et al., 2020), and find that the time-averaged Weddell Gyre transport increases from 34 to 41 Sv when the horizontal grid spacing is reduced from 1° to 0.1°. Models such as those studied by Adcroft et al. (2019) and Neme et al. (2021) offer realism but are less configurable and more computationally expensive than idealized models that might demonstrate similar behaviour.

In the idealized and eddy-permitting simulations by Wilson et al. (2022), the introduction of a zonal submarine ridge intensifies the Weddell Gyre. Wilson et al. (2022) also comment that the ACC and Weddell Gyre primarily interact through transient eddies on the eastern boundary of the zonal ridge. As discussed in Chapter 1, zonally-elongated ridges play a major role in setting the stratification of the gyre and ACC in the real ocean (Orsi et al., 1993). Figure 2.1b illustrates the potential density based on hydrographic sections of the Weddell Gyre and ACC. The contours of potential density in the Weddell Gyre are domed and there is a steep meridional density gradient above the submarine ridge (approx. 54°S in Figure 2.1b). As seen in Figure 2.1b, this is true if a reference pressure of 0 (σ_0), 1000 (σ_1), or 2000 (σ_2) dbar is used when calculating the potential density. As a result, only the densest isopycnals in the ACC outcrop in the Weddell Gyre and are exposed to the intense buoyancy forcing found near the sea surface of the Weddell basin and on the continental shelf (Naveira Garabato et al., 2016).

In this chapter, we aim to investigate how mesoscale eddies can influence the Weddell Gyre and its interaction with the ACC. We do this by varying the horizontal resolution of an idealized model over a wide range of horizontal grid spacings including: eddy-parameterized scales (80 and 40 km), eddy-permitting scales (10 and 20 km), and eddy-rich scales (3 km). The Weddell Gyre is found to be extremely sensitive to horizontal resolution and is strongest at eddy-permitting resolutions.

The chapter is structured as follows. In Section 2.2 we describe the idealized model used in this study and in Section 2.3 we describe the three experiments that are carried out. In Section 2.4 we present our results including a thermal wind decomposition of the Weddell Gyre and ACC transport. In Section 2.5, we discuss

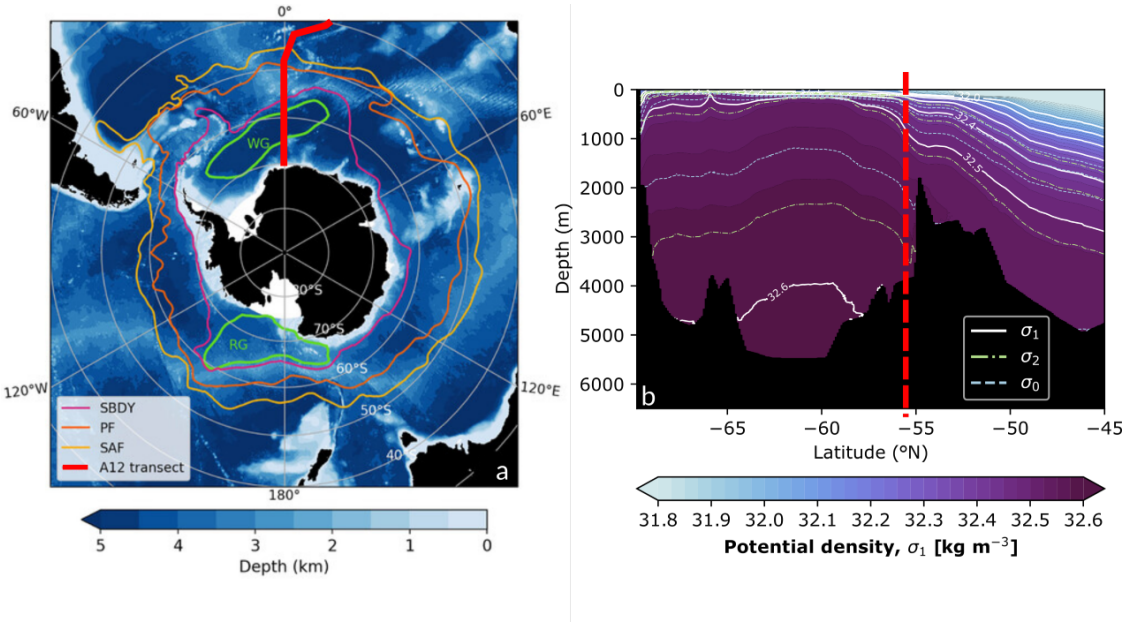

Figure 2.1: Bathymetric and hydrographic features of the Southern Ocean. (a) From Wilson et al. (2022), the bathymetry of the Southern Ocean. The contours mark three fronts of the ACC (Orsi et al., 1995): Southern Boundary (SBDY), Polar Front (PF), and Subantarctic Front (SAF). Outlines of the Weddell Gyre (WG) and and Ross Gyre (RG) are also shown, using contours of satellite-based dynamic ocean topography (Armitage et al., 2018). (b) Potential density along the A12 transect [red line in (a)] calculated using conservative temperature and absolute salinity measurements from 10 hydrographic sections. The gridded hydrographic data originates from the GO-SHIP Easy Ocean product (Katsumata et al., 2022). White contours show potential density surfaces that are calculated with a reference pressure of 1000 dbar (σ_1). Green and blue contours show similar potential density surfaces that are calculated with a reference pressure of 2000 (σ_2) and 0 (σ_0) dbar respectively.

how mesoscale eddies can strengthen the flow at the sea floor and the missing physics in our model design. Closing remarks are made in Section 2.6.

2.2 Model design

The experiments presented in this chapter are performed in the NEMO Community Ocean model (Madec et al., 2019). NEMO has been used for several idealized gyre studies (Lévy et al., 2010; Lévy et al., 2015; Perezhogin, 2019; Ruggiero et al., 2015; Styles et al., 2022) and the presented configuration is similar to the model used by Wilson et al. (2022). The configuration features a zonally periodic channel and a southern continental shelf which resembles the neighbouring coastline for the Weddell

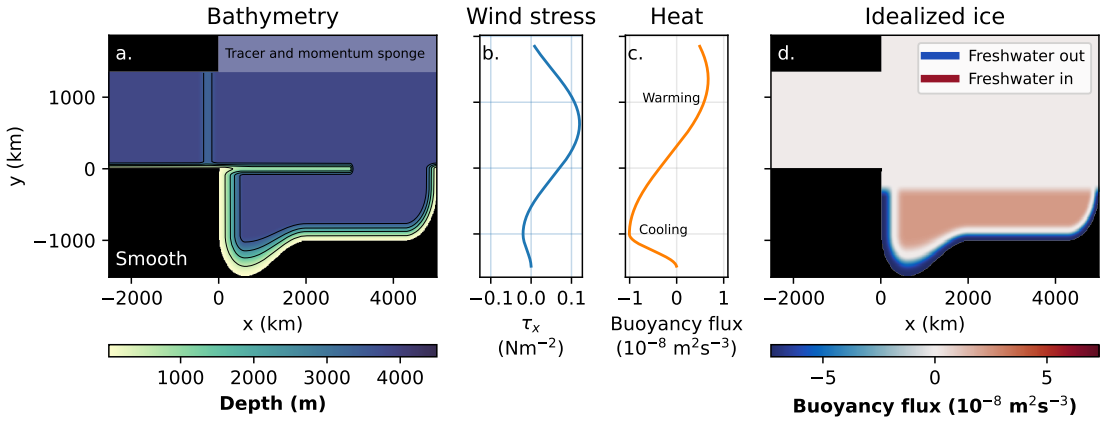

Figure 2.2: Summary of the model configuration. (a) Bathymetry of the model (without topographic noise) with contours at 1000 m intervals. (b) The zonal wind stress profile for the configuration. (c) The zonal heat flux profile for the configuration in units of buoyancy flux. (d) The freshwater fluxes used to represent sea ice for the configuration in units of buoyancy flux. In this model, a buoyancy flux of 10^{-8} m^{2}s^{-3} corresponds to 14.9 Wm^{-2} of surface heating or approximately 4×10^{-5} kg m^{-2}s^{-1} of freshwater input (assuming a surface salinity of 35 psu).

Gyre (see Figure 2.2a). Two large landmasses are present on the western margins of the model, with an opening that crudely represents the Drake Passage. Additional topographic features include a submarine ridge which extends eastwards from the idealized Drake Passage and a meridional sill in the Drake Passage that blocks f/H contours and regulates the ACC transport (f is the Coriolis parameter and H is the ocean depth). A necessary consequence of the periodic model design is a well-defined eastern boundary for the gyre. As discussed in the previous chapter (Section 1.2), the eastern boundary of the gyre is dynamic feature and it is uncertain if any topographic feature constrains it. The parameters for these topographic features and all other relevant fixed parameters can be found in Table 2.1. Throughout this chapter, the x coordinate is the zonal displacement from the eastern boundary of the Drake Passage and the y coordinate is the meridional displacement from the southern boundary of the Drake Passage (see axes in Figure 2.2a).

The model has a regular horizontal grid with a horizontal grid spacing between 80 and 3 km, depending on the experiment (see Table 2.2). For context, on an ORCA grid (Madec and Imbard, 1996) at 65°S the horizontal grid spacing is around 50 km in a 1° model, 12 km in a 0.25° model, and 5 km in a 0.1° model. All

Table 2.1: Summary of fixed parameters in the model. Δx is the horizontal grid spacing of the model in meters. (*) The sill height is varied for the ACC sensitivity experiment but is 500 m for all other experiments.

Model parameter	Value
Meridional domain size	3350 km
Zonal domain size	7520 km
Reference Coriolis parameter	-1.3× 10^{-4} s^{-1}
Meridional gradient of Coriolis parameter	9.6× 10^{-12} m^{-1} s^{-1}
Momentum diffusivity (resolution dependent)	(0.05 Δx) m^2 s^{-1}
Tracer diffusivity (resolution dependent)	(0.005 Δx) m^2 s^{-1}
Maximum (smooth) ocean depth	4000 m
Number of model levels	31
Vertical resolution	10 - 315 m
Continental shelf width	300 - 600 km
Drake Passage zonal length	2520 km
Drake Passage meridional width	1350 km
Drake passage sill zonal width	500 km
Drake passage sill maximum height*	500 m
Submarine ridge zonal extent	3000 km
Submarine ridge meridional width	200 km
Submarine ridge maximum height	3000 m
Root mean square of topographic noise	100 m
Topographic noise length scales	240, 120, 60, 30, 9 km
Topographic noise relative amplitudes	8, 4, 2, 1, 0.3

configurations use z-coordinates and have 31 vertical model levels, with vertical spacing that is approximately 10 m near the sea surface, 315 m near the sea floor, and partial cells are used to represent the varying sea floor. By only varying the horizontal resolution, we are only exploring dynamics that do not require higher order vertical modes. The configuration exists on a beta plane where the Coriolis parameter varies linearly with the meridional coordinate, y, around its value at 65°S (y=0 in Figure 2.2). The model uses a free slip condition on lateral boundaries and applies a linear friction to the bottom boundary with a linear friction coefficient of 4×10^{-4} m s^{-1}. A simplified linear equation of state is used, $\rho = \rho_0 (1 - a_0 T + b_0 S)$, with a thermal expansion coefficient of $a_0 = 2.8 \times 10^{-4}$ kg m^{-3} K^{-1}, a haline coefficient of $b_0 = 7.7 \times 10^{-4}$ kg m^{-3} psu^{-1}, and a reference density of $\rho_0 = 1026.0$ kg m^{-3}. When using a linear equation of state, there is no distinction between conservative and potential temperature, nor is there a distinction between absolute

and practical salinity; therefore, in our results we will simply refer to temperature and salinity. The horizontal diffusion of momentum and tracers is implemented with a diffusivity that scales linearly with horizontal grid spacing (see Table 2.1). Subgrid scale vertical mixing of momentum and tracers is represented by the Turbulent Kinetic Energy scheme (Bougeault and Lacarrere, 1989; Gaspar et al., 1990).

The model is forced with a sinusoidal and zonal wind stress which only varies in the meridional direction. The wind stress profile resembles the zonally and annually averaged wind stress across the Southern Ocean (Figure 2.2b), with a maximum westerly wind stress of 0.12 N m^{-2} over the center of the circumpolar channel and a peak easterly wind stress of 0.02 N m^{-2} along the continental shelf. The surface heat flux profile also resembles the zonally and averaged fluxes across the Southern Ocean. Similarly, the surface heat flux is also sinusoidal and zonally uniform with a maximum surface warming of 10 Wm^{-2} at the northern boundary of the Drake Passage and a peak cooling of 15 W m^{-2} on the south continental shelf. The surface heat flux is shown in units of buoyancy flux in Figure 2.2c and is the dominant buoyancy flux north of the submarine ridge.

The effect of sea ice on the salinity budget is simply represented by a surface freshwater flux, as shown in units of buoyancy flux in Figure 2.2d. The freshwater fluxes resemble the annual-average freshwater fluxes due to sea ice in the Southern Ocean, with freshwater entering the ocean in the Weddell basin and leaving the ocean where there is persistent sea ice formation on the southern continental shelf (Pellichero et al., 2018). Freshwater fluxes are the dominant buoyancy flux in the Weddell basin, as argued by Pellichero et al. (2018), and this is represented in the idealized model. The domain area integral of freshwater fluxes is identically zero to conserve the water content of the model. The model was also tested without the idealized sea ice. Removing the idealized sea ice does not change the gyre or ACC's sensitivity to resolution but the isopycnals are less realistic above the continental shelf.

The northern margin of the model ($y > 1350$ km) contains a sponge layer, which parameterizes the effect of the global ocean to the north. The horizontal

flow is relaxed to rest, the salinity is relaxed to 35 psu at all depths, and the temperature is relaxed to the vertical profile,

$$T(z) = T_{\text{top}} exp(z/\delta_z), \tag{2.1}$$

where T is the temperature, z is the vertical coordinate (relative to the mean free surface height), $T_{\text{top}} = 10°\text{C}$ is the prescribed sea surface temperature and $\delta_z = 1500$ m is the decay length scale of the surface temperature. Consequently, the prescribed sea floor temperature is approximately 0°C. The momentum sponge has a maximum relaxation timescale of 1×10^6 seconds (approximately 12 days) and the tracer sponge has a maximum relaxation timescale of approximately 1×10^7 seconds (approximately 120 days). The sponge layer is 500 km wide and the relaxation timescale varies with y sinusoidally, increasing from zero to the maximum value.

The model's initial state features a sinusoidal ACC with a peak zonal velocity of 0.2 m s^{-1} in the channel center and a zero velocity at $y = 0$ km and $y = 1350$ km. The ACC velocity profile decays with depth similarly to the temperature in the northern sponge (Equation 2.1). The initial state of the gyre basin (south of $y = 0$) is at rest. The initial temperature profile is calculated using the thermal wind relation, integrating south from the northern sponge where the temperature profile matches Equation 2.1. Similarly to the sponge layer, the initial salinity is 35 psu everywhere in the domain.

In some experiments (see the next section) topographic noise is introduced to the bathymetry, as shown in Figure 2.3. The addition of weak topographic noise permits topographic interactions everywhere in the domain but only perturbs the larger scale bathymetric features. The analytic noise field is generated using a zonally periodic and continuous noise generation function, $\mathcal{N}(x, y)$, from OpenSimplex (Spencer, 2022). OpenSimplex was selected to generate a noisy bathymetry with no discontinuities and known statistical properties. Noise is added at various length scales as shown below,

$$\lambda(x, y) \propto \sum_{i=1}^{N_L} \mathcal{N}\left(\frac{x}{L_i}, \frac{y}{L_i}\right) L_i, \tag{2.2}$$

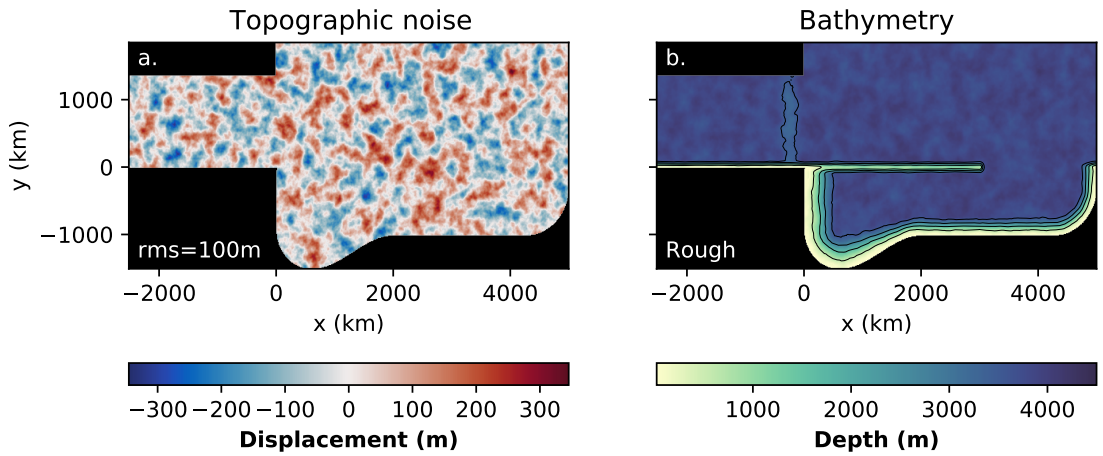

Figure 2.3: (a) Noise profile and (b) bathymetry for the Rough simulation with a horizontal grid spacing of 3 km. All discrete noise fields used in this chapter have a root mean square of 100 m and are based on the same continuous noise function, $\mathcal{N}(x, y)$.

where λ is the final two dimensional noise function, L_i is the i^{th} length scale used (listed in Table 2.1), and N_L is the number of length scales used. The continuous function, $\lambda(x, y)$, is then evaluated on the grid used for each experiment and scaled so that the root mean square (rms) of the discrete noise field is 100 m in all configurations. Each length scale introduces a topographic gradient with a magnitude that is independent of L_i, as demonstrated below,

$$\boldsymbol{\nabla}\lambda(x, y) \propto \sum_{i=1}^{N_L} \boldsymbol{\nabla}\mathcal{N}\left(\frac{x}{L_i}, \frac{y}{L_i}\right). \tag{2.3}$$

As seen in Figure 2.3, the maximum displacement caused by the noise field is approximately 300 m and the structure of the continental shelf and other large topographic features is not lost to the noise. In cases where the added noise would create islands in the domain, the noise is locally reduced to zero so that all topographic features remain submerged.

In Section 2.5, we will discuss the important differences between this idealized configuration and the real ocean and assess how the discrepancies may modify the results presented in this chapter.

2.3 Experimental setup

The model described in the previous section is computationally affordable and a wide parameter space can be explored. In total, 78 simulations were conducted with a minimum run time of 220 years. A summary of the experiments is shown in Table 2.2. There are three sets of experiments: Smooth, Rough, and ACC sensitivity. The Smooth experimental series uses the bathymetry shown in Figure 2.2a and does not feature any topographic noise. The horizontal grid spacing is varied from 80 to 10 km and only the 80 and 40 km simulations include the Gent and McWilliams (1990) eddy parameterization (GM hereafter). The 80 and 40 km simulations use a constant GM diffusivity parameter of 2000 m^2 s^{-1}. The Rough series is exactly the same as the Smooth series but uses topographic noise, as shown in Figure 2.3, and the horizontal grid spacing varies from 80 to 3 km. The 3 km simulation is eddy-rich and computationally expensive so only one eddy-rich time integration could be completed. In Section 2.4.5, we also test various applications of GM on eddy-permitting and eddy-parameterized simulations to see how this affects our main results.

In this model the ACC is driven by wind-stress, surface buoyancy forces, and buoyancy forcing on the northern boundary. The ACC transport is not prescribed, so the ACC strength is free to respond to changes in the horizontal resolution. The ACC sensitivity experiment series is designed to assess how strongly the Weddell Gyre and ACC transports are coupled. Not only is a study of the gyre-ACC coupling scientifically interesting; it is also necessary to assess if the changes in the Weddell Gyre transport with resolution are influenced by changes in the idealized ACC strength. In the ACC sensitivity experiments, the height of the Drake Passage sill is varied from 500 m to 2500 m in intervals of 200 m: this modifies the strength of the simulated ACC in a way that does not modify the immediate conditions for the Weddell Gyre. For example, we cannot modify the wind stress to change the ACC strength as this will alter the wind stress curl above the gyre and change the gyre strength directly. Modifying the wind stress would also be further complicated by eddy saturation effects in simulations with explicit eddies (Marshall et al., 2017).

Table 2.2: Summary of the numerical experiments. Experiments marked with GM use the Gent and McWilliams (1990) eddy parameterization. In total 44 ACC sensitivity experiments were conducted (11 for each horizontal grid spacing between 80 and 10 km).

	Horizontal grid spacing (km)					
Experiment series	80^{GM}	40^{GM}	20	10	3	Topographic noise
Smooth	✓	✓	✓	✓	✗	✗
Rough	✓	✓	✓	✓	✓	✓
ACC sensitivity (11 variations of sill height)	✓	✓	✓	✓	✗	✓

2.4 Results

As seen in Figure 2.4, 200 years is a sufficient spin up time to assume a statistically steady Weddell Gyre and ACC transport. The transports in Figure 2.4 are calculated from annual averages of the depth-integrated stream function. The ACC transport is the zonal average of the stream function along the northern boundary of the domain and the Weddell Gyre transport is the maximum value of the stream function in the gyre basin (south of y=0). Only the gyre transport in the 3 km simulation shows a slight downward trend that does not alter the interpretation of the presented results. We also find that the spatial average of temperature and salinity are also statistically steady. Figure 2.5 shows the evolution of the domain-averaged temperature and salinity for configurations with a rough bathymetry. All configurations have statistically-steady temperature and salinity but the eddy-permitting configurations are on average 0.2-0.4 °C cooler than the eddy-parameterized and eddy-rich simulations.

The residual overturning circulation was calculated using the same method as Wilson et al. (2022), but is challenging to interpret with the present model configuration. In simulations with explicit eddies, the overturning is unrealistically intense near the floor. This is caused by a dense pocket of water which is trapped on the western portion of the Antarctic shelf and is generated by the intense freshwater forcing above it (see Figure 2.2). Consequently, mean isopycnal depth does not always increase with density. In principle, this pocket of dense water could be isolated and removed in the calculation but the residual overturning circulation

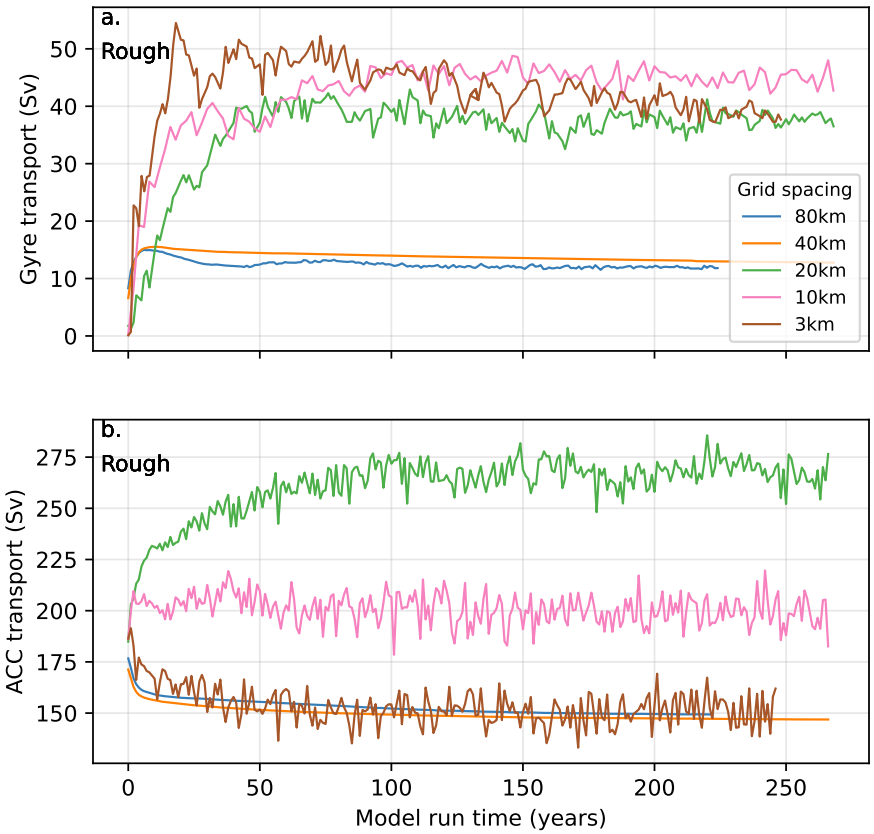

Figure 2.4: Evolution of the (a) Weddell Gyre and (b) ACC transports for configurations with rough bathymetry.

would no longer be complete. For studying the overturning structure of the Weddell Gyre and ACC, we recommend using the model configuration from Wilson et al. (2022), which has simpler geometry and buoyancy forcing.

All results presented in this section are time-averages taken from the final 20 years of each model run. As indicated by Figure 2.6, the 3 km simulation resolves a rich eddy field in the ACC and near the eastern boundary of the zonal ridge. Similar to Wilson et al. (2022), a weaker but qualitatively similar eddy field is partially resolved in 10 and 20 km simulations. The distribution of eddy kinetic energy is discussed further in Section 2.5.1.

2.4.1 Transport sensitivity to resolution

In the Rough and Smooth configurations, the Weddell Gyre and ACC are strongly sensitive to resolution, as shown in Figure 2.7. The transports are calculated from

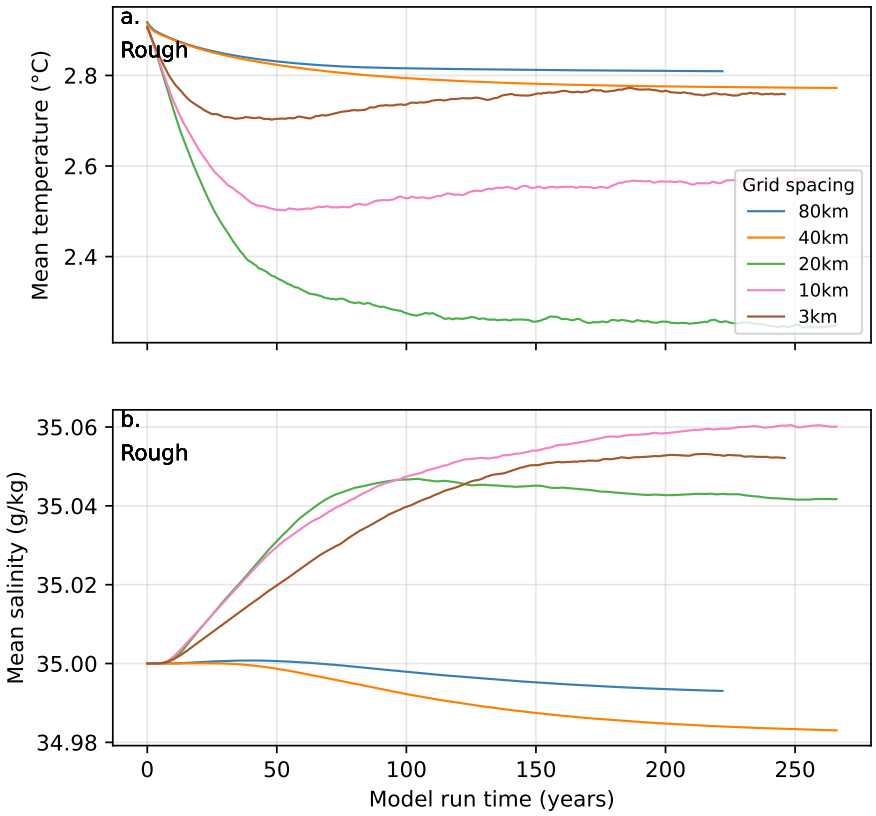

Figure 2.5: Evolution of the domain-averaged (a) temperature and (b) salinity for configurations with rough bathymetry.

the twenty year time-average of the depth-integrated stream function. Figure 2.7a shows how the Weddell Gyre transport increases as the resolution is doubled over smooth bathymetry. The time-averaged Weddell Gyre transport is 28.9 Sv in the 80 km simulation and increases to 54.7 Sv in the 10 km simulation. Introducing a rough bathymetry reduces all gyre transports (17 Sv reduction for the 80 km case, 10 Sv reduction for the 10 km case) but also increases the Weddell Gyre's sensitivity to resolution (Figure 2.7c). With a rough bathymetry, the time-averaged Weddell Gyre transport is 11.9 Sv in the 80 km configuration and then rapdily increases to 44.8 Sv in the 10 km configuration. For the Rough configuration, we have access to an eddy-rich simulation where the Weddell Gyre transport is 38.6 Sv. In this case, the transition from an eddy-permitting to an eddy-rich simulation reduces the Weddell Gyre transport by 6.2 Sv. The red error bars in Figure 2.7a through to 2.7d show the interannual variability of the gyre and ACC transports during

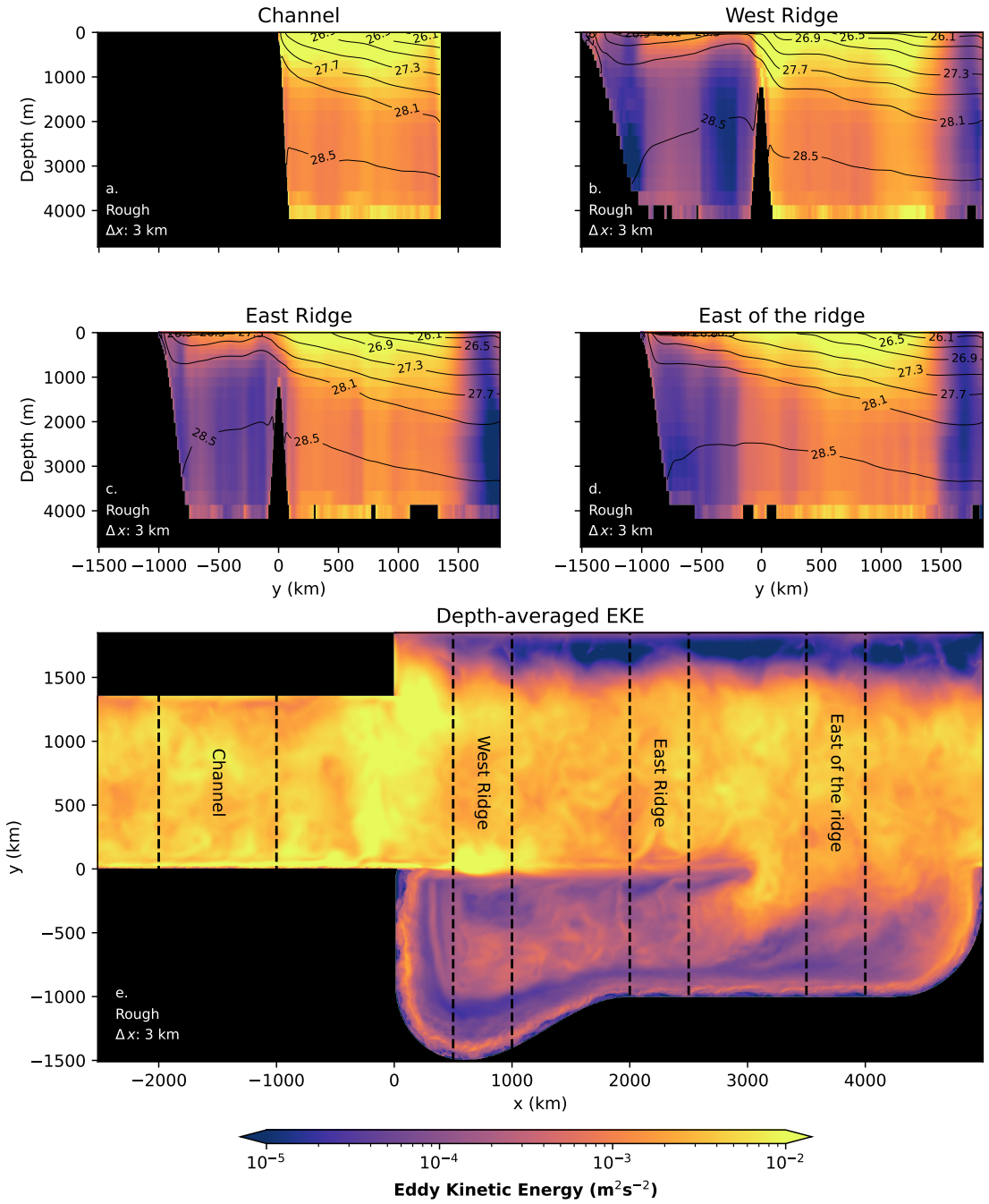

Figure 2.6: (a)-(d) Zonal averages and the (e) depth average of the eddy kinetic energy in a simulation with a 3 km horizontal grid spacing and rough bathymetry. The zonal averages in (a)-(d) are taken over various meridional sections that are shown in (e). The black contours in (a)-(d) show the zonally-averaged density surfaces across the meridional section.

the experimental period (two standard deviations either side of the average). The limited overlap of adjacent error bars suggests that the gyre and ACC transports for almost any year in our experiment are similar to the time-averaged results.

In Figure 2.7, the time-averaged stream function for the gyre shrinks and follows the bathymetry more closely when the resolution increases from eddy-parameterized (80 km) to eddy-permitting (10 km) scales. The boundary current that forms on the submarine ridge becomes particularly narrow and intense. In Section 2.4.3 we use a thermal wind decomposition to relate the transports and stream functions shown in Figure 2.7 to horizontal density gradients and the velocity at the sea floor.

The structure of the ACC is sensitive to the coarseness of the bathymetry. In the Smooth configurations, the ACC is deflected northwards by the ridge in the Drake Passage but quickly returns to a zonal flow which results in large positive and negative meridional velocities in the ACC (Figure 2.7g). In the Rough configurations, the northward deflection of the ACC is similarly severe but the topographic noise appears to dampen the ACC's return to a zonal flow (Figure 2.7h and 2.7i). The ACC's behaviour in the Rough configurations more closely resembles the ACC's abrupt equatorward deflection east of the Drake Passage and the current's more steady poleward trajectory while circumnavigating Antarctica (see Figure 7 of Mazloff et al. (2010)).

The time-averaged ACC transport is also strongly sensitive to resolution in both Smooth and Rough configurations. In particular, the transition from a smooth to rough bathymetry intensifies the ACC transport at eddy-permitting resolutions (increasing from 221.7 to 266.2 Sv at 20 km). With a rough bathymetry, the eddy-parameterized model recreates the ACC transport of the eddy-rich simulation. This suggests that a single GM parameter can recreate the transport of an eddy-rich ACC but not an eddy-rich gyre transport south of it. This could be caused by differences in bathymetry between the two circulations or differences in the Rossby deformation radius. The role of the GM parameterization is discussed further in Section 2.4.5.

In Section 2.4.3, the ACC transport will also be related to horizontal density gradients and the bottom velocity. With a maximum ACC transport of 266.2 Sv

(20 km horizontal grid spacing, rough bathymetry) and a minimum of 147.7 Sv (40 km horizontal grid spacing, rough bathymetry), it is important to assess if such large variations in the ACC transport modify the Weddell Gyre transport directly.

2.4.2 ACC sensitivity results

In the ACC sensitivity experiments, the strength of the ACC is varied by modifying the height of the sill in the idealized Drake Passage. As shown in Table 2.2, these experiments use horizontal grid spacings between 80 and 10 km and all experiments have a rough bathymetry.

The results of the ACC sensitivity experiment are shown in Figure 2.8 where we can immediately see that the gyre transport barely responds ($\sim$ 1 Sv) to large changes in the idealized ACC transport ($\sim$ 100 Sv) at all tested resolutions. The large changes in the Weddell Gyre transport with resolution are controlled by the gyre's direct sensitivity to resolution and not the gyre's sensitivity to the ACC strength.

2.4.3 Thermal wind and bottom flow decomposition

In Section 2.4.1 we observe that the idealized Weddell Gyre and ACC transports are sensitive to horizontal resolution and are particularly strong at eddy-permitting resolutions. In this section, we relate the observed transports to the isopycnal structure of the circulation and the strength of the circulation at the sea floor. The depth-integrated velocity field is separated into depth-dependent and depth-independent components using integration by parts,

$$\mathbf{U} = \int_{-H}^{\eta} \mathbf{u}\, dz = \mathbf{u}_b H + \mathbf{u}_t \eta - \int_{-H}^{\eta} \frac{\partial \mathbf{u}}{\partial z} z\, dz, \tag{2.4}$$

where $\mathbf{U}$ is the depth-integrated velocity field, η is the free surface height, $\mathbf{u}_b$ is the velocity at the sea floor, and $\mathbf{u}_t$ is the velocity at the free surface. We then use the following equation to describe how the the velocity field varies with depth,

$$f \frac{\partial \mathbf{u}}{\partial z} = -\frac{g}{\rho_0} \left(\hat{\mathbf{k}} \times \boldsymbol{\nabla}_h \rho \right) + \boldsymbol{\mathcal{E}}, \tag{2.5}$$

where g is the acceleration due to gravity, ρ_0 is the reference density, $\boldsymbol{\nabla}_h$ is the horizontal gradient operator, ρ is the density, and $\boldsymbol{\mathcal{E}}$ is a residual function. Equation

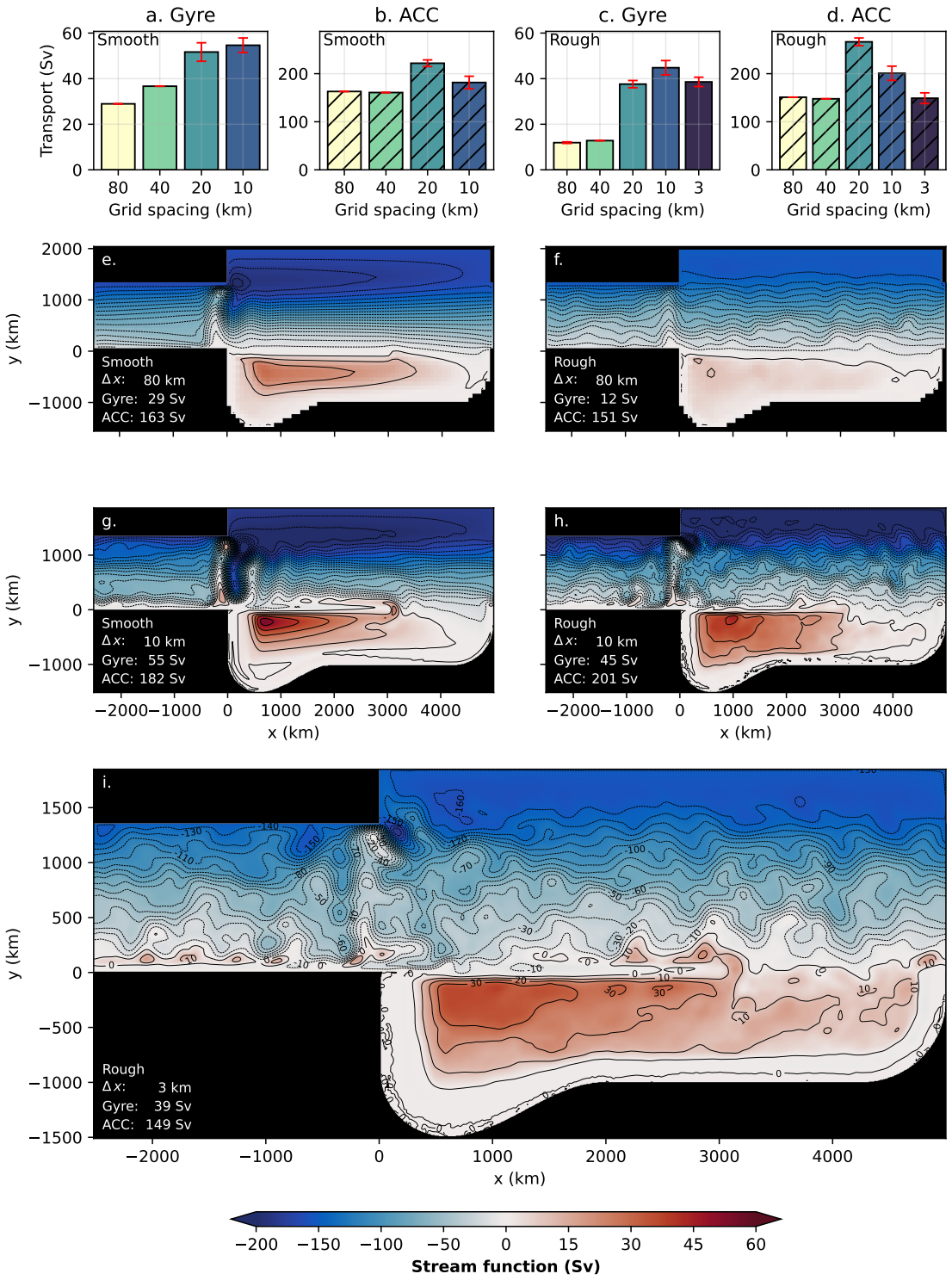

Figure 2.7: Sensitivity of the Weddell Gyre and ACC transport to resolution. (a)-(d) show the time-averaged gyre and ACC transport over smooth and rough bathymetry. Red error bars show the inter-annual variability of the transport (two standard deviations). (e)-(i) are the time-averaged stream functions from configurations at an eddy-parameterized resolution (80 km), an eddy-permitting resolution (10 km), and an eddy-rich resolution (3 km). The black contours have an interval of 10 Sv.

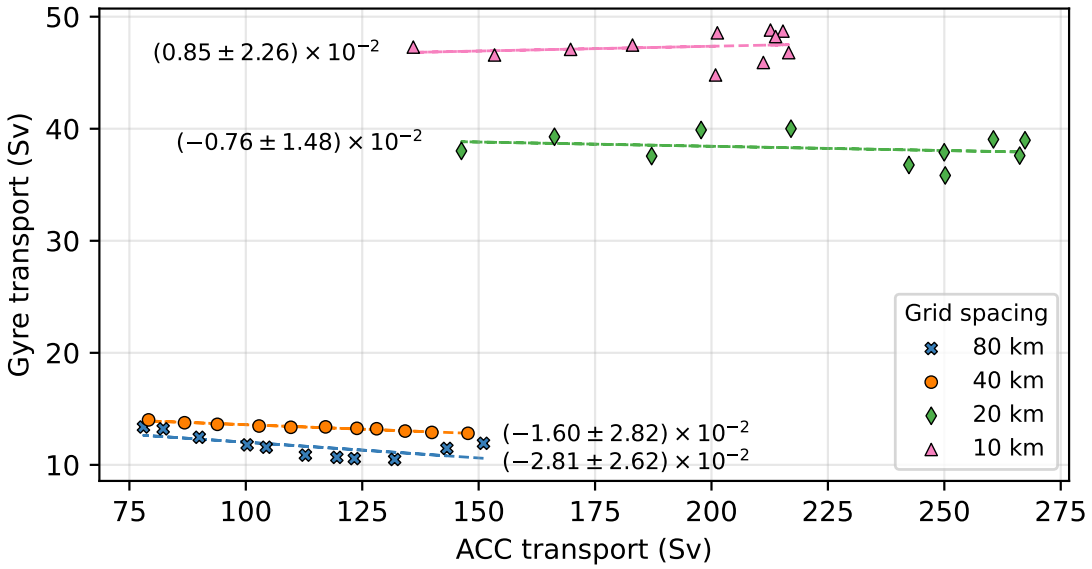

Figure 2.8: How the Weddell Gyre (WG) transport varies with respect to the ACC transport at several resolutions. The dashed line shows the straight line of best fit which is calculated using a least squares method. The value of the slope (dimensionless) and error is provided for each line. The gyre transport is insensitive to large variations in the ACC transport.

2.5 is the thermal wind equation where all non-geostrophic terms, non-hydrostatic terms, and numerical errors are aggregated in $\boldsymbol{\mathcal{E}}$. The model used in this chapter assumes hydrostatic balance so $\boldsymbol{\mathcal{E}}$ is free of non-hydrostatic terms.

By combining Equations 2.4 and 2.5 we can derive a full decomposition of the depth-integrated flow,

$$\mathbf{U} = \underbrace{\mathbf{u}_b H}_{\text{Bottom velocity}} \underbrace{+ \frac{g}{\rho_0 f} \int_{-H}^{\eta} \left(\hat{\mathbf{k}} \times \boldsymbol{\nabla}_h \rho\right) z \, dz}_{\text{Thermal wind}} + \mathbf{u}_t \eta + \boldsymbol{\mathcal{E}}^z, \tag{2.6}$$

where $\boldsymbol{\mathcal{E}}^z$ is the depth-integrated and rescaled residual that still contains non-geostrophic terms and errors from the discretization. The mean free surface height aligns with $z = 0$ (by definition) and therefore the free surface term, $\mathbf{u}_t \eta$, is negligible in all of the presented results.

Using Equation 2.6, we decompose the Weddell Gyre and ACC transport into depth-independent ($\mathbf{u}_b H$) and depth-dependent components (thermal wind and residual). The decomposed transports and the associated stream functions are shown in Figures 2.9 and 2.10 respectively. In order to calculate valid stream

functions, a Helmholtz decomposition of each term in Equation 2.6 is determined using an elliptical solver and the divergent part is removed. The full circulation has a weak divergent component and when this component is removed the largest change in the stream function is 0.03 Sv. The full circulation has a negligible divergence, so only the non-divergent components of the terms in Equation 2.6 influence the full circulation. Each component of the gyre transport shown in Figure 2.9 is equal to the component's stream function evaluated where the maximum streamfunction of the gyre is located (black crosses, Figure 2.10). This definition was chosen as it describes the decomposition of the quantity of interest, the gyre's total transport. As shown in Figure 2.10, the maximum of a specific component's stream function in the gyre basin (blue crosses) does not necessarily align with the gyre centre. The ACC transport components shown are the zonal averages, but zonal variations of the decomposition are small and do not alter our interpretation of the results.

In all cases, the combined transport from the bottom flow and thermal wind component closely describes the total transport of the gyre (black crosses in Figure 2.9). This suggests that the residual terms are minor when considering the gyre and ACC transports. The circulation associated with the residual term, $\boldsymbol{\mathcal{E}}^z$, is weak across most of the horizontal domain meaning that the depth-integrated circulation can be described to leading order using geostrophic assumptions. It is important to note that a small value of $\boldsymbol{\mathcal{E}}^z$ does not guarantee geostrophy at all depths. The residual is largest at lower resolutions, this may be caused by small departures from geostrophy through viscous effects or a larger numerical error that comes with a coarser grid.

Looking at the gyre transports, the relative significance of the bottom velocity and the thermal wind component depends on the coarseness of the bathymetry. In the Smooth configurations, the bottom velocity plays a dominant role in controlling the gyre transport and increases with horizontal resolution. In configurations with a rough bathymetry, the gyre transport from the bottom flow is reduced and comparable to the thermal wind component, but still increases with resolution. When a rough bathymetry is used, the thermal wind component of the gyre is

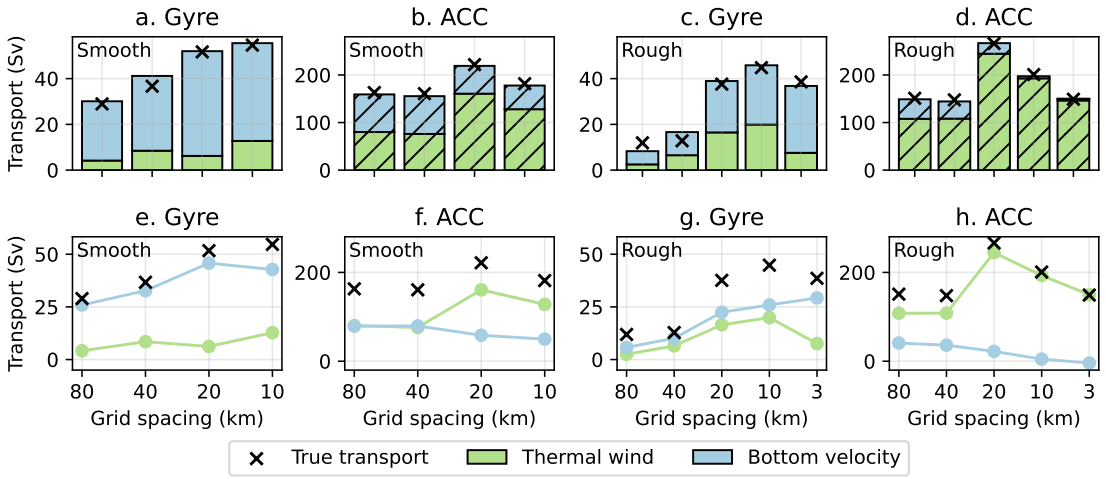

Figure 2.9: A decomposition of the gyre and ACC transports over smooth and rough bathymetries. The thermal wind component describes the geostrophic transport relative to the bottom velocity which emerges from horizontal density gradients. The bottom velocity component describes the depth-independent transport which is determined by the velocity at the sea floor ($u_b H$). The black crosses mark the total gyre and ACC transports shown in Figure 2.7.

particularly strong with a 10 km horizontal grid spacing and consequently the total gyre transport is particularly strong at eddy-permitting resolutions.

The decomposition of the ACC transport is also dependent on the coarseness of the bathymetry. In simulations with a smooth bathymetry, contributions to the ACC transport from the bottom flow and thermal wind components are similar in size (Figure 2.9b). The bottom flow component shrinks with resolution and the thermal wind component is largest at an eddy-permitting resolution (20 km in Figure 2.9b). When a rough bathymetry is used, the ACC transport is almost entirely determined by the thermal wind component, which is even larger at eddy-permitting resolutions (see Figure 2.9d). The decomposition of the ACC with rough bathymetry is more realistic as observations (Chidichimo et al., 2014; Donohue et al., 2016; Koenig et al., 2014) suggest that the ACC transport is largely determined by a thermal wind (or often called 'baroclinic') component.

The shape of the stream function from the bottom flow and the thermal wind components differ. The thermal wind stream function (left column of Figure 2.10) features a gyre that lies over the basin interior and submarine ridge and is not west-intensified. Over the continental shelf there is a density-driven slope current

that reverses direction south of the submarine ridge, which is a consequence of the idealized model design. An accurate slope current may require a wind stress that follows the continental shelf (Thompson et al., 2018). The stream function for the bottom flow transport (right column of Figure 2.10) features a gyre that follows the bathymetry closely and is west-intensified. The submarine ridge blocks the deep current but the bottom flow is free to extend northwards into the ACC channel once it is far enough east.

Over the submarine ridge the thermal wind and bottom velocity stream functions reinforce each other, resulting in a particularly strong western and northern boundary current. In contrast, the thermal wind and bottom velocity stream function are opposite-signed on the continental shelf, which limits the gyre's presence over the continental shelf in all simulations. In higher resolution simulations, the bottom velocity stream functions uniquely feature intense recirculations to the east of the Drake Passage.

2.4.4 Sensitivity of the thermal wind component to resolution

In the previous section we note that the depth-varying component of the flow can be closely described by the thermal wind relation and ultimately related to horizontal density gradients. To understand why the thermal wind component of the gyre and the ACC is particularly strong at eddy-permitting resolutions, we study the isopycnal structure at various resolutions. Zonal averages of the density are calculated over five meridional sections: Channel (-2000 $< x <$ -1000 km), West Ridge (500 $< x <$ 1000 km), East Ridge (2000 $< x <$ 2500 km), East of the ridge (3500 $< x <$ 4000 km), and the full zonal average. The locations of these sections are shown in Figure 2.6e.

Figure 2.11 compares the isopycnal structure between an eddy-permitting (10 km) and an eddy-parameterized (80 km) simulation with rough bathymetry. The isopycnal structure for simulations with a smooth bathymetry are qualitatively similar. In all meridional sections, the isopycnals are more tilted in the eddy-permitting

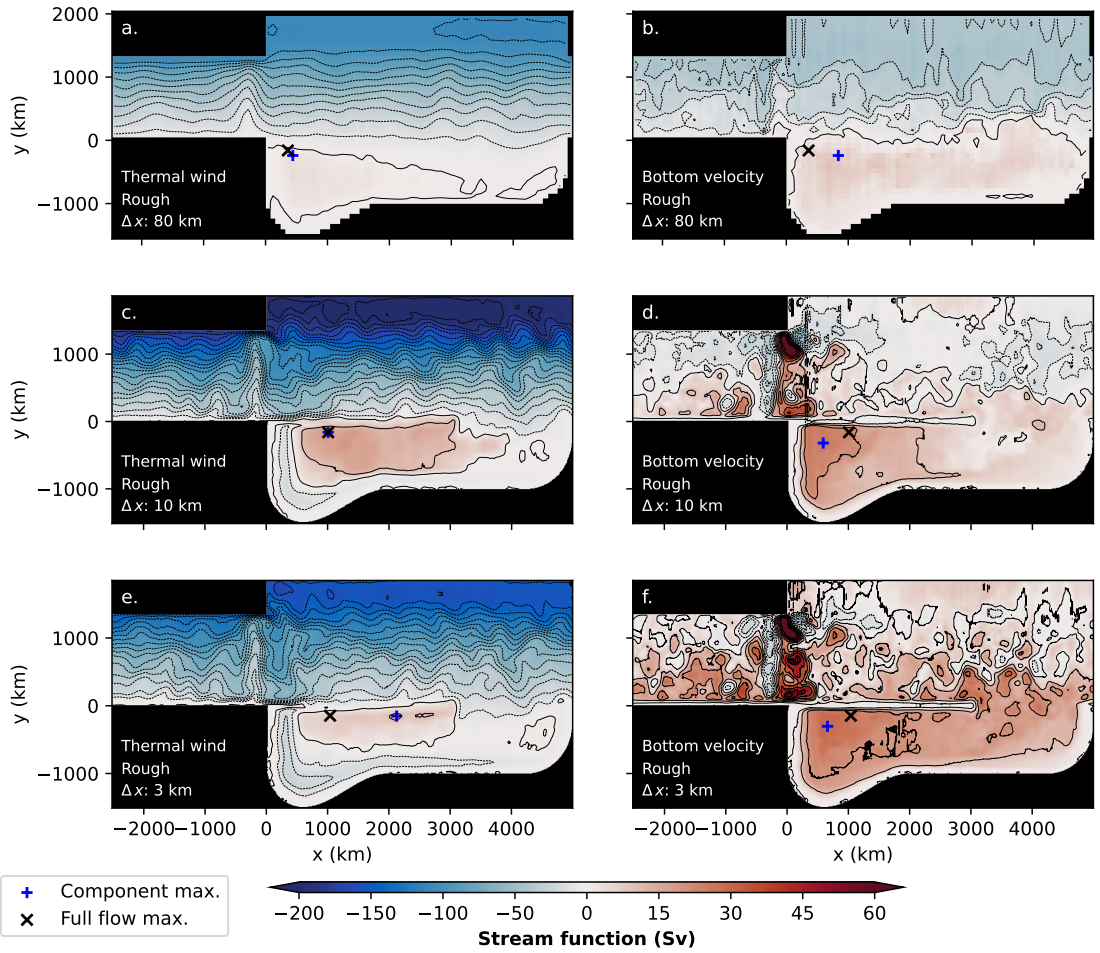

Figure 2.10: Stream functions from the same decomposition shown in Figure 2.9 at various resolutions. The black contours have an interval of 10 Sv. Results are from configurations with a rough bathymetry. The combined thermal wind and bottom velocity stream function is approximately equal to the total stream function, shown in Figure 2.7. Blue crosses mark the location of the component stream function maximum in the gyre basin. Black crosses mark the location where the total gyre transport is calculated.

simulation. In particular, meridional density gradients over the submarine ridge are large at eddy-permitting resolutions and the stratification of the gyre basin ($y < 0$) is reduced. At eddy-permitting and eddy-rich resolutions, the submarine ridge plays a large role in setting the nearby stratification; this is in agreement with observations (such as Figure 2.1b) and the findings of Wilson et al. (2022). From Figure 2.11 we can conclude that the thermal wind component of the gyre and ACC transports is larger in eddy-permitting models as density gradients are more extreme in the upper 2000 m of the model. A thick and weakly stratified layer also emerges

in the eddy-permitting simulations, which is approximately below the 1028.5 kg m^{-3} contour. In this layer, horizontal density gradients are small and the thermal wind relation suggests that the zonal flow is not expected to vary significantly with depth.

Figure 2.12 compares the isopycnal structure between an eddy-rich (3 km) and the same eddy-permitting (10 km) simulation with rough bathymetry. The isopycnals of the eddy-rich and eddy-permitting simulations share similar features, however meridional density gradients are smaller in the eddy-rich case. This is particularly noticeable above the submarine ridge and ultimately reduces the thermal wind transport of the gyre and ACC in the upper 2000 m of the model. The reduced outcropping of isopycnals in the eddy-rich model also increases the stratification of the gyre basin and reduces the thickness of the weakly stratified layer (approximately below 1028.5 kg m^{-3} contour). In simulations with explicit eddies, the densest isopycnals outcrop approximately 200 km south of the submarine ridge. In this area, the wind stress curl is at its peak negative value and there is little buoyancy forcing (see Figures 2.2c and d). It is therefore possible that there is an Ekman control on the maximum surface density in the gyre basin.

Such large horizontal density gradients are uncommon in eddy-parameterized models. The eddy-parameterized models (80 and 40 km) include the strongest tracer diffusion terms, and eddy schemes like the GM parameterization simulate the effect of unresolved eddies by flattening isopycnals. In the presented simulations (and many climate models), the diffusion parameters and the parameterized eddies are insensitive to topographic features and consequently the isopycnals are relatively flat over the submarine ridge and the gyre basin. In reality, eddy diffusivity can be significantly reduced over large topographic features (Isachsen, 2011). Early work built on the modified quasi-geostrophic Eady (Eady, 1949) and Phillips (Phillips, 1954) models argues that the ratio of the topographic slope and the isopycnal slope governs the baroclinic stability of along-slope currents (Blumsack and Gierasch, 1972; Isachsen, 2011; Mechoso, 1980). The quasi-geostrophic theory predicts that baroclinic instabilities are less intense when the isopycnals and sea floor tilt in the opposite direction. This effect is potentially demonstrated in our eddy-rich

simulation as well; in Figure 2.6c, the eddy kinetic energy reduces by an order of magnitude above the southern side of the submarine ridge where the isopycnal tilt opposes the tilt of the ridge. Other studies however suggest that the ratio between the slope width and the internal deformation radius determines the baroclinic instability (e.g. Hetland, 2017; Stern et al., 2015).

The eddy-permitting simulations are significantly less diffusive than the eddy-parameterized experiments and no eddy parameterization is used. The partially resolved eddy field is insufficient to flatten the isopycnals to the same extent as the eddy-parameterized models and therefore more extreme density gradients emerge. In the eddy-rich simulation (3 km), diffusive terms are small, but the near-resolved mesoscale eddy field is able to flatten the density surfaces more effectively than the partially-resolved eddy field. In Section 2.4.5, we test if various applications of GM in eddy-permitting models can change our results.

2.4.5 Using GM at eddy-permitting resolutions

In the results shown so far, all eddy-permitting simulations do not use the GM parameterization. In this subsection we investigate how strong to weak applications of GM affect our gyre and ACC transports at eddy-permitting resolutions. In simulations with 10 and 20 km horizontal grid spacings and rough bathymetry, the GM diffusivity parameter was varied from 35 m^2s^{-1} up to 2000 m^2s^{-1} (the value used in lower resolution simulations). The results of this sensitivity experiment are shown in Figure 2.13.

At both eddy-permitting resolutions (Figure 2.13a and 2.13d), the gyre transport decreases as the strength of the GM parameterization increases. Up until the strongest application of GM, the thermal wind component of the gyre transport weakens, suggesting the density surfaces are flattening in response to the increased GM diffusivity. When the GM diffusivity equals 2000 m^2s^{-1}, the residual of the thermal wind decomposition is significant, making it difficult to assess the relative importance of the thermal wind transport. The general weakening of the

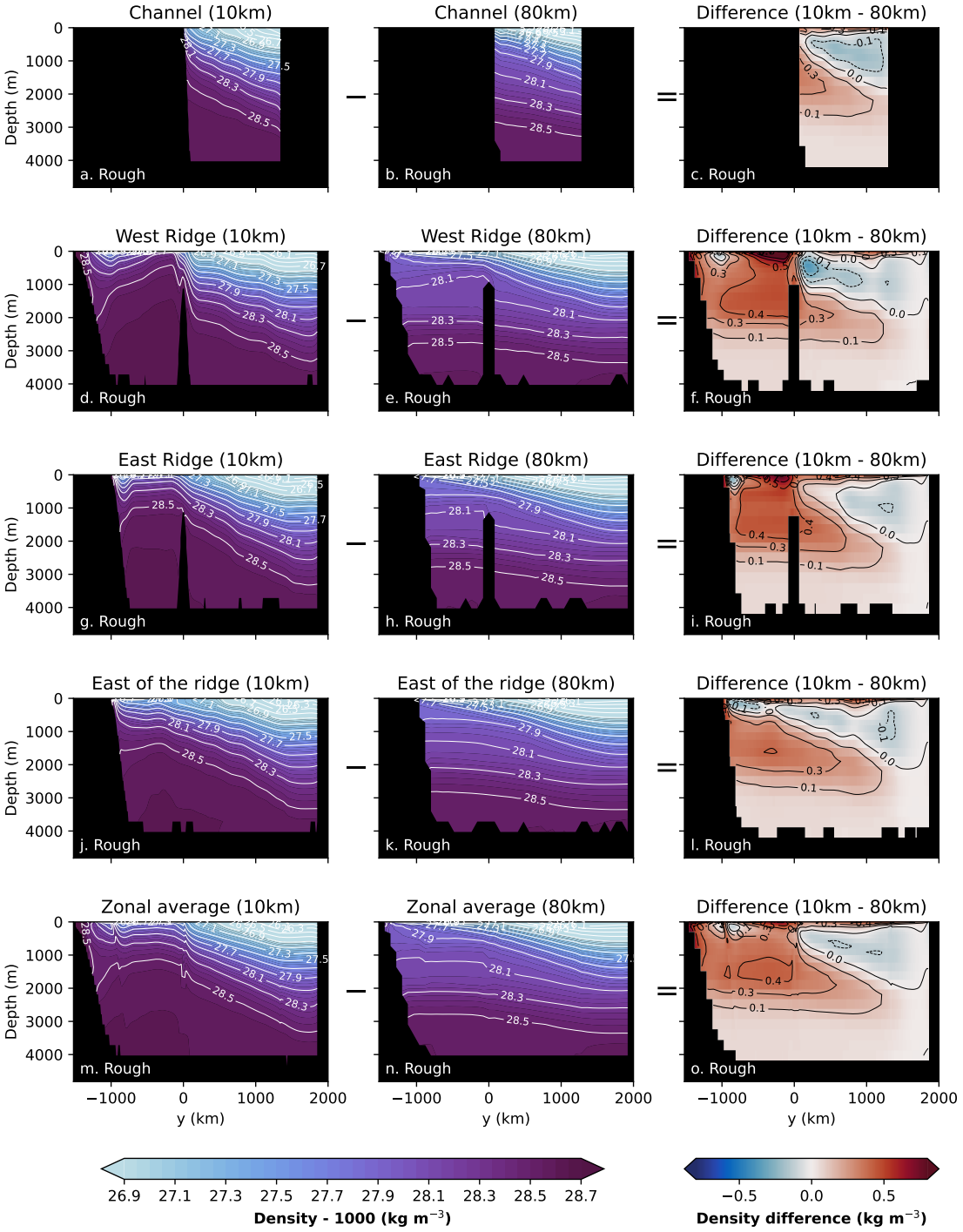

Figure 2.11: Meridional density sections of an eddy-permitting (10 km, left column) and an eddy parameterized (80 km, middle column) simulation. The difference between the density sections are shown in the right column. All presented sections feature a rough bathymetry.

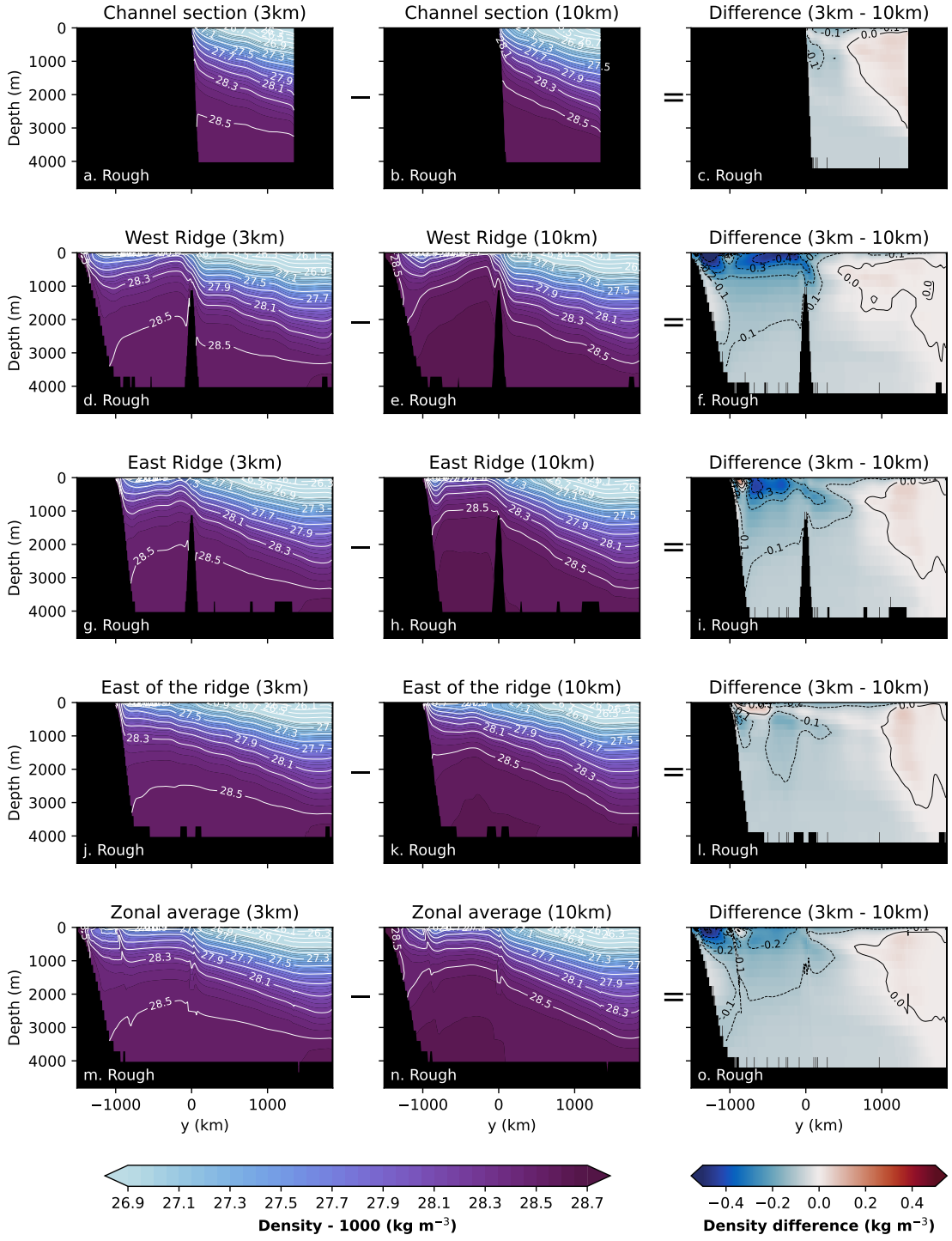

Figure 2.12: Meridional density sections of an eddy-rich (3 km, left column) and an eddy-permitting (10 km, middle column) simulation. The difference between the density sections are shown in the right column. All presented sections feature a rough bathymetry.

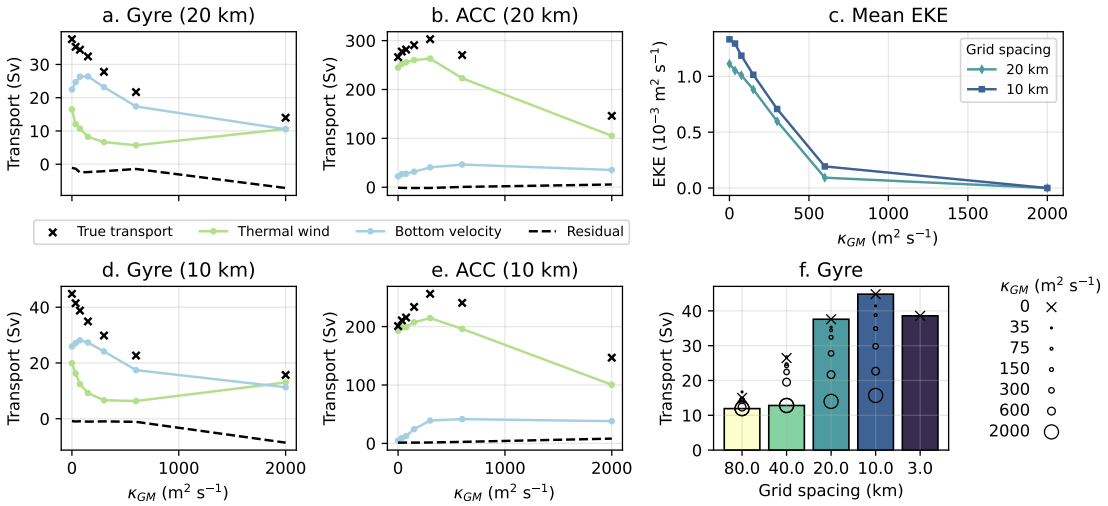

Figure 2.13: The effect of using GM in eddy-permitting models. (a) and (d) show the transport of the Weddell Gyre with applications of GM at various strengths alongside the thermal wind decomposition. (b) and (e) show the transport of the ACC with applications of GM at various strengths alongside the thermal wind decomposition. (c) is the mean eddy kinetic energy when the GM diffusivity parameter is varied. (f) compares the various gyre transports when GM is applied to the transports shown in Figure 2.7c. The strength of GM is similarly varied in the eddy-parameterized models and the effect on the gyre transport is shown in (f).

gyre transport is accompanied by a reduction in the overall eddy kinetic energy of the model (Figure 2.13c).

Figure 2.13f contextualises these eddy-permitting results. We find that weak applications of GM (75 m^{2}s^{-1} or less) in eddy-permitting models can improve their agreement with eddy-rich models at the expense of some explicit eddy kinetic energy. Stronger applications of GM (600 m^{2}s^{-1} or more) in eddy-permitting models can improve their agreement with the eddy-parameterized models but reduces the explicit mean eddy kinetic energy by an order of magnitude. In Figure 2.13f, the gyre transport still slowly increases with resolution when a GM diffusivity of 2000 m^{2}s^{-1} is used. In the absence of explicit eddies, this slow increase is likely a result of increased resolution of the mean flow, increased resolution of the bathymetry, or the linear variation of the momentum and tracer diffusivity with horizontal grid spacing.

For completeness, we also show in Figure 2.13f what happens to the gyre transport when the GM parameter is similarly varied in eddy-parameterized models. In the 80 km case, the gyre transport was insensitive to variations in the GM

parameter and has a maximum value of 16.7 Sv when the GM parameter is 35 m^2s^{-1}. In the 40 km case, the gyre transport is more sensitive to the variation in the GM parameter and has a maximum value of 26.8 Sv when the GM parameter is 35 m^2s^{-1}. Significantly reducing the strength of GM in eddy-parameterized models (from 2000 to 75 m^2s^{-1} or less) can increase the gyre transport but does not lead to agreement with the eddy-rich simulations.

Figure 2.13f shows that in our experiment, no selection of GM diffusivities can produce a consistent gyre transport between all horizontal resolutions. Using different applications of GM (e.g. spatially varying diffusivities) and altenative parameterizations may yield different results. Exploring these approaches with the model would be a valuable contribution to the ocean modelling community but is beyond the scope of the present study.

2.5 Discussion

In the previous section, we related the thermal wind component of the gyre and ACC transports to the density structure. In contrast, it is not immediately clear why the transport from the bottom flow can vary significantly with resolution. To explore this sensitivity of the bottom flow to resolution, we discuss the potential contributions of non-linear eddy-mean flow interactions. We will then discuss other physical processes that are neglected in our idealized model.

2.5.1 Role of eddies

In this chapter, we observe that the density surfaces of the idealized Weddell Gyre change significantly when explicit eddies are introduced to ocean simulations and that the density structure has a significant influence on the horizontal circulation. In the presence of rough bathymetry, the thermal wind component of the gyre transport intensifies in simulations with explicit eddies because the meridional density gradients are steeper. In Figure 2.6, we see large eddy kinetic energies in areas where the isopycnal tilt is the most extreme. This suggests that the

increase in the mean available potential energy that comes with steeper isopycnals can fuel more energetic mesoscale eddies.

A component of the mesoscale eddy field extends to the sea floor, as shown by the vertical bands of eddy kinetic energy in Figure 2.6. It therefore seems likely that explicit mesoscale eddies are influencing the bottom flow in select areas of the model (e.g. between 1000 and 500 km south of the submarine ridge in Figure 2.6b). In the presence of variable bottom topography, mesoscale eddies can drive a mean circulation along topographic contours (Bretherton and Haidvogel, 1976). This can be interpreted either as an 'entropic force' (Holloway, 1987; Holloway, 1992) or, alternatively, as energetically constrained mixing of potential vorticity over the sloping topography (Adcock and Marshall, 2000; Bretherton and Haidvogel, 1976). In Stewart et al. (2019), a simulated Antarctic Slope Current is partially accelerated by mesoscale eddy vorticity fluxes. These eddy-driven flows are not captured by eddy parameterizations employed in climate models based on GM. However, it is possible that these entropic forces are captured in our simulations with explicit eddies, consistent with the strengthening of the topostrophic bottom flow at higher resolutions. This deserves further investigation, a potential vorticity budget budget could identify an eddy mechanism, but this is beyond the scope of the present study.

As eddy-permitting models become more feasible for climate projections, there is an increasing interest in developing eddy parameterizations for simulations where the largest eddies are at least marginally resolved. The development and testing of eddy parameterizations is a busy area of research; Hewitt et al. (2020) review the various approaches that could be deployed in eddy-parameterized and eddy-permitting ocean models. Of particular relevance to the Weddell Gyre is a recent study by Wei et al. (2022) which finds encouraging results for parameterized mesoscale eddy buoyancy fluxes over large scale bathymetry when topographic suppression effects are incorporated.

2.5.2 Missing physics in the idealized configuration

Before concluding on the results presented in this chapter, it is important to summarize the limitations of the idealized model. Firstly, the winds in these configurations are zonal and do not follow the continental shelf. This may be the reason why the density driven slope current in this model does not reach the Drake Passage; additionally, a complete slope current may require deep passages in the zonal submarine ridge. Preliminary tests suggest that deep passages may be problematic with the present configuration design. When a single deep passage is introduced to the submarine ridge at eddy-permitting resolution, the gyre circulation leaks through and interacts with the unrealistic meridional sill in the Drake Passage.

In Figure 2.12, the isopycnals tilt upwards when above the continental shelf. This suggests that dense water is being exported everywhere along the shelf. In reality, dense water export is more localized and isopycnals would tilt down above the continental shelf in East Antarctica (Thompson et al., 2018). Non-linearities in the equation of state may also be important for AABW formation (Gill and Niller, 1973), so using a linear equation of state may lead to inaccurate densities. Presently, it is unclear if a more accurate slope current would modify the gyre transport significantly.

We imitate the time-averaged effect of ice with an effective freshwater flux shown in Figure 2.2d but no attempt is made to couple the effect of sea ice to the oceanic or atmospheric state. Neme et al. (2023) (currently under review), find that the wind-driven export of sea ice can influence the Weddell Gyre transport. In Neme et al. (2023), the long term gyre transport decreases when surface winds are intensified as increased sea ice export flattens the gyre's density surfaces. In both our experiments and Neme et al. (2023), the gyre's transport is determined by thermal wind balance. The effect of internal stresses in the ice can modify the surface stress experienced by the ocean. By neglecting internal stresses, we are assuming that all ice is in 'free drift' which may not be valid near the continental shelf according to satellite observations (Kimura, 2004; Kwok et al., 2017). In reality, the Weddell Gyre and ACC are exposed to an extreme seasonal cycle which significantly varies the gyre's transport (Neme et al., 2021) and density structure on the western boundary (Hattermann,

2018). The seasonal variability of the wind stress and buoyancy forcing can be larger than the time-averaged forcing. In this work we are assuming that time-averaged forcing will accurately produce a time-averaged Weddell Gyre and ACC, but this may not be true because of non-linear processes. This is certainly not true for the subpolar gyres in the northern hemisphere, where winter conditions play a disproportionately large role in setting the properties of the deep ocean thermocline as waters subducted at any time outside of late-winter are re-entrained by the dynamic mixed layer (Stommel, 1979). A similar mechanism also operates on an inter-annual time scale in the northern hemisphere (MacGilchrist et al., 2021). This may be relevant when considering modes of atmospheric variability such as the SAM. It is unclear if a similar selection process ('Stommel's Demon') is present in the Southern Ocean and needs further investigation (see Chapter 4). All experiments used in this study are in a statistically steady state (see Figure 2.4), unlike the real ocean which is exposed to an extreme seasonal cycle, a changing global ocean, and a changing climate. Despite the static forcing, the eddy-rich simulations presented in this chapter still produce a qualitatively similar time-averaged density structure (Figures 2.11 and 2.12) to observations (Figure 2.1b). The time-averaged thermal wind component of the gyre transport only depends on the time-averaged density structure. We therefore believe that the sensitivity of the thermal wind component of the gyre transport is relevant when considering transient forcing as well.

The large-scale topographic features in the model (shown in Figure 2.2a) are qualitatively similar to the Weddell basin but there are some important differences. Firstly, the submarine ridge and the northern boundary of the domain are zonal. The meridional components of the idealized Weddell Gyre and ACC are too constrained by bottom topography when compared to the real ocean. In reality, the ACC is deflected northwards immediately upon exiting the Drake Passage (Mazloff et al., 2010) which is a behaviour this idealized model cannot recreate as any northward deflection of the ACC is limited by the sponge region. Finally, a unique feature of the Weddell Gyre is its dynamic shape as no obvious topographic feature constrains the gyre's eastern boundary (Vernet et al., 2019). In our idealized

simulations, the zonal extent of the Weddell Gyre is not able to extend beyond the width of the basin (5000 km) without taking a northward departure into the ACC channel. It is unclear why there are significant levels of eddy kinetic energy on the eastern margins of the gyre basin (see Figure 2.6) but this may be an unrealistic consequence of the periodic model design.

2.6 Conclusions

Using a minimal description of the Weddell Gyre and ACC, we have identified an extreme sensitivity of the circulation to horizontal grid spacing between eddy-parameterized and eddy-permitting resolutions. The Weddell Gyre in eddy-permitting simulations is significantly stronger than in eddy-parameterized cases and slightly stronger than an eddy-rich case (Figure 2.7). This is concerning as coupled climate models are beginning to traverse this highly sensitive 'gray zone', where large mesoscale eddies are only partially resolved.

To investigate if the gyre transports are affected by the varying ACC strength, we performed a sensitivity experiment in Section 2.4.2. The channel topography was modified to either increase or decrease the ACC transport at eddy-parameterized and eddy-permitting resolutions and the effect on the Weddell Gyre was negligible (Figure 2.8). The limited coupling of the gyre and ACC transports was useful for our study but the insensitivity itself is also scientifically interesting and should be investigated further. If the real Weddell Gyre is insensitive to variations in the depth-varying ACC transport, then the southern boundary density of the ACC may be controlled by subpolar gyre processes.

To improve our understanding of the flow's vertical structure, we used a thermal wind decomposition in Section 2.4.3 which works well with a small residual (Figure 2.9). In cases with a smooth bathymetry, the gyre strength is almost entirely determined by the depth-independent, bottom flow transport, $\mathbf{u}_b H$. When a rough bathymetry is used, the bottom gyre transport is comparable in size to the thermal wind transport, which varies with depth. Although the total transport sensitivity to resolution is similar with smooth and rough bathymetry, the vertical and horizontal

structure of the flow clearly differs. This highlights how permitting small topographic interactions everywhere in an idealized model can change large scale circulation features. In the case of non-zero topographic noise, it is possible that the Weddell Gyre transport is frictionally controlled in a similar way to the ACC (Marshall et al., 2017). A future study using a similar configuration could investigate how the magnitude and form of topographic noise influences the gyre transport.

With a rough bathymetry, the thermal wind component of the gyre is particularly large over the submarine ridge (Figure 2.11 and 2.12). This is a behaviour which was found in the work of Wilson et al. (2022) and in hydrographic sections (such as Figure 2.1b). Wilson et al. (2022) found that the submarine ridge plays a fundamental role in setting the stratification and circulation of the Weddell Gyre and the ACC. This result holds true in our experiments at eddy-permitting and eddy-rich resolutions. However, we would need to study simulations without the submarine ridge to fully assess its impact on the gyre at various resolutions. The presence of the ACC's sloping density surfaces and zonally-elongated submarine ridges may be an important difference between subpolar gyres in the northern and southern hemisphere. The thermal wind component of the gyre is largest at eddy-permitting resolutions because the partially-resolved eddy field is less effective at flattening isopycnals than a fully-resolved eddy field or an eddy parameterization. In all cases, the bottom flow transport of the gyre increases significantly when explicit eddies are present. In this chapter, the quantity of interest has been the rotational gyre transport but the significant sensitivity of the gyre's density structure to the resolution of mesoscale eddies may also influence other important gyre variables. The sensitivity of divergent quanitities such as the overturning and meridional heat transport should be studied using a similar model in future work.

In Section 2.4.5, we showed that using a weak application of the GM parameterization can bring eddy-permitting gyre transports down to eddy-rich values at the expense of some explicit eddy kinetic energy (Figure 2.13). Only a strong application of GM can significantly reduce the gyre's extreme sensitivity to horizontal resolution between eddy-parameterized and eddy-permitting scales and this would be at the

expense of practically all explicit eddy kinetic energy. We also varied the strength of GM in the eddy-parameterized models and found that judicious choices of the GM parameter can minimise the gyre transport's sensitivity to resolution. However, no selection of GM parameters can avoid a factor of 3-4 difference in the gyre transport between the coarsest and finest resolutions.

In this study, the Weddell Gyre transport is largest and the isopycnals are the steepest at eddy-permitting resolutions. For this reason, ocean modellers should approach this eddy-permitting 'gray zone' with care when simulating the Southern Ocean and consider employing parameterizations that are compatible with partially resolved mesoscale eddies.

2.7 End of chapter remarks

In this chapter, we have shown that an idealized Weddell Gyre is sensitive to the effect of mesoscale eddies and is surprisingly insensitive to the strength of an idealized ACC. We have also highlighted the importance of adopting eddy parameterizations designed for eddy-permitting models. An intuitive next step is to use vorticity diagnostics to identify the relevant forces responsible for spinning up the Weddell Gyre. When integrated within a large area, the dynamics of a circulation, realistic or idealized, can be straightforward to interpret. In the next chapter, we apply these diagnostics to a realistic simulation of the Weddell Gyre and discover a major limitation of the C-grid.

3

Spurious Forces in the Vorticity Budget of Ocean Gyres

Contents

In this chapter, we use vorticity diagnostics to identify which model forces spin up a realistic simulated Weddell Gyre as well as a commonly used double gyre configuration. While using these diagnostics, we discovered a significant spurious force which emerges from the C-grid discretization. This newly discovered spurious force is of comparable magnitude to contributions from the wind stress and completely corrupts the vorticity budget of the Weddell Gyre. The content of this chapter is based on a published paper in the *Journal of Advances in Modeling Earth Systems* (Styles et al., 2022), which explores the origins of the spurious force and potential methods to mitigate it. I took the lead on this research project by developing the vorticity diagnostics, decomposing the spurious contributions, conducting experiments in the double gyre configuration, and writing the paper.

3.1 Introduction

Accurately representing the sea floor has always been a challenge for the ocean modelling community. Quantifying the full influence of the sea floor on model circulations is important for both future model development and the interpretation of results from existing models. We present a diagnostic method that reveals how bottom topography influences the depth-integrated vorticity budget of general circulation models (GCMs) and we identify significant spurious forces that emerge from the discrete Coriolis force when calculated on a C-grid (Mesinger and Arakawa, 1976) using z-coordinates.

The recent article by Stewart et al. (2021) also studied the impact of bottom topography on vorticity budgets. However, the model used by Stewart et al. (2021) is a two layer isopycnal model where the bottom topography is completely contained in the lower density layer. In this chapter we consider models that have a higher

vertical resolution and a step-like bathymetry. It is in these more commonly used models that we identify a new category of spurious forces.

The textbook theory of gyres relies on the idea of a depth-integrated vorticity budget and gyres can be classified by the leading order terms in the depth-integrated vorticity equation. For example, the Stommel (1948) gyre is dominated by wind stress curl, lateral bottom friction, and the beta effect. In another example, Niiler (1966) analytically integrated the vorticity equation over the area enclosed by gyre streamlines to study inertial gyres dominated by the wind stress curl, the advection of vorticity, and lateral bottom friction.

GCMs have a primitive momentum equation with an associated vorticity budget. By taking the curl of the depth-integrated terms from the primitive momentum equation we can calculate the corresponding terms in the model's depth-integrated vorticity equation (referred to as vorticity diagnostics hereafter). The vorticity diagnostics can then be integrated over the area enclosed by gyre streamlines to reveal the model forces responsible for spinning the gyre up and down. In this chapter we diagnose the vorticity budget of gyres in two case studies using the NEMO model (Madec et al., 2019). We consider a simple double gyre configuration with analytic forcing and idealized geometry which resembles a North Atlantic basin. We also consider the vorticity budget of the Weddell Gyre in a realistic configuration of the global ocean. In both of these case studies we identify spurious force profiles with different characteristics. In the light of these results, we discuss potential changes to the model discretizations that could mitigate the spurious forces.

The chapter is structured as follows. We first discuss the analytic depth-integrated vorticity budget in Section 3.2 as well as the analytic method of contour integration. In Section 3.3 we consider how the depth-integrated vorticity budget behaves on a C-grid with step-like bathymetry and how spurious terms emerge from the discrete Coriolis acceleration. Results from the analytically forced double gyre model are presented in Section 3.4 and results for the Weddell Gyre are presented in Section 3.5. A discussion of approaches to avoid the spurious forcing terms can be found in Section 3.6. Closing remarks are given in Section 3.7. In

Appendix A, we provide the exhaustive details that support the work presented in this chapter. In Appendix A.1 we derive the depth-integrated vorticity equation and in Appendix A.2 we present the discrete forms of the Coriolis acceleration for various vorticity schemes. Appendix A.3 presents results from the double gyre model using various forms of the discrete Coriolis acceleration. Appendix A.4 presents contour integrations of uninterpolated diagnostics from the double gyre model.

3.2 The analytic vorticity budget

3.2.1 The depth-integrated vorticity equation

Vorticity diagnostics are an underused tool for interpreting model circulations and offer a description of gyre dynamics that complements textbook theory (Vallis, 2017). A handful of recent papers have used a vorticity budget to diagnose regional and global GCM models (Hughes and de Cuevas, 2001; Le Bras et al., 2019; Le Corre et al., 2020; Schoonover et al., 2016; Yeager, 2015).

To obtain a depth-integrated vorticity budget analytically we start from the vector-invariant form of the momentum equation:

$$\frac{\partial \mathbf{u_h}}{\partial t} = -\left[(\nabla \times \mathbf{u}) \times \mathbf{u} + \frac{1}{2}\nabla\left(\mathbf{u}\cdot\mathbf{u}\right)\right]_h - f\left(\hat{\mathbf{k}} \times \mathbf{u}\right)_h - \frac{1}{\rho_0}\nabla_h P + \mathcal{F}^{\mathbf{u}} + \mathcal{D}^{\mathbf{u}}, \quad (3.1)$$

where f is the Coriolis parameter, $\mathbf{u}_h$ is the 'horizontal' (parallel to the Earth's surface) velocity vector, $\mathcal{F}^{\mathbf{u}}$ is the vertical divergence of the vertical diffusive momentum fluxes (which relates to the surface momentum fluxes when vertically integrated), $\mathcal{D}^{\mathbf{u}}$ is the horizontal divergence of the horizontal diffusive momentum fluxes, ∇_h is the horizontal gradient operator, and $[\,\cdot\,]_h$ is the horizontal component of a vector. To derive a depth-integrated vorticity equation, we need to depth-integrate and take the curl of Equation 3.1. The order of the two operations and any multiplications carried out significantly alters the form and physical meaning of the obtained depth-integrated vorticity equation.

If we choose to depth-integrate the curl of the momentum equation, the pressure gradient vanishes upon taking the curl and bottom vortex stretching (neglecting contributions from the relative vorticity which is reasonable when the Rossby number

is small) represents the interaction of the currents with the sea floor. Both the beta effect and bottom vortex stretching originate from the Coriolis acceleration in Equation 3.1. In the model, the curl of the single momentum diagnostic associated with the Coriolis acceleration will be responsible for two distinct physical processes. Jagannathan et al. (2021) use this form of vorticity budget to investigate flow interactions with idealized bathymetry. In Section 3.6.2 we discuss whether the spurious forces identified in this chapter emerge in this vorticity budget.

If we choose to take the curl of the depth-*averaged* momentum equation then sea floor interactions are represented by the JEBAR term (Joint Effect of Baroclinicity and Relief). Cane et al. (1998) and Drijfhout et al. (2013) have questioned the relevance of JEBAR by presenting simple examples in which there is no flow immediately above the bathymetry. In these examples there is trivially no interaction between the flow and the bathymetry, but there is a non-zero JEBAR term.

Throughout this chapter we consider the vorticity equation obtained by taking the curl of the depth-integrated momentum equation:

$$\begin{aligned}\frac{\partial}{\partial t}\left(\nabla\times\mathbf{U}\right)\cdot\hat{\mathbf{k}} = &\underbrace{-\nabla_h\cdot\left(f\mathbf{U}\right)}_{\text{Planetary Vort.}} + \underbrace{\frac{1}{\rho_0}\left(\nabla P_b\times\nabla H\right)\cdot\hat{\mathbf{k}}}_{\text{Bottom pressure torque}} + \underbrace{\frac{1}{\rho_0}\left(\nabla\times\boldsymbol{\tau}_{\text{top}}\right)\cdot\hat{\mathbf{k}}}_{\text{Surface stress curl}} \\ &\underbrace{-\frac{1}{\rho_0}\left(\nabla\times\boldsymbol{\tau}_{\text{bot}}\right)\cdot\hat{\mathbf{k}}}_{\text{Bottom friction}} + \underbrace{\mathcal{D}^{\zeta}}_{\text{Lateral diffusion}} \\ &\underbrace{-\nabla_h\cdot\left(\int_{-H(x,y)}^{\eta(x,y,t)}\zeta\mathbf{u}\,dz\right) - \left[\nabla\times\left(\int_{-H(x,y)}^{\eta(x,y,t)}\frac{1}{2}\nabla_h\left(\mathbf{u}_h^2\right) + w\frac{\partial\mathbf{u}_h}{\partial z}\,dz\right)\right]\cdot\hat{\mathbf{k}}}_{\text{Advection}}. \end{aligned} \tag{3.2}$$

Here ζ is the vertical component of the vorticity, $\boldsymbol{\tau}_{\text{top}}$ is the surface stress due to wind and sea ice, $\boldsymbol{\tau}_{\text{bot}}$ is the bottom stress due to friction at the sea floor, $\mathcal{D}^{\zeta}$ is the lateral diffusion of depth-integrated relative vorticity, η is the free surface height, H is the depth of the sea floor, and P_b is the pressure at the sea floor. In Equation 3.2 we omit the contribution from free surface undulations as we assume the time evolution of the free surface is small and we omit atmospheric pressure torques as

we are assuming there are no atmospheric pressure gradients above the ocean. The derivation of Equation 3.2 (including the omitted terms) is presented in A.1.

The terms on the right-hand side of Equation 3.2 are the following: the advection of planetary vorticity; the bottom pressure torque; the surface stress curl; the curl of bottom friction; the lateral diffusion of relative vorticity; and the advection of relative vorticity (including negligible components of vortex stretching when the Rossby number is small). The planetary vorticity term in Equation 3.2 contains contributions from the evolving free surface and surface water fluxes as $\nabla_h \cdot \mathbf{U} = -\partial\eta/\partial t + Q/\rho_0$, where Q is the surface water flux due to evaporation, precipitation, and run-off. In an equilibrated state, the free surface evolution is small and the divergence caused by realistic water fluxes is negligible. Hence, we assume $\nabla_h \cdot (f\mathbf{U}) \approx \beta V$ where β represents the linear variation of f with latitude and V is the meridional component of the depth-integrated velocity. This formulation is practical as topographic interactions emerge from pressure gradients in the form of the bottom pressure torque and beta effects emerge from the curl of the Coriolis acceleration; the Coriolis acceleration is responsible for one physically meaningful term in the analytic vorticity budget. Equation 3.2 is also used in Stewart et al. (2021).

Jackson et al. (2006) conclude that the leading order balance between bottom pressure torques and the planetary vorticity term in Equation 3.2 is crucial for steering jets and western boundary currents over bottom topography. They further argue that the form of the topographic steering determines if bottom friction is able to modify the geometry of the current.

As a consequence of Stokes' theorem, the area integral of a term from Equation 3.2 is directly related to the line integral of the depth-integrated forces along the area edge. This is particularly useful when considering area integrals of terms from the vorticity equation and is discussed further in the next sub-section.

3.2.2 Contour integration method

All terms in the depth-integrated vorticity equation can be expressed as the curl of a depth-integrated acceleration in the momentum equation:

$$\Omega = (\nabla \times \mathbf{M}) \cdot \hat{\mathbf{k}}, \tag{3.3}$$

where Ω is a term in the depth-integrated vorticity equation and $\mathbf{M}$ is a term in the depth-integrated momentum equation. If we integrate Ω over the area enclosed by a depth-integrated streamline, we can interpret the integral using Stokes' theorem:

$$I(\psi) = \pm \iint_{A_\psi} \Omega \, dA = \pm \oint_{\Gamma_\psi} \mathbf{M} \cdot \mathbf{dl}, \tag{3.4}$$

where A_ψ is the area enclosed by a depth-integrated streamline and Γ_ψ is the anticlockwise path along the same streamline. The criteria for selecting the sign in Equation 3.4 is defined later in this paragraph. The depth-integrated stream function, ψ, only exists if the flow is steady and $\nabla_h \cdot \mathbf{U} = 0$. If a long time-average of a varying flow is taken and the surface water fluxes are sufficiently small, a quasi-streamline can be calculated which approximately follows the circulation. The integral $\rho_0 I(\psi)$ can be interpreted as the work done per unit area by the force associated with $\mathbf{M}$ on a fluid column in one circulation of Γ_ψ. For a gyre circulating in a clockwise direction, the direction of circulation would be opposite to the conventional anticlockwise direction of Γ_ψ. So that the reader does not have to constantly consider the direction of the flow relative to Γ_ψ we select the sign in Equation 3.4 so a positive value of $I(\psi)$ corresponds to a force that is spinning the gyre up.

Analytically, we would expect the planetary vorticity term to vanish upon integration as a consequence of the divergence theorem:

$$\iint_{A_\psi} \nabla_h \cdot (f\mathbf{U}) \, dA = \oint_{\Gamma_\psi} f\mathbf{U} \cdot \hat{\mathbf{n}} \, dl = 0, \tag{3.5}$$

where $\hat{\mathbf{n}}$ is the horizontal vector which is normal to the streamline and the depth-integrated velocity. The Coriolis force can still play a role in shaping the streamlines of the circulation but ultimately has no influence on the integrated budget. Although the divergent part of the advection term, $\nabla_h \cdot \left(\int \zeta \mathbf{u} \, dz \right)$, has a similar form, we do not expect the same zero integral for this term as the depth-integrated product of ζ and $\mathbf{u}$ is not parallel to $\mathbf{U}$ in general.

This method has been used in models before. Schoonover et al. (2016) integrated vorticity diagnostics over a limited number of streamlines in the North Atlantic and concluded that the wind stress curl is largely balanced by bottom pressure torques. Stewart et al. (2021) also used this method in an isopycnal model and concluded that wind stress curl is not balanced by bottom pressure torques in general. Stewart et al. (2021) discuss how the integrating area affects the resultant vorticity balances and in their model the wind stress curl is only balanced by bottom pressure torques when integrated over latitude bands. Jackson et al. (2006) note that in their idealized models the vorticity input from bottom friction mostly disappears when integrated over latitude bands but can be significant when integrated over the area enclosed by streamlines.

In Gula et al. (2015), terms in the barotropic vorticity budget are integrated over an entire subdomain covering the South Atlantic Bight to study the interaction between the Gulf Stream and the continental shelf. Flow through the boundaries of the nested model is permitted so we would not expect the planetary vorticity term to vanish upon integration. These integrations show a leading order balance between the planetary vorticity term and bottom pressure torques and suggest that bottom pressure torques are the dominant mechanism for removing the planetary vorticity imported into the subdomain by the Gulf Stream.

It should be noted that Schoonover et al. (2016), Stewart et al. (2021), Jackson et al. (2006), and Gula et al. (2015) all use a terrain-following coordinate in their models but in this chapter we study the vorticity budget of a z-coordinate model. In Section 3.6.4 we discuss how the vorticity budget can be affected by the choice of vertical coordinate and how terrain-following coordinates can mitigate spurious Coriolis forces related to the topography.

3.3 The vorticity budget on a C-grid

3.3.1 The discrete depth-integrated vorticity equation

In many contemporary ocean GCMs, the discretized model variables are distributed on the C-grid (Mesinger and Arakawa, 1976). The geometry of the C-grid is shown

in Figure 3.1: T points hold scalar information including the divergence of the flow; the U and V points hold the horizontal components of vector quantities including the horizontal velocity, surface stresses, and accelerations in the momentum equation. Values closely related to vorticity are found on F points, this includes the relative vorticity, the streamfunction, and terms in the depth-integrated vorticity equation (Ω). Vertical velocities are located on W points that are directly above and below T points as shown in Figure 3.1. The Coriolis parameter can be evaluated at any point on the C grid but F point values are used for calculating the Coriolis acceleration in most models that use a vector invariant momentum equation because the relative and planetary vorticity are then evaluated at the same point (see Section 3.3.2). In this chapter, $f_{i,j}$ refers to the value of the Coriolis parameter centred on the F point and $f^u_{i,j}$ ($f^v_{i,j}$) refers to the Coriolis parameter centred on the U (V) point as shown in Figure 3.1.

Every point in the C-grid has an associated cell with a vertical thickness and horizontal width. Throughout this chapter e^{3t} is the T cell vertical thickness and e^{1t}, e^{2t} are the T cell widths in the i and j direction respectively. The same convention is used for U, V, and F cells also. It should be noted that the values of the F cell thicknesses in this chapter depend on the scheme used to calculate the Coriolis acceleration (see Section 3.3.2).

The GCM configurations discussed in this chapter use a primitive momentum equation that is a discrete equivalent to the vector invariant momentum equation (Madec et al., 2019). Momentum diagnostics can be combined to represent terms in the analytic momentum equation (Equation 3.1). The curl of the depth-integrated momentum diagnostics is taken to form a closed discrete vorticity budget that is valid in an unsteady state as the time derivative diagnostic is included. The resultant vorticity diagnostics should closely resemble the terms in the depth-integrated vorticity equation (Equation 3.2); however, the planetary vorticity diagnostic deviates from the planetary vorticity term in several significant ways.

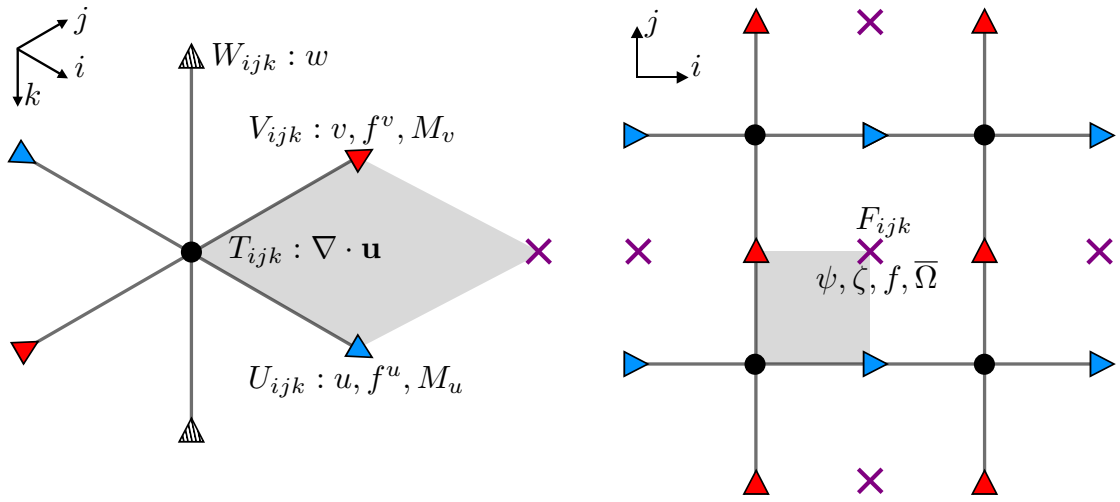

Figure 3.1: The distribution of variables on the C-grid in both a three dimensional (left) and horizontal (right) view. The T, U, V, F, and W points are shown alongside important values that are centred on these points. The T, U, V, and F points at the coordinate (i,j,k) lie on the four corners of the gray square. The variable w is the vertical velocity and M_u, M_v are the x and y components of a term in the momentum equation. Note that k increases downwards.

3.3.2 The discrete Coriolis acceleration

The Coriolis acceleration is a product of the Coriolis parameter, f, and the horizontal velocity $\mathbf{u}_h$. There are many possible schemes for calculating their product and the choice of scheme affects the quantities that are conserved in the model flow.

Consider the following discrete Coriolis acceleration:

$$\begin{aligned} \mathrm{COR}^x_{i,j,k} &= \frac{1}{4}\frac{1}{(e^{1u}e^{3u})_{i,j,k}}\sum_{n=1}^{4} f^v(\mathbf{r}_n)\tilde{V}_k(\mathbf{r}_n), \\ \mathrm{COR}^y_{i,j,k} &= \frac{-1}{4}\frac{1}{(e^{2v}e^{3v})_{i,j,k}}\sum_{n=1}^{4} f^u(\mathbf{r}_n)\tilde{U}_k(\mathbf{r}_n), \end{aligned} \tag{3.6}$$

where COR^x (COR^y) is the x (y) component of the discrete Coriolis acceleration which is centred on a U (V) point; $\tilde{V} = ve^{1v}e^{3v}$ and $\tilde{U} = ue^{2u}e^{3u}$ are volume fluxes; and $\mathbf{r}_n$ points to one of the four neighbouring V or U points. If we depth-integrate the acceleration in Equation 3.6 and then take the curl, we obtain the following equation for the discrete planetary vorticity term:

$$\begin{aligned}\mathrm{PVO}_{i,j,k} = -\frac{1}{4}\frac{1}{\left(e^{1f}e^{2f}\right)_{i,j}}\Big[&\left(f^u U e^{2u}\right)_{i+1,j} + \left(f^u e^{2u} U\right)_{i+1,j+1} \\ &- \left(f^u U e^{2u}\right)_{i-1,j} - \left(f^u U e^{2u}\right)_{i-1,j+1} \\ &+ \left(f^v V e^{1v}\right)_{i,j+1} + \left(f^v V e^{1v}\right)_{i+1,j+1} \\ &- \left(f^v V e^{1v}\right)_{i,j-1} - \left(f^v V e^{1v}\right)_{i+1,j-1}\Big],\end{aligned} \tag{3.7}$$

where PVO is the discrete planetary vorticity term which is centred on an F point. U and V are the depth-integrated velocities in the x and y directions respectively. Equation 3.7 is the discrete calculation of $-\nabla_h \cdot (f\mathbf{U})$ averaged over the four T cells surrounding the central F point and is therefore closely related to the analytic planetary vorticity term in Equation 3.2. The Coriolis acceleration given in Equation 3.6 is not used in C-grid models as it lacks the energy and/or enstrophy conserving properties of other mainstream schemes. However, when studying the discrete depth-integrated vorticity budget it is useful to consider how the used Coriolis accelerations deviate from this reference value as any difference may emerge as a departure from the discrete calculation of $-\nabla_h \cdot (f\mathbf{U})$ in the vorticity budget.

When using a vector invariant momentum equation, mainstream schemes use multi-point and thickness-weighted averaging of f and $\mathbf{u}$ in order to conserve energy and/or enstrophy (Madec et al., 2019). A general form of the discrete Coriolis acceleration under these schemes is:

$$\mathrm{COR}^x_{i,j,k} = \frac{1}{N}\frac{1}{e^{1u}_{i,j}}\sum_{n=1}^{N}\left(\frac{f(\mathbf{a_n})}{e^3_k(\mathbf{b}_n)}\right)\tilde{V}_k(\mathbf{c_n}), \tag{3.8}$$

$$\mathrm{COR}^y_{i,j,k} = \frac{-1}{N}\frac{1}{e^{2v}_{i,j}}\sum_{n=1}^{N}\left(\frac{f(\mathbf{a_n})}{e^3_k(\mathbf{b}_n)}\right)\tilde{U}_k(\mathbf{c_n}), \tag{3.9}$$

where $\mathbf{a}_n$, $\mathbf{b}_n$, and $\mathbf{c}_n$ are the horizontal locations of three neighbouring grid points (not necessarily different) for the n^{th} term of the sum. COR^x and COR^y are still centred on U and V points respectively. Note that $\mathbf{a}_n$ is always the location of an F point and $\mathbf{c}_n$ is always the location of a U or V point. Depending on the scheme, the e^3_k term can be either a U, V, or F cell thickness so $\mathbf{b}_n$ is the location

of either a U, V, or F point respectively. N is the number of terms in the average which depends on the choice of scheme. Equations 3.8 and 3.9 are valid on points near the bathymetry but if $\mathbf{b}_n$ or $\mathbf{c}_n$ points to a masked grid point (a point in the bathymetry) then the n^{th} term in the sum is equal to zero.

In this chapter we consider three popular schemes for calculating the Coriolis acceleration. The energy conserving scheme (ENE) (Sadourny, 1975) conserves total horizontal kinetic energy and uses a four point average (N=4). The enstrophy conserving scheme (ENS) (Sadourny, 1975) conserves potential enstrophy and has eight terms (N=8). Finally the energy and enstrophy conserving scheme (EEN) (Arakawa and Lamb, 1981) conserves both horizontal kinetic energy and potential enstrophy and uses a twelve point average (N=12). Barnier et al. (2006) demonstrates that the choice of scheme can significantly influence the global ocean circulation, especially in areas with strong current-topography interaction.

The explicit forms of the ENE, ENS, and EEN schemes for the Coriolis acceleration are given in Appendix A.2. The results in Section 3.4 and 3.5 use the EEN scheme; however, in Section 3.6.1 we argue that all three schemes produce similar spurious forces. This argument is more concise when we use a form of the Coriolis acceleration that is general to the ENE, ENS, and EEN schemes.

We will decompose the general discrete Coriolis acceleration in Equations 3.8 and 3.9 by considering variations of f and e^3 around the U and V points:

$$f(\mathbf{a}_n) = f(\mathbf{c}_n) + \left[f(\mathbf{a_n}) - f(\mathbf{c}_n)\right], \tag{3.10}$$

$$e^3_k(\mathbf{b}_n) = \frac{1}{\alpha_k(\mathbf{b}_n)} \left(e^{3u}_{i,j,k} + \left[\alpha_k(\mathbf{b}_n) e^3_k(\mathbf{b}_n) - e^{3u}_{i,j,k}\right]\right), \tag{3.11}$$

$$e^3_k(\mathbf{b}_n) = \frac{1}{\alpha_k(\mathbf{b}_n)} \left(e^{3v}_{i,j,k} + \left[\alpha_k(\mathbf{b}_n) e^3_k(\mathbf{b}_n) - e^{3v}_{i,j,k}\right]\right), \tag{3.12}$$

where $f(\mathbf{c_n})$ is the value of the Coriolis parameter centred on the same point as the volume flux. Note that Equation 3.11 and Equation 3.12 both simplify down to the same equation, $e^3_k(\mathbf{b}_n) = e^3_k(\mathbf{b}_n)$, as they are simply alternative ways of expressing $e^3_k(\mathbf{b}_n)$. The form of Equation 3.11 will be applied to COR^x (Equation 3.8) and the form of Equation 3.12 will be applied to COR^y (Equation 3.9). The

$\alpha_k(\mathbf{b_n})$ term is of order one and represents a scaling of e_k^3 relative to other local cell thicknesses that only occurs in the EEN scheme. In the EEN scheme, $e_k^3(\mathbf{b}_n)$ is an F cell thickness and F cell thicknesses are calculated using:

$$e_{i,j,k}^{3f} = \frac{1}{4}\left(e_{i,j,k}^{3t} + e_{i+1,j,k}^{3t} + e_{i,j+1,k}^{3t} + e_{i+1,j+1,k}^{3t}\right), \tag{3.13}$$

where masked T cell thicknesses are set to zero. When near bathymetry (masked points), the F cell thickness could be up to four times smaller than the typical unmasked T cell thicknesses surrounding it. The product $\alpha_k e_k^{3f}$ is the F cell thickness before this scaling is applied and will be more similar to the neighbouring T cell thicknesses in Equation 3.13. This scaling of e^{3f} is unique to the EEN scheme and therefore $\alpha_k = 1$ in the ENS and ENE cases.

By combining Equations 3.8, 3.9, 3.10, 3.11, and 3.12 we can derive a general decomposition of the Coriolis acceleration:

$$\begin{aligned}
\mathrm{COR}_{i,j,k}^{x} = \frac{1}{N}\frac{1}{\left(e^{1u}e^{3u}\right)_{i,j,k}}\sum_{n=1}^{N} f(\mathbf{c}_n)\tilde{V}_k(\mathbf{c_n})\Bigg[1 + \underbrace{\frac{f(\mathbf{a}_n) - f(\mathbf{c}_n)}{f(\mathbf{c}_n)}}_{f\text{ displacement}} \\
\underbrace{-\alpha_k(\mathbf{b}_n)\frac{\alpha_k(\mathbf{b}_n)e_k^3(\mathbf{b}_n) - e_{i,j,k}^{3u}}{e_{i,j,k}^{3u}} + \left[\alpha_k(\mathbf{b}_n) - 1\right]}_{\text{Cell thicknesses}} + \underbrace{\left[\alpha_k(\mathbf{b}_n) - 1\right]\frac{f(\mathbf{a}_n) - f(\mathbf{c}_n)}{f(\mathbf{c}_n)}}_{\text{Coupled } f\text{-topographic}}\Bigg], \\
\mathrm{COR}_{i,j,k}^{y} = \frac{-1}{N}\frac{1}{\left(e^{2v}e^{3v}\right)_{i,j,k}}\sum_{n=1}^{N} f(\mathbf{c}_n)\tilde{U}_k(\mathbf{c_n})\Bigg[1 + \underbrace{\frac{f(\mathbf{a}_n) - f(\mathbf{c}_n)}{f(\mathbf{c}_n)}}_{f\text{ displacement}} \\
\underbrace{-\alpha_k(\mathbf{b}_n)\frac{\alpha_k(\mathbf{b}_n)e_k^3(\mathbf{b}_n) - e_{i,j,k}^{3v}}{e_{i,j,k}^{3v}} + \left[\alpha_k(\mathbf{b}_n) - 1\right]}_{\text{Cell thicknesses}} + \underbrace{\left[\alpha_k(\mathbf{b}_n) - 1\right]\frac{f(\mathbf{a}_n) - f(\mathbf{c}_n)}{f(\mathbf{c}_n)}}_{\text{Coupled } f\text{-topographic}}\Bigg],
\end{aligned} \tag{3.14}$$

where we have assumed that variations in f and the nonscaled cell thickness, $\alpha_k e_k^3$, are small. The x and y components of the Coriolis acceleration have a leading order contribution centred on the U and V point. The leading order term simplifies to the reference Coriolis acceleration in Equation 3.6 and therefore will resemble $-\nabla_h \cdot (f\mathbf{U})$ in the discrete vorticity budget. Equation 3.14 is valid on

points near the bathymetry but if $\mathbf{b}_n$ or $\mathbf{c}_n$ points to a masked grid point then the n^{th} term of the entire sum is equal to zero.

The remaining terms may emerge as first order departures from $-\nabla_h \cdot (f\mathbf{U})$ in the discrete vorticity budget. The first order contributions are: an f displacement term caused by the difference between the values of f where the volume fluxes are located and the values of f used in the scheme; a topographic effect caused by variations in cell thicknesses; and a coupled f-topographic effect caused by the combined effect of sudden changes in cell thicknesses near masked points and the previously mentioned f displacement term. Note that if $\alpha = 1$ (true for ENS and ENE) then the f-topographic effect vanishes.

The depth-integrated Coriolis acceleration is:

$$\begin{aligned} \widehat{\mathrm{COR}}^{x}_{i,j} &= \sum_{k=1}^{k^x_{max}(i,j)} e^{3u}_{i,j,k} \mathrm{COR}^{x}_{i,j,k}, \\ \widehat{\mathrm{COR}}^{y}_{i,j} &= \sum_{k=1}^{k^y_{max}(i,j)} e^{3v}_{i,j,k} \mathrm{COR}^{y}_{i,j,k}, \end{aligned} \tag{3.15}$$

where $k^x_{\max}$ and $k^y_{\max}$ are the highest unmasked indices in the column and they may vary with horizontal index when z-coordinates are used. The depth-integrated Coriolis acceleration is therefore also sensitive to steps in the bathymetry. This is discussed in the next sub-section.

3.3.3 The influence of model level steps on the Coriolis acceleration

In this section, we present a toy configuration that highlights how model levels can influence the discrete Coriolis acceleration. The configuration is shown in Figure 3.2. The configuration has two model levels, three U-grid points in the i direction, two in the j direction, and a rigid lid. The points in the upper level are surrounded by unmasked points, we assume the grid is regular, and cell widths are the same in the i and j direction. We also assume an f-plane so f does not vary.

The configuration has a step bathymetry and a current running alongside it. The current has no y component so $v = 0$ everywhere and therefore $\mathrm{COR}^x = 0$

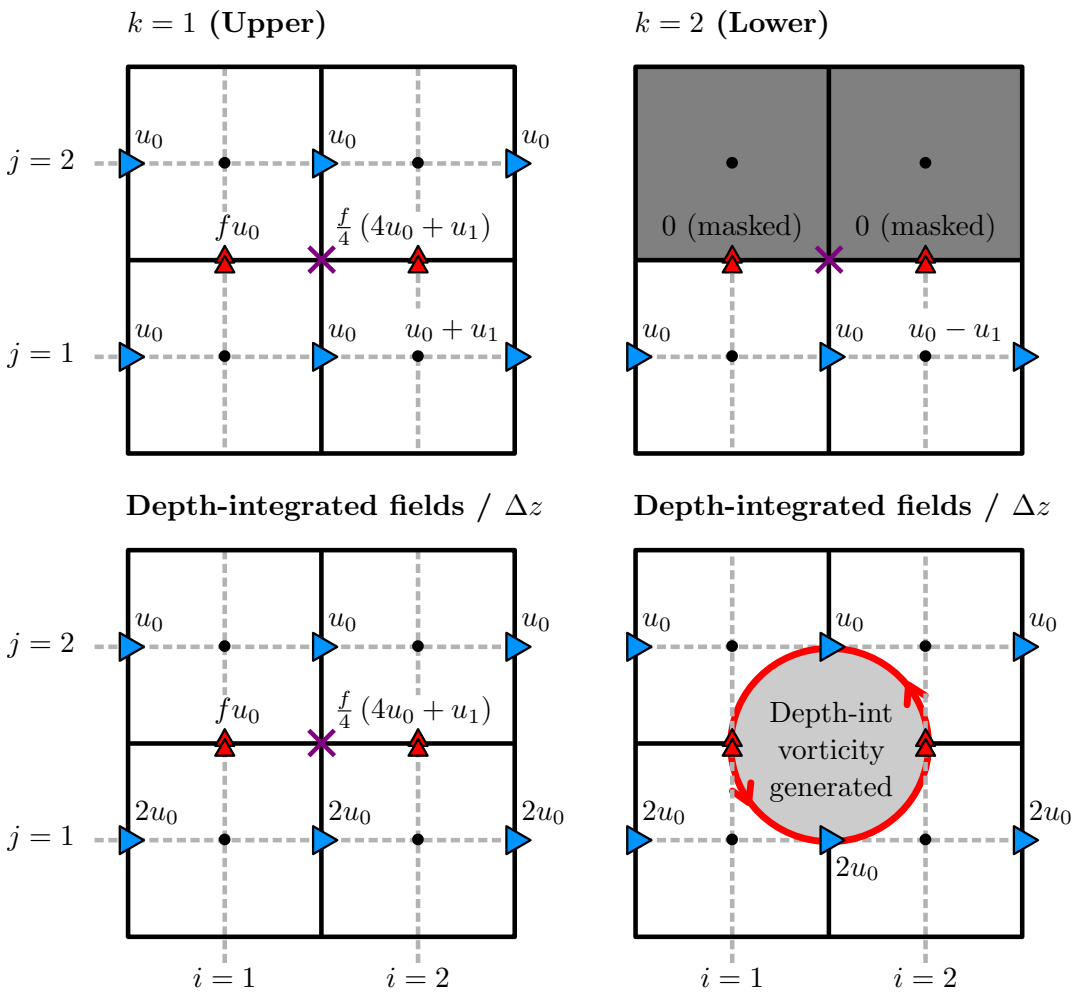

Figure 3.2: A toy model demonstrating how model levels influence the discrete Coriolis acceleration. A horizontal plan is shown for the upper and lower level as well as a view of the depth-integrated fields divided by the cell thickness Δz. Single arrows represent prescribed velocities; double arrows represent calculated Coriolis accelerations; and shaded cells represent bottom topography. Accelerations on the lower level are masked to prevent the velocity field from evolving into a flow that would violate the no penetration boundary condition. The central F point is marked by a cross and is where the depth-integrated vorticity is generated.

at all points. The lower limb of the current decelerates by an amount u_1 and as a consequence of incompressibility a vertical velocity is induced which accelerates the upper current by u_1.

Under these assumptions, the discrete Coriolis acceleration does not vary between the ENE, ENS, and EEN schemes and is:

$$\mathrm{COR}^{y}_{i,j,k} = \frac{f}{4}\left[u_{i,j,k} + u_{i-1,j,k} + u_{i,j+1,k} + u_{i-1,j+1,k}\right], \tag{3.16}$$

which is effectively f multiplied by the four point average of u.

In the upper layer, the Coriolis accelerations, located on the V points marked by red triangles in Figure 3.2, are:

$$\mathrm{COR}^{y}_{1,1,k=1} = f u_0, \tag{3.17}$$

$$\mathrm{COR}^{y}_{2,1,k=1} = \frac{f}{4}\left(4u_0 + u_1\right). \tag{3.18}$$

In the lower layer, the Coriolis accelerations are set to zero as they lie on masked V points. The V points are masked to prevent accelerations into the topography that would violate the no penetration boundary condition. The depth-integrated Coriolis accelerations are:

$$\widehat{\mathrm{COR}}^{y}_{1,1} = \mathrm{COR}^{y}_{1,1,k=1}\,\Delta z, \tag{3.19}$$

$$\widehat{\mathrm{COR}}^{y}_{2,1} = \mathrm{COR}^{y}_{2,1,k=1}\,\Delta z, \tag{3.20}$$

where Δz is the constant cell thickness. It should be noted that u_1 vanishes when calculating the depth-integrated velocities but remains in the depth-integrated acceleration. The depth-integrated Coriolis acceleration depends on more than the depth-integrated velocities.

When we take the curl of the depth-integrated accelerations, we can see how a depth-integrated vorticity is generated:

$$\frac{1}{\Delta x}\left[\widehat{\mathrm{COR}}^{y}_{2,1} - \widehat{\mathrm{COR}}^{y}_{1,1}\right] = \frac{1}{4}\frac{\Delta z}{\Delta x} f u_1, \tag{3.21}$$

where Δx is the constant cell width. Note that this value is located on the central F point shown in Figure 3.2.

The pressure gradient, lateral diffusion term (unless no-slip boundary conditions are used), and the horizontal advection term are ambiguous on the masked velocity points at the edge of the bathymetry (e.g. the V points in the upper right diagram of Figure 3.2). An explicit momentum balance cannot be resolved and the Coriolis

acceleration is the only non-zero and unambiguous acceleration into the sea floor. There should be no net acceleration into the bathymetry or else the no penetration boundary condition would be violated, so all accelerations that are incident on bathymetry are masked and set to zero. The masking of all accelerations can be interpreted as the addition of a spurious term to the discrete Coriolis acceleration. This spurious force is of unclear physical origin and is not realistic as it is localized to grid points that lie near model level steps. We can think of the result in Equation 3.21 as either the curl of this spurious force or as a form of spurious vortex stretching that takes place on F points near model level steps (cf. Bell, 1999).

3.3.4 Decomposing the planetary vorticity term

In Section 3.3.2 we concluded that the discrete Coriolis acceleration used in mainstream schemes contained spurious contributions caused by f displacement, variations in cell thicknesses, and a coupled f-topographic effect. In Section 3.3.3 we demonstrated how spurious contributions from model level steps exist in the depth-integrated discrete Coriolis acceleration. The four found spurious contributions have the potential to emerge in the planetary vorticity diagnostic which is calculated by taking the curl of the depth-integrated Coriolis acceleration:

$$\begin{aligned}\mathrm{PVO}_{i,j} = \frac{1}{\left(e^{1f}e^{2f}\right)_{i,j}}\Big[&\left(\widehat{\mathrm{COR}}^{y}e^{2v}\right)_{i+1,j} - \left(\widehat{\mathrm{COR}}^{y}e^{2v}\right)_{i,j} \\ &- \left(\widehat{\mathrm{COR}}^{x}e^{1u}\right)_{i,j+1} + \left(\widehat{\mathrm{COR}}^{x}e^{1u}\right)_{i,j}\Big].\end{aligned} \tag{3.22}$$

We can therefore express the planetary vorticity diagnostic as the sum of five components:

$$\begin{aligned}\mathrm{PVO}_{i,j} = -\nabla_h \cdot (f\mathbf{U})\,|_{i,j} + f \text{ displacement} + \text{ cell thicknesses} \\ + f\text{-topographic} + \text{ model level steps}\end{aligned} \tag{3.23}$$

where $-\nabla_h \cdot (f\mathbf{U})\,|_{i,j}$ refers to the discrete divergence calculation in Equation 3.7 and is closely related to the analytic planetary vorticity term in Equation 3.2.

Table 3.1: The five different calculations of the planetary vorticity term and the components from Equation 3.23 they include. FD = f displacement term, E3 = Cell thicknesses term, FT = f-topographic term, MLV = Model levels steps term.

Calculation	$-\nabla_h \cdot (f\mathbf{U})$	FD	E3	FT	MLV
Full diagnostic	✓	✓	✓	✓	✓
Assume $f(\mathbf{a}_n) = f(\mathbf{c}_n)$, $e^3 = \text{const}$	✓	✗	✗	✗	✓
Assume $e^3 = \text{const}$	✓	✓	✗	✗	✓
Assume $f(\mathbf{a}_n) = f(\mathbf{c}_n)$	✓	✗	✓	✗	✓
Calculate $-\nabla_h \cdot (f\mathbf{U})$	✓	✗	✗	✗	✗

The remaining terms are departures from the analytic estimate that emerge from using mainstream schemes to calculate the Coriolis acceleration and the masking of velocity points near the stepped bathymetry.

The magnitude of these contributions may vary significantly between configurations so a general method for decomposing the planetary vorticity diagnostic is valuable. In order to calculate the decomposition of the planetary vorticity diagnostic, we calculate the depth-integrated Coriolis acceleration under three different assumptions and then calculate the corresponding contributions to the vorticity budget. An explicit calculation of $-\nabla_h \cdot (f\mathbf{U})\,|_{i,j}$ (Equation 3.7) is also needed. The calculations are listed in Table 3.1 along with the components from Equation 3.23 they include. By linearly combining the fields from each calculation we can isolate each component in Equation 3.23. The f-topographic component is a residual, calculated by finding the difference between the complete planetary vorticity diagnostic and the sum of the four other components; therefore the five components add up to the complete planetary vorticity diagnostic by construction.

3.3.5 Contour integration on a C-grid

Calculating the curl on a C-grid is consistent with Stokes' law applied to an F cell, and integrating $\nabla \times \mathbf{M} \cdot \hat{\mathbf{k}}$ over several adjacent F cells is equivalent to a line integral of $\mathbf{M}$ around them (see Figure 3.3). As the streamfunction, ψ, is defined on F points we can approximate that the area enclosed by a streamline is a collection of interior F cells and that the area integral of vorticity diagnostics is the line integral of model accelerations around them. This is an approximation as we are assuming

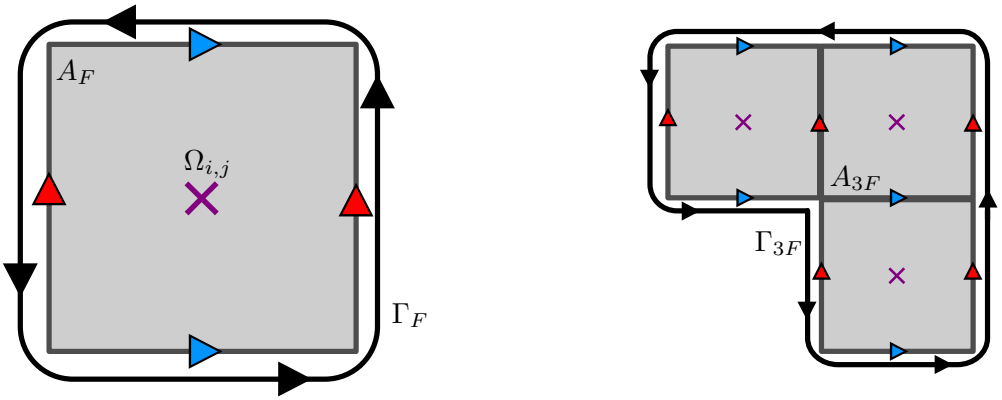

$$\Omega_{i,j} = \frac{1}{A_F} \iint_{A_F} \nabla \times \mathbf{M} \cdot \hat{\mathbf{k}}\, dA \qquad I_{3F} = \iint_{A_{3F}} \nabla \times \mathbf{M} \cdot \hat{\mathbf{k}}\, dA$$
$$\Omega_{i,j} = \frac{1}{A_F} \oint_{\Gamma_F} \mathbf{M} \cdot \mathbf{dl} \qquad I_{3F} = \oint_{\Gamma_{3F}} \mathbf{M} \cdot \mathbf{dl}$$

Figure 3.3: The application of Stokes' theorem on a C-grid. The vorticity diagnostic Ω is equivalent to the normalized line integral of $\mathbf{M}$ around a single F cell of area A_F. The area integral of Ω over a collection of F cells (e.g. A_{3F}) is equivalent to the line integral of $\mathbf{M}$ along the perimeter (e.g. Γ_{3F}).

that the streamline follows the rectangular edges of the interior F cells but the resultant error is minimised if we first interpolate the points onto a sufficiently fine grid. The asymptotic value the contour integral tends towards as the interpolation resolution is increased should be free of area error. This method is applied to all contour integrals presented in Sections 3.4 and 3.5. Any non-topographic contributions to the contour integral that remains after the interpolation will be described as a numerical beta effect.

A numerical beta effect can emerge from $-\nabla_h \cdot (f\mathbf{U})\ |_{i,j}$ even after being interpolated onto a fine grid as the divergence is calculated over the four T cells that surround the central F point (see Equation 3.7). When the internal F points are summed within the contour, the local domains for calculating the grid point divergences will overlap meaning the resultant area integral will not satisfy the divergence theorem in general. Overlapping local domains are a requirement of the C-grid's horizontal geometry. In Section 3.6.3 we highlight how the divergence calculation on a B-grid only requires information from a single tracer cell. The local domains for calculating the divergence do not overlap when integrating on the B-grid and the associated numerical beta effect will not emerge.

3.4 A double gyre model

3.4.1 Details of the configuration

The first experiment in this chapter is an idealized double gyre configuration based on the GYRE PISCES reference configuration in NEMO. The GYRE PISCES reference configuration has been used for a wide range of experiments (Lévy et al., 2010; Lévy et al., 2015; Perezhogin, 2019; Ruggiero et al., 2015). The domain is a closed rectangular basin which is 3180 km long, 2120 km wide, and is rotated at an angle of 45° relative to the zonal direction. The basin exists on a beta plane where f varies linearly around its value at $\sim$ 30°N.

The model has a regular 122×82 grid that is aligned with the rotated basin. The horizontal resolution is equivalent to a 1/4° grid at the equator and the configuration has 31 model levels. Two forms of bathymetry are used in this section. The FLAT configuration has a fixed depth of 4.5km and no partial cells are used. The SLOPED configuration has a linear slope that extends from the North West side of the basin and spans half the basin (see Figure 3.4a). The maximum depth of the SLOPED configuration is 4.5km, the minimum depth is 2km, and partial cells are used to represent the slope.

The circulation is forced by sinusoidal analytic profiles of surface wind stress and buoyancy forcing. The wind stress is zonal and only varies with latitude so that the curl changes sign at 22°N and 36°N (see Figure 3.4b). The wind stress profile is designed to spin up a subpolar gyre in the north, a subtropical gyre in the south, and a small recirculation also emerges in the bottom corner. The net surface heat flux takes the form of a restoring to a prescribed apparent temperature. Further details about the buoyancy forcing can be found in Lévy et al. (2010). The wind stress and buoyancy forcing varies seasonally in a sinusoidal manner.

The model uses a free slip condition on all boundaries except at the bottom where a linear friction drag is applied. A simplified linear equation of state is used, $\rho = \rho_0 \left(1 - a_0 T + b_0 S\right)$, with a thermal expansion coefficient of $a_0 = 2 \times 10^{-4}$kg m^{-3} K^{-1}, a haline coefficient of $b_0 = 7.7 \times 10^{-4}$kg m^{-3} psu^{-1}, and a reference

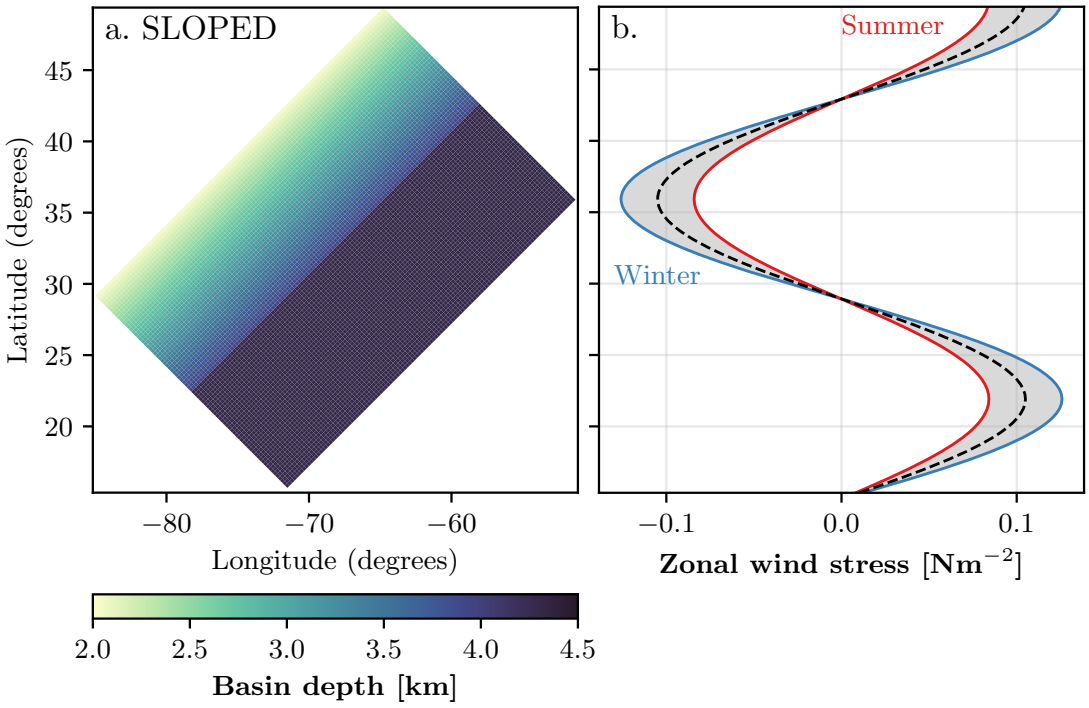

Figure 3.4: (a) Bathymetry of the SLOPED configuration. (b) The wind stress profile for both the FLAT and SLOPED configuration. The wind stress profile varies seasonally in a sinusoidal manner between summer and winter extremes that are highlighted.

density of $\rho_0 = 1026.0$ kg m^{-3}. Horizontal and biharmonic diffusion of momentum is implemented with a diffusivity of 5×10^{10} m^{4}s^{-1}. Biharmonic diffusion of tracers along isopycnals is implemented with a diffusivity of 10^9 m^{4}s^{-1} (Lemarié et al., 2012a; Madec et al., 2019).

The model is spun up for 60 years and the experiment was run for an additional 10 years with monthly-mean outputs. A steady state is not required for the diagnostics to be valid as the time derivative term is present in the vorticity budget. A time step of 10 minutes is used for the model integration.

The EEN vorticity scheme is used for consistency with all analysis discussed in Section 3.3 and the results from the Weddell Gyre in Section 3.5. The EEN method calculates F cell thicknesses using the method described by Equation 3.13 and we therefore expect sudden changes in the F cell thickness near the domain edge for both the FLAT and SLOPED configurations.

3.4.2 Methods

Momentum diagnostics are calculated for every time step and the discrete vorticity diagnostics are calculated by depth-integrating the momentum diagnostics and taking the curl. The resultant diagnostics are time-averaged over the ten year experimental period. The extensive time-averaging will influence the advection vorticity diagnostic as there is an added contribution from the eddy vorticity flux.

For contour integration, the vorticity diagnostics and depth-integrated stream function are then linearly interpolated onto a regular 1/12° grid. This is to minimise errors caused by the difference between the true enclosed streamline area and the total area of the enclosed F cells. Interpolation beyond 1/12° resolution makes little difference to the results, suggesting that the area error has been significantly reduced.

For 1001 values of ψ, closed streamline contours are identified using a marching squares algorithm from the scikit-image package (Van Der Walt et al., 2014). Streamlines that are near the recirculation gyre (south of 20°N) are ignored in this experiment and for some values of ψ no closed streamlines could be found. For each closed streamline found, the vorticity diagnostics are integrated over the area enclosed; this is equivalent to calculating $I(\psi)$ in Equation 3.4 over many values of ψ. The freshwater fluxes mean that $\nabla_h \cdot \mathbf{U} \neq 0$ even in a steady state and an exact stream function cannot be calculated. To test how closely the calculated streamlines follow the circulation we integrate the positive quantity $\mid f_0 \left(\nabla_h \cdot \mathbf{U}\right) \mid$ over the same enclosed areas to estimate the magnitude of the error caused by the divergent flow. The maximum value of f is used as f_0 and the largest contour integral of $\mid f_0 \left(\nabla_h \cdot \mathbf{U}\right) \mid$ is 1.84 $\mathrm{m}^3\ \mathrm{s}^{-2}$ which is substantially smaller than the leading contour integrals presented in the next sub-section. In addition to this test we used an elliptical solver to calculate the Helmholtz decomposition of the depth-integrated velocity field (e.g. Marshall and Pillar, 2011); using the streamlines from the incompressible component does not change the results presented in the next sub-section.

Multiple closed contours can be found for the same value of ψ so an additional contour constraint is needed to ensure $I(\psi)$ is single-valued. In this experiment we

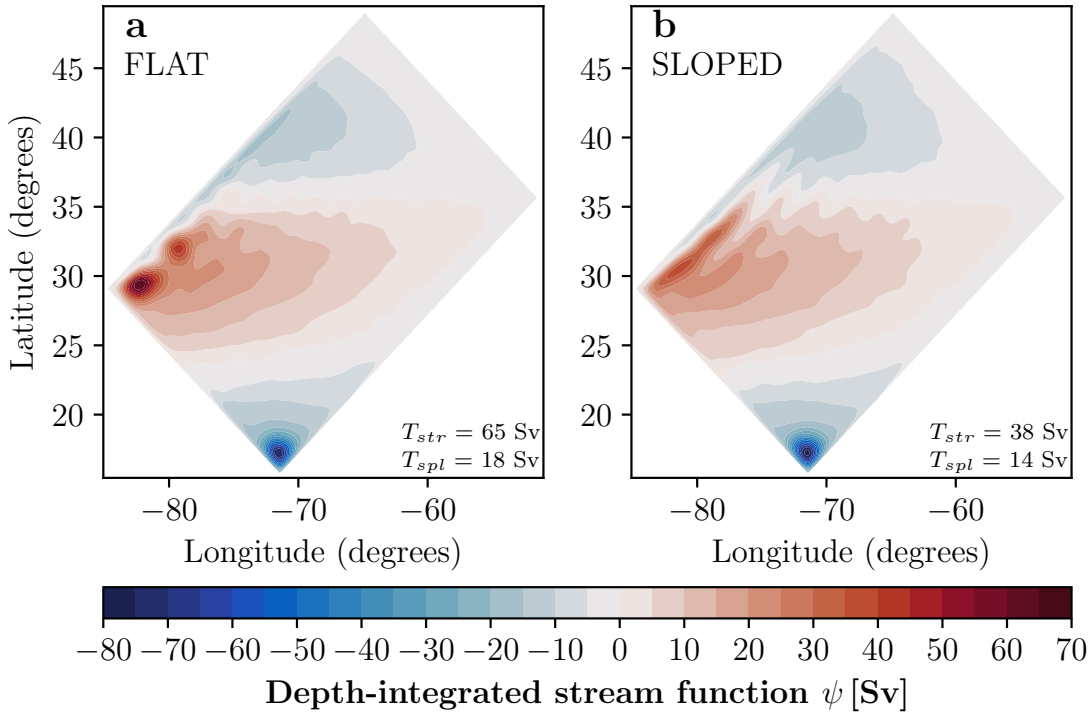

Figure 3.5: The depth-integrated streamfunction (time-averaged) of the (a) FLAT and (b) SLOPED configurations. The transports of the subtropical gyre (T_{str}) and subpolar gyre (T_{spl}) are given.

always choose the contour that spans the largest area which minimises the influence of small pocket circulations that are not a part of the gyre. Closed streamlines that run along the edge of the domain can be hard to identify so a discontinuity in $I(\psi)$ near $\psi = 0$ is expected as the largest detected contours will suddenly become pocket circulations as ψ approaches zero.

3.4.3 Results

The depth-integrated streamfunction from the FLAT and SLOPED configurations is shown in Figure 3.5. The vorticity of the depth-integrated velocity field is shown in Figure 3.6. In both configurations a subtropical and subpolar gyre can clearly be identified and a small recirculation gyre can be found in the Southernmost corner. The subtropical gyre circulation is clockwise and the subpolar gyre circulation is anticlockwise.

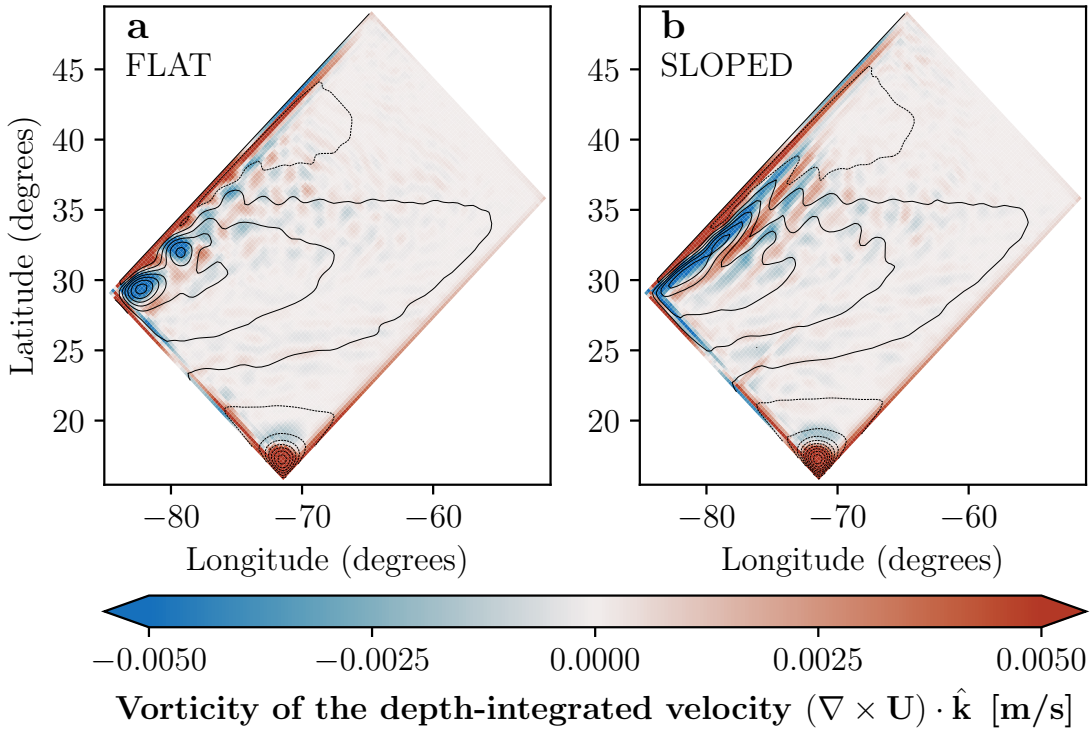

Figure 3.6: The vorticity of the depth-integrated velocity field (time-averaged) for the (a) FLAT and (b) SLOPED configurations. The black contours are streamlines from Figure 3.5.

In the FLAT configuration, the subtropical gyre has a transport of 65 Sv and the subpolar gyre has a transport of 18 Sv. In the SLOPED configuration, the subtropical gyre has a transport of 38 Sv and the subpolar gyre has a transport of 14 Sv. We note that the sloped bathymetry significantly alters the form of the subtropical gyre streamlines.

The depth-integrated vorticity diagnostics of the FLAT and SLOPED configuration are shown in Figures 3.7 and 3.8 respectively alongside the decomposition of the planetary vorticity diagnostic introduced in Section 3.3.4. In the FLAT configuration, we note that the non-linear advection of vorticity and the planetary vorticity diagnostic have the largest grid point values ($\sim 10^{-9}\,\mathrm{m\,s^{-2}}$) near the western boundary currents of both gyres. The wind stress curl is one order of magnitude smaller ($\sim 10^{-10}\,\mathrm{m\,s^{-2}}$) but changes sign less frequently within the gyre regions. We see that the planetary vorticity diagnostic is almost entirely a result of the beta effect (Figure 3.7g and h). We note that the contribution

from varying cell thicknesses in the FLAT configuration is non-zero and localized to the edge (Figure 3.7j) where the EEN Coriolis scheme artificially shrinks F cell thicknesses near masked points.

In the SLOPED configuration (Figure 3.8) the advection and planetary vorticity diagnostics are still large but have an elongated structure similar to the SLOPED streamlines in Figure 3.5b. The bottom pressure torque is significant and is localized to the sloped region (Figure 3.8b). The planetary vorticity diagnostic has a more complex decomposition as the influence of varying cell thicknesses extends beyond the edge of the domain and model level steps also contribute (Figure 3.8k).

The integrals of the vorticity diagnostics over areas enclosed by streamlines are shown in Figure 3.9 and Figure 3.10 for the FLAT and SLOPED configurations respectively as well as the integrals of the planetary vorticity diagnostic components. Example streamline contours are also shown. In these figures $\psi > 0$ describes the subtropical gyre and $\psi < 0$ describes the subpolar gyre. The subtropical and subpolar gyres circulate in the opposite direction but the sign of the integration results are adjusted so that positive integrals correspond to forces that spin the gyres up.

In the FLAT configuration we see that the subtropical and subpolar gyre are entirely driven by wind stress curl. For area integrations that envelop most of the subtropical gyre (small and positive values of ψ), the wind stress curl is largely balanced by the advection of relative vorticity. This balance implies a net import of positive vorticity into the gyre. The imported vorticity cannot originate from the subpolar gyre as the advection of relative vorticity plays no role in spinning the subpolar gyre down. The streamlines at the exterior of the gyre envelop both cells (maxima in ψ) of the subtropical gyre so the advection of vorticity between the cells is not a contribution to the signal. The imported vorticity must originate from the recirculation gyre in the southernmost corner. In the subtropical gyre interior (large positive values of ψ) the wind stress curl is largely balanced by the curl of bottom friction, matching the balance proposed by Niiler (1966).

The planetary vorticity diagnostic is significant in both of the FLAT gyres and is the dominant drag for the subpolar gyre. For area integrals that include

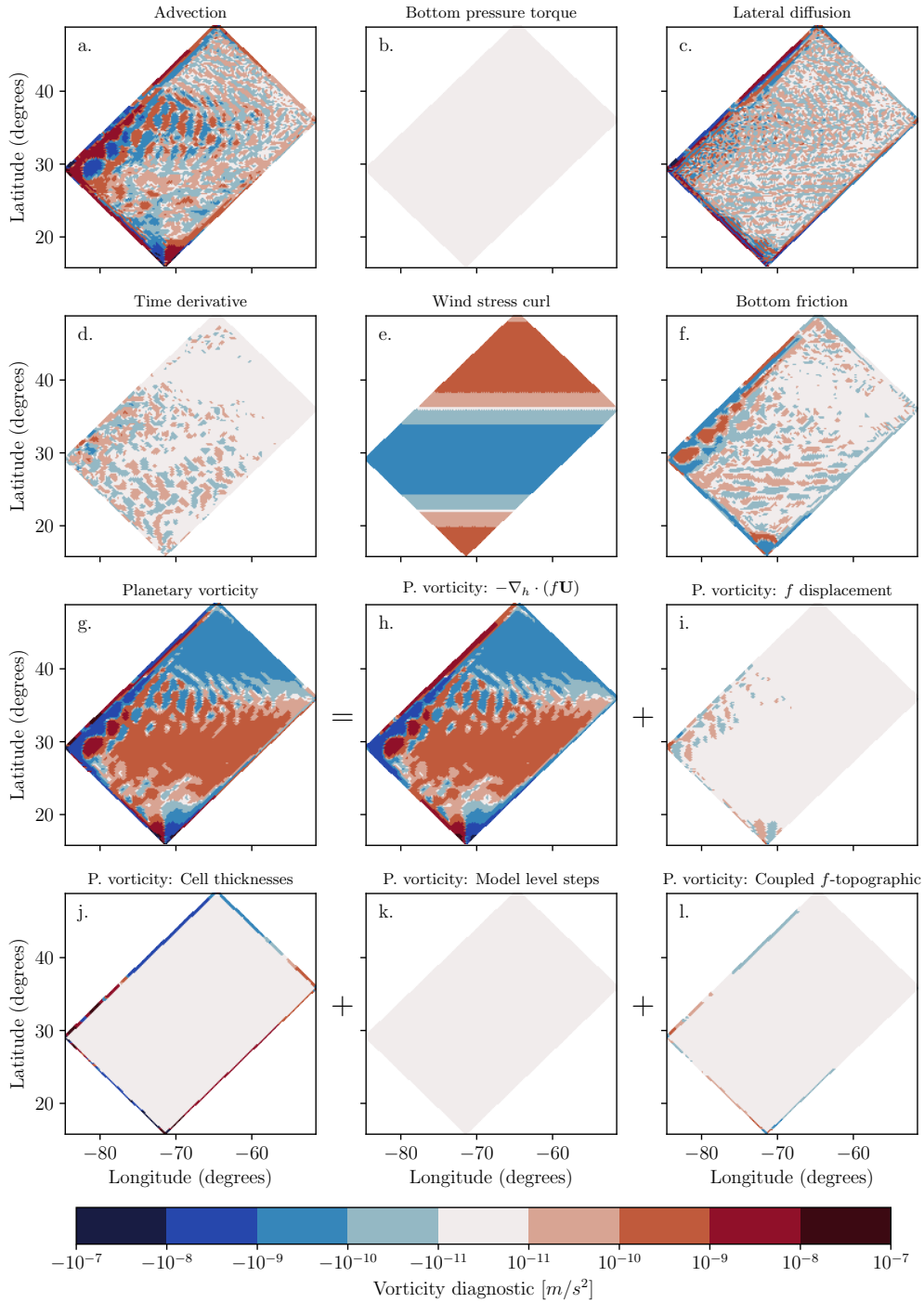

Figure 3.7: The depth-integrated vorticity diagnostics for the FLAT configuration and the components of the planetary vorticity diagnostic (time-averaged). Panels (a) through to (g) are the diagnostics for the terms in the depth-integrated vorticity equation (Equation 3.2). Panels (h) through to (l) are the components of the planetary vorticity diagnostic in Equation 3.23 and discussed in Section 3.3.4. The color bar is logarithmic (for values greater than 10^{-11} in magnitude) and shows the four leading order magnitudes that are positive and negative.

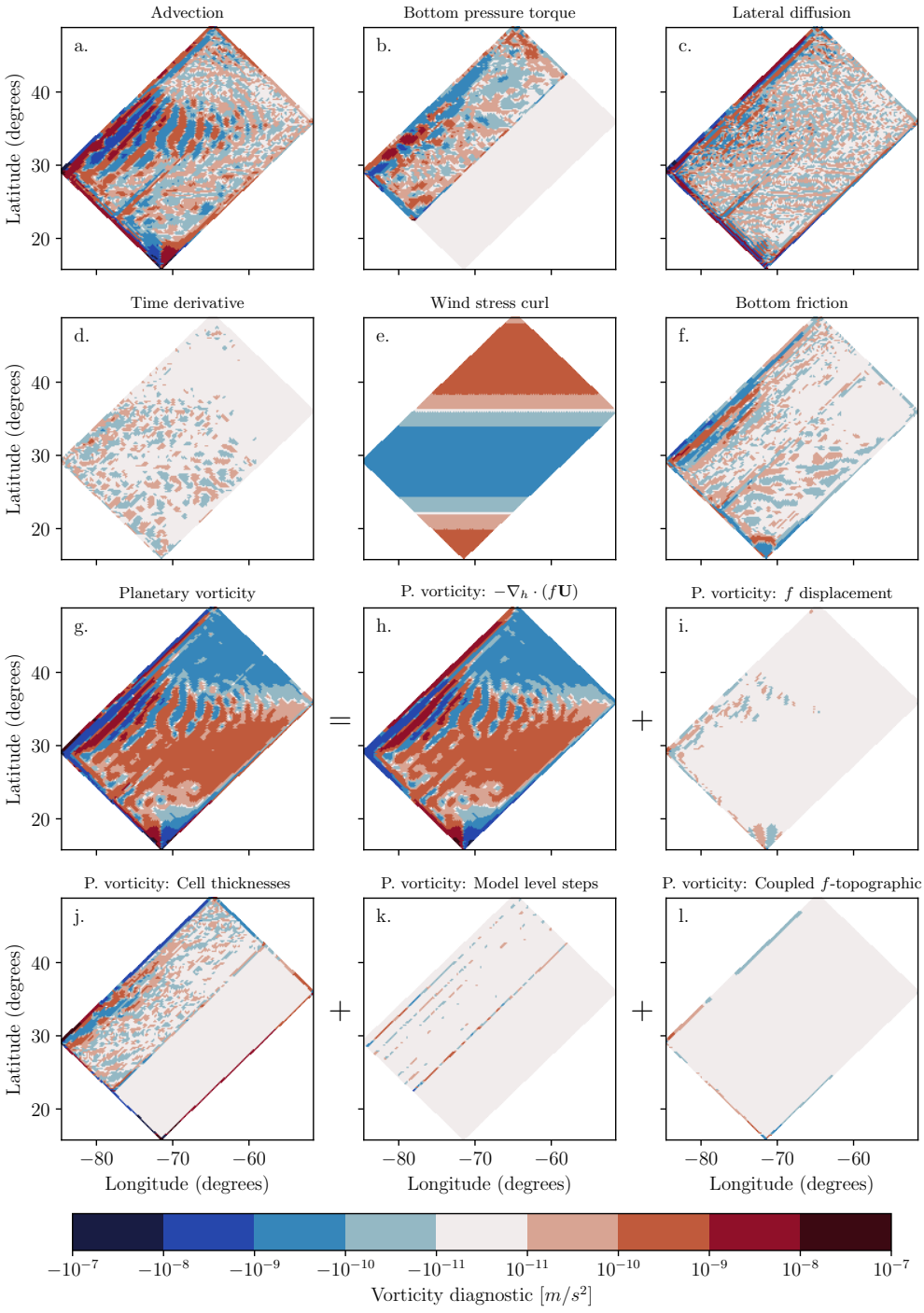

Figure 3.8: The depth-integrated vorticity diagnostics for the SLOPED configuration and the components of the planetary vorticity diagnostic (time-averaged).

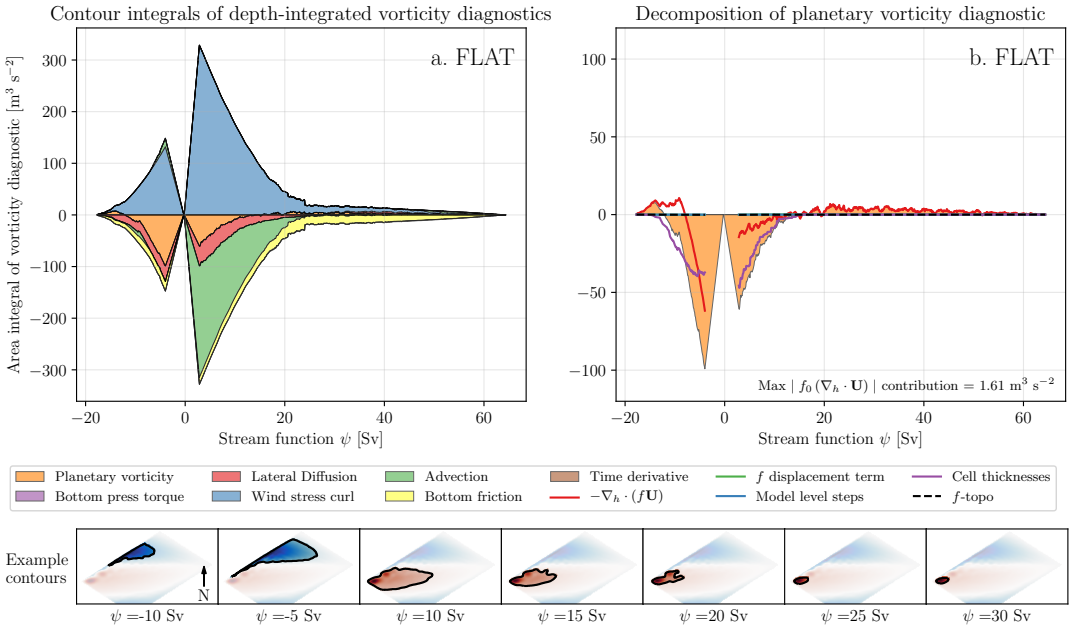

Figure 3.9: Stacked area plots showing the integrals of depth-integrated vorticity diagnostics (time-averaged) for the FLAT configuration. Positive values correspond to a force that spins the subtropical ($\psi > 0$) or subpolar ($\psi < 0$) gyre up. The diagnostics are integrated over areas enclosed by streamlines to develop a full forcing profile of the gyres. The x axis describes the value of the streamline used in the integration. Example streamline contours are given. (b) Shows the area integrals of the planetary vorticity diagnostic and its components. The maximum contour integral of $|f_0\,(\nabla_h \cdot \mathbf{U})\,|$ is stated as an approximate error caused by the divergence of the depth-integrated flow.

the exterior of either gyre (small values of ψ), the integrated planetary vorticity diagnostic is a combination of a numerical beta effect originating from the discrete calculation of $-\nabla_h \cdot (f\mathbf{U})$ and the influence of partial F cells that are artificially created by the EEN scheme. At the interior of both gyres (large values of ψ) the numerical beta effect is the only component.

In the SLOPED configuration we see that both the subtropical and subpolar gyre are almost entirely driven by wind stress curl. There is no dominant force spinning the gyres down. Advection, bottom pressure torques, lateral diffusion, bottom friction, and planetary vorticity all make a similar contribution to spinning the gyres down. The planetary vorticity diagnostic is similarly mixed as both the numerical beta effect and partial cells make up the signal. The gyres in the SLOPED configuration appear to be an intermediate case between a topographically steered

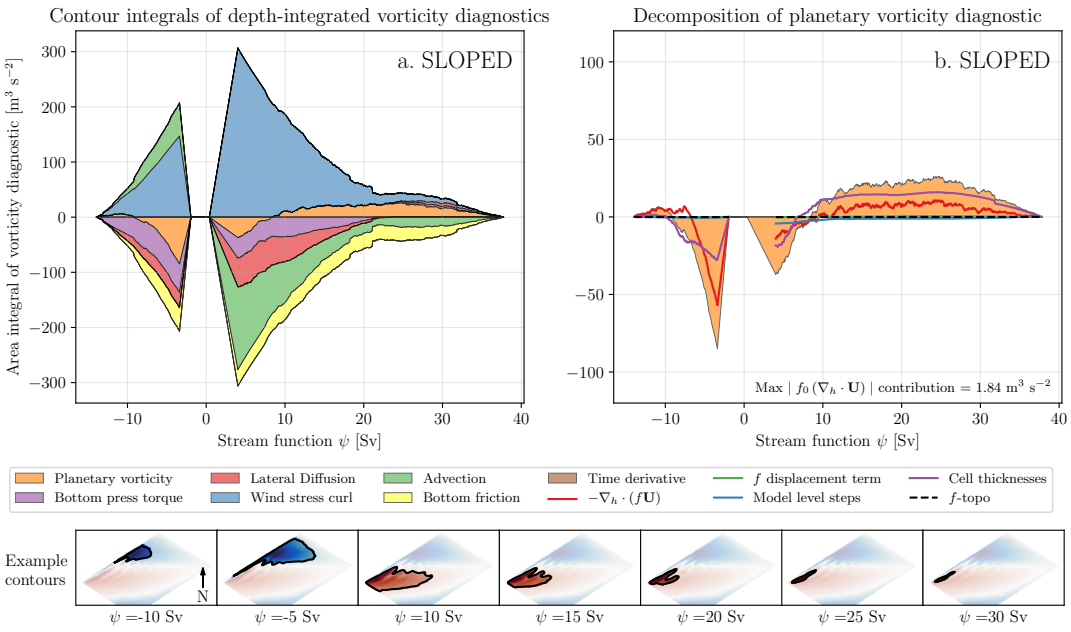

Figure 3.10: Stacked area plots showing the integrals of depth-integrated vorticity diagnostics (time-averaged) for the SLOPED configuration. Positive values correspond to a force that spins the subtropical ($\psi > 0$) or subpolar ($\psi < 0$) gyre up. (b) Shows the area integrals of the planetary vorticity diagnostic and its components.

gyre and an advective regime.

Spurious forces that emerge from the discrete Coriolis acceleration are significant in idealised models with and without variable bathymetry and appear to have a large influence on gyre circulations. In the next sub-section we see if these forces are also significant in a realistic global model.

3.5 The Weddell Gyre

3.5.1 Details of the configuration

We now consider a more realistic configuration based on the NEMO global model with realistic forcing and bathymetry. In this experiment, we use an ocean-ice global configuration that is similar to that described in Storkey et al. (2018) but based on NEMO version 4. The global grid is based on the 'ORCA' family of grids within the NEMO framework (Madec et al., 2019). In this chapter we only consider the configuration using the ORCA025 grid (1/4° horizontal resolution at

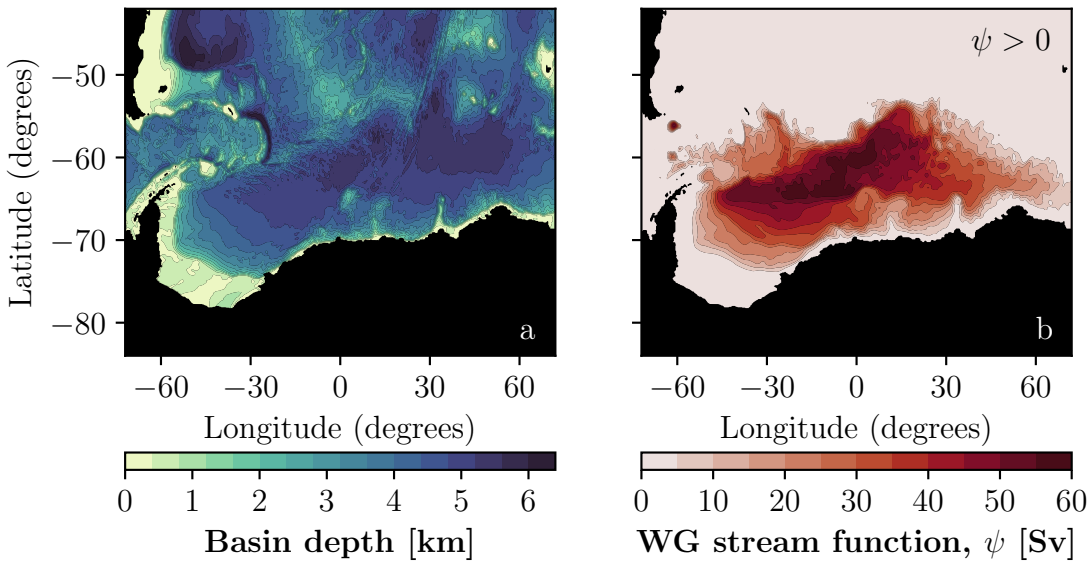

Figure 3.11: (a) The bathymetry of the Weddell Gyre region in the global model. (b) Depth-integrated streamfunction of the Weddell Gyre (time-averaged).

the equator). Most of the model bathymetry for ORCA025 is derived from the ETOPO1 data set (Amante and Eakins, 2009). Bathymetry on the Antarctic shelf is based on IBSCO (Arndt et al., 2013) and has been smoothed by three applications of a first order Shapiro filter. The bathymetry is represented in z-coordinates by partial cells (Barnier et al., 2006). Surface forcing is taken from the CORE2 surface forcing data set (Large and Yeager, 2009) and includes contributions from sea ice. The bathymetry is shown in Figure 3.11a.

The model uses a free slip lateral boundary condition with a quadratic drag along the bottom boundaries and the TEOS-10 equation of state (McDougall and Barker, 2011). Biharmonic diffusion of momentum is implemented and acts along model level surfaces with a diffusivity that varies with local horizontal grid spacing (Willebrand et al., 2001). Laplacian diffusion of tracers is implemented and acts along isopycnal surfaces with a diffusivity that also varies with local horizontal grid spacing. The EEN vorticity scheme is used again for consistency with the analysis in Section 3.3 and the results in Section 3.4.

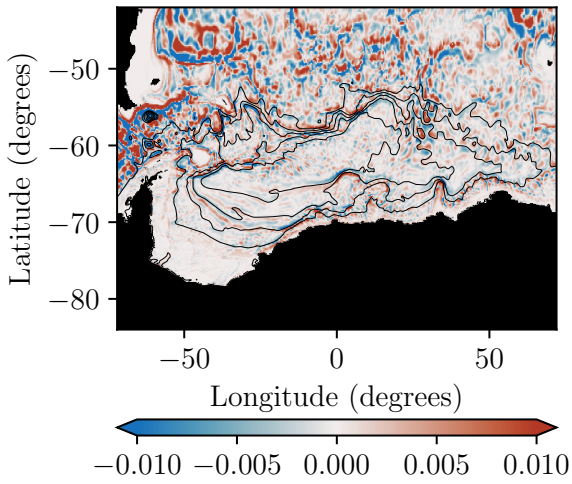

Figure 3.12: The vorticity of the depth-integrated velocity field (time-averaged) in the Weddell Gyre region of the global model. The black contours are positive streamlines ($\psi > 0$) from Figure 3.11.

3.5.2 Methods

The methods used for calculating the depth-integrated streamfunction, vorticity diagnostics, and contour integrals are identical to those described in Section 3.4.2. We study the area including and surrounding the Weddell Gyre in the model (see Figure 3.11) and consider the time-averaged fields over a typical year, specifically 1977. The stream function is interpolated onto a regular 1/12° grid and closed contours are identified for 201 values of ψ. Interpolating beyond 1/12° resolution makes little difference to the results, suggesting that any area errors have been significantly suppressed. We test how closely the calculated streamlines follow the circulation by integrating the positive quantity $\mid f_0 \, (\nabla_h \cdot \mathbf{U}) \mid$ over the same enclosed areas to estimate the magnitude of the error caused by the divergent flow. The maximum value of $\mid f \mid$ is used as f_0 and the largest contour integral of $\mid f_0 \, (\nabla_h \cdot \mathbf{U}) \mid$ is 19.52 $\mathrm{m}^3\ \mathrm{s}^{-2}$ which is substantially smaller than the leading contour integrals presented in the next sub-section. In addition to this test we used an elliptical solver to calculate the Helmholtz decomposition of the depth-integrated velocity field; using the streamlines from the incompressible component does not change the results presented in the next sub-section.

As we are studying a one gyre system we choose to only identify contours where $\psi > 0$. This effectively filters out the vorticity budget of closed circulations in the ACC. The sign of the integration results are adjusted so that positive integrals correspond to forces that spin the Weddell Gyre up.

3.5.3 Results

The depth-integrated streamfunction of the Weddell Gyre is shown in Figure 3.11b and it can be seen that the Weddell Gyre has a transport of 60 Sv. The streamlines follow the isobaths closely suggesting the circulation is largely constrained by the bathymetry. The vorticity of the depth-integrated velocity field is shown in Figure 3.12.

The depth-integrated vorticity diagnostics are shown in Figure 3.13. The fields shown in Figure 3.13 have been smoothed using 25 point nearest neighbour averaging over a local 5×5 grid. The contribution from model level steps (Figure 3.13k) has not been smoothed to show that it is localized to specific lines where the number of model levels change. The combined effect of the wind stress and stress due to sea ice are shown in Figure 3.13e. With realistic topography and forcing, the grid point values of depth-integrated vorticity diagnostics are very noisy (even when smoothed) with the exception of the surface stress curl. This highlights how important it is to integrate the vorticity diagnostics when interpreting them. For individual grid points we see that the planetary vorticity diagnostic is made up of contributions from the beta effect, partial cells, and a significant contribution from model level steps. The beta effect is the most coherent of the contributions and is mostly negative in the western limb of the gyre where $V > 0$ and positive in the eastern limb where $V < 0$. As expected, the contribution from model levels steps is localized to areas where the number of model levels change.

Unlike in the double gyre model, bottom friction appears to be small and incoherent in the Weddell Gyre region and is unlikely to have any significant influence on the vorticity budget. The total time tendency (Figure 3.13d) is non-zero in

this vorticity budget suggesting that the model is not in a completely steady state; however, the grid point values are only significant in the Drake Passage and are noisy.

The integrals of the depth-integrated vorticity diagnostics over areas enclosed by streamlines are shown in Figure 3.14 alongside integrations of the planetary vorticity components. The largest identified streamline for the gyre has a value of 8 Sv. This causes a discontinuity in Figure 3.14 and integrated terms for stream function values less than 8 Sv describe the dynamics of remote pocket circulations and are not relevant to the Weddell Gyre. We see that the Weddell Gyre is almost entirely spun up by the wind stress curl. The stress due to sea ice (marked by hatching in Figure 3.14a) and the advection of relative vorticity also help to spin the Weddell Gyre up. The advective contribution is caused by vorticity exchange at the interface between the Weddell Gyre and the ACC.

Bottom pressure torques and lateral diffusion play a notable role in spinning the Weddell Gyre down but the planetary vorticity diagnostic is the most significant contribution. Looking at the decomposition of the planetary vorticity diagnostic we see that the signal is mostly determined by changes in model level and the remainder is determined by variations in cell thickness. This suggests that the Weddell Gyre is almost entirely spun down by topography due to the combined effect of bottom pressure torques and the planetary vorticity diagnostic, but the majority of the gyre's interaction with the sea floor is spurious. This conclusion is true in both the interior and exterior of the gyre.

The results in Figure 3.14 are concerning as they suggest that the vorticity input from the realistic surface stresses is largely balanced by spurious topographic accelerations. In an area of the ocean with such strong bathymetric feratures, it is not surprising that topographic forcing is important but we would expect the topographic accelerations from a realistic bathymetry to also be realistic. Instead, the dominant component of the topographic forcing is a spurious acceleration that is localized to discrete lines where the number of model levels change (see Figure 3.13k) and arises from the masking of the non-topographic Coriolis acceleration.

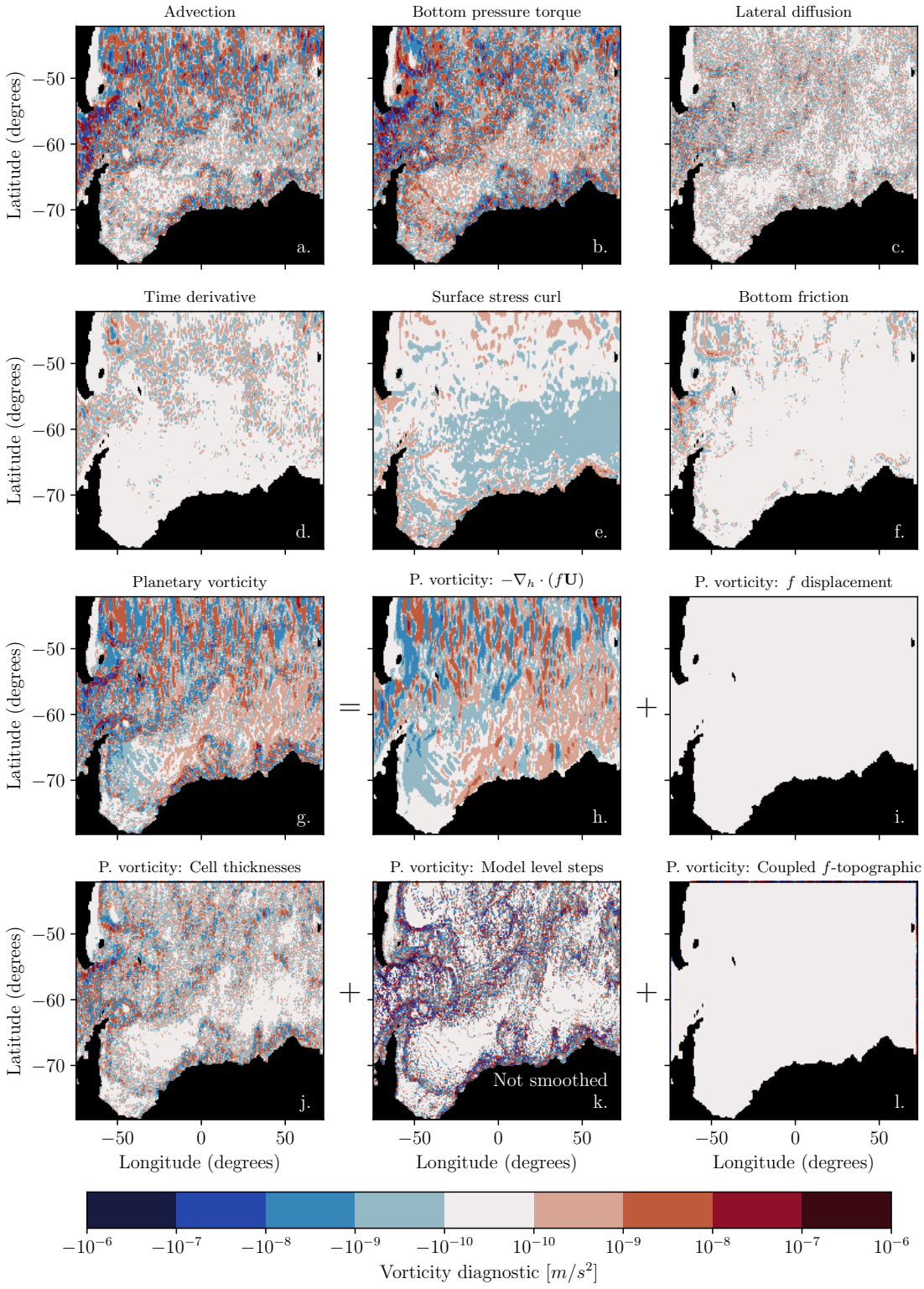

Figure 3.13: The depth-integrated vorticity diagnostics for the Weddell Gyre and the components of the planetary vorticity diagnostic (time-averaged). All fields except (k) have gone through a 25 point nearest neighbour smoothing process.

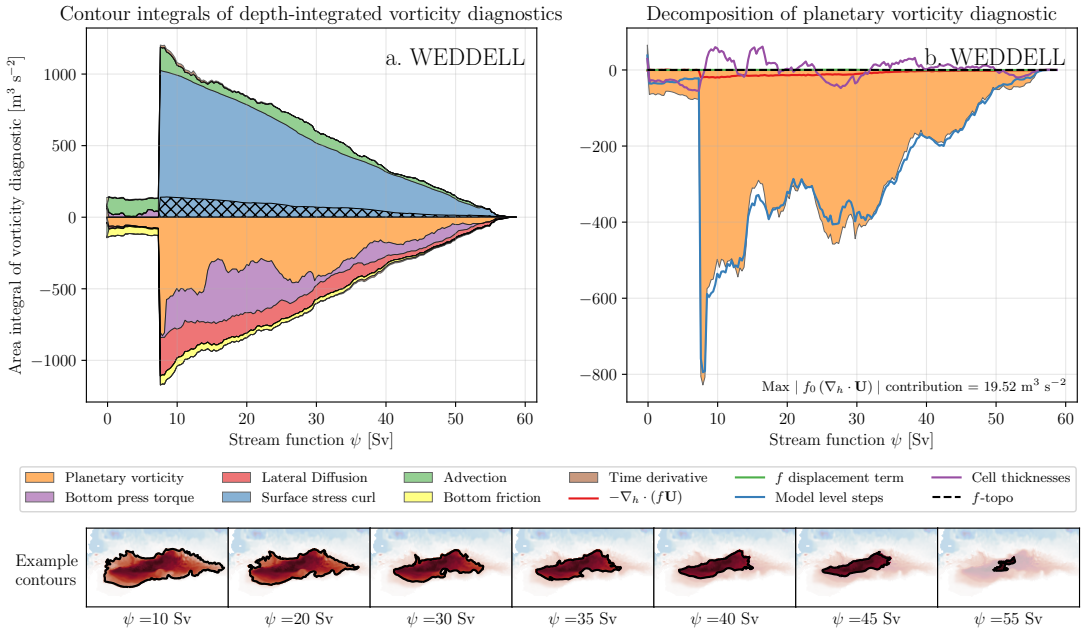

Figure 3.14: Stacked area plots showing the integrals of depth-integrated vorticity diagnostics for the Weddell Gyre (time-averaged). Positive values correspond to a force that spins the gyre up. The hatching marks the sea ice contribution to the surface stress integral. The largest identified streamline for the gyre has a value of 8 Sv. This causes a discontinuity in Figure 3.14 and integrated terms for stream function values less than 8 Sv describe the dynamics of remote pocket circulations and are not relevant to the Weddell Gyre. (b) Shows the area integrals of the planetary vorticity diagnostic and its components.

This suggests that the partial cell representation of the sea floor is not providing realistic topographic forcing in the Weddell Gyre region.

3.6 Discussion

We have shown that the vorticity dynamics of both highly idealized and realistic gyre configurations are greatly influenced by spurious forces that emerge from the discrete Coriolis force and the step-like representation of bathymetry. In the idealized double gyre configuration (Section 3.4) the spurious force is a combination of numerical beta and topographic effects that are present in both the FLAT and SLOPED configuration. In the realistic Weddell Gyre (Section 3.5) the spurious force is the dominant drag and is entirely determined by model level steps and partial cells. In this section we discuss possible methods to mitigate these spurious forces.

3.6.1 Alternative vorticity schemes

The results presented in Sections 3.4 and 3.5 both use the EEN vorticity scheme and it is tempting to dismiss the spurious forces as an artifact of the selected scheme. The analysis in Section 3.3.2 is general for three popular schemes: EEN, ENE, and ENS. The methods and decomposition used in this chapter are applicable under any scheme where the Coriolis acceleration can be expressed in the form of Equations 3.8 and 3.9. Results from the SLOPED double gyre configuration using the different schemes are presented in Appendix A.3 and the vorticity budgets are qualitatively similar. Spurious topographic forces and the numerical beta effect are still significant.

It therefore seems that switching between the available vorticity schemes will not alleviate the spurious signal. It is possible that a new scheme could be formulated which is designed to significantly reduce the spurious forces, but that will most likely require abandoning the conserved quantities that characterise the existing schemes.

3.6.2 Alternative depth-integrated vorticity equations

In Section 3.2.1 we derived a depth-integrated vorticity equation by taking the curl of the depth-integrated momentum equation and we calculated the model vorticity diagnostics using the equivalent discrete method. As discussed in Section 3.2.1, there are alternative formulations of the depth-integrated vorticity equations with different physical meanings. An accurate model should be able to represent all forms of the depth-integrated vorticity budget so switching between formulations does not alleviate any spurious forces, but it is interesting to see if any of the spurious contributions in this chapter can spill over into other vorticity budgets.

If we derive a continuous depth-integrated vorticity equation by depth-integrating the curl of the momentum equations then the Coriolis acceleration emerges in the vorticity budget as:

$$\int_{-H(x,y)}^{\eta(x,y,t)} \left[\nabla \times \left(-f\hat{\mathbf{k}} \times \mathbf{u}\right)_h\right] \cdot \hat{\mathbf{k}}\, dz = -\nabla_h \cdot (f\mathbf{U}) + f\left(\mathbf{u}_b \cdot \nabla\right) H + f\left(\mathbf{u}_t \cdot \nabla\right) \eta, \quad (3.24)$$

where $\mathbf{u}_t$ and $\mathbf{u}_b$ are the horizontal velocities at the free surface and sea floor respectively. When compared with Equation 3.2 we can see that the planetary vorticity term has an additional topographic and free surface term. The second term on the right hand side of Equation 3.24 describes a vortex stretching acting on the vertical velocity induced by the bottom topography. In configurations with no variable bathymetry and small variations in the free surface, the order of taking the curl and depth-integrating no longer affects the vorticity budget so the non-topographic spurious forces identified in this chapter will remain in either formulation.

To calculate the discrete curl of a horizontal vector field near the bathymetry we need to make an assumption about how the along-slope component varies as it approaches the edge of the domain. We can assume either a free slip or no slip boundary condition by using a ghost point that mirrors the location of the closest grid point into the bathymetry. For a free slip boundary condition the ghost point value matches the closest grid point value, $F^{\parallel}$; for a no slip boundary condition the ghost point value will be the negative of the closest grid point value, $-F^{\parallel}$. A partial slip boundary condition also exists where the value of the ghost point will be between $-F^{\parallel}$ and $F^{\parallel}$.

Let us return to the simple flow introduced in Section 3.3.3 and illustrated in Figure 3.2 but this time when we calculate the planetary vorticity diagnostic we will calculate the curl of the Coriolis acceleration on each model level and then depth-integrate. For the lower level, the horizontal flow is entirely in the x direction so there is a zero along-slope component of the Coriolis acceleration near the bathymetry ($F^{\parallel}$=0). This means that if a free slip, no-slip, or partial slip boundary condition are used the ghost point value will be zero and the curl of the Coriolis force (centred on the purple cross in Figure 3.2) will be zero in all three cases. As all vorticity generation takes place in the upper level, the planetary vorticity diagnostic is the same if we take the curl before or after depth-integrating (Equation 3.21) and the effect of model level steps can exist in either vorticity budget.

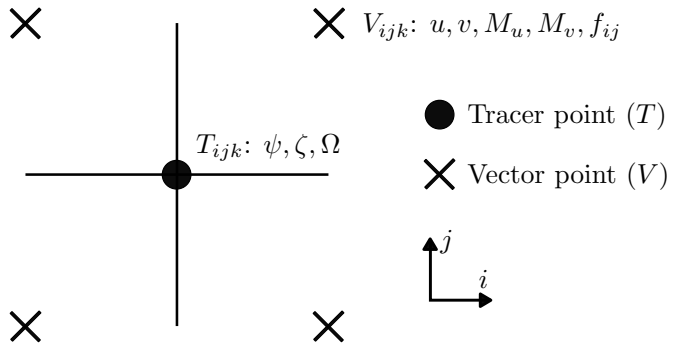

Figure 3.15: The horizontal distribution of variables on the B-grid. Tracer points (T) and vector points (V) are shown alongside important values that are centred on these points. Just like in the C-grid, the vertical velocities are found directly above and below the Tracer point.

The result of Equation 3.21 can be interpreted as a vortex stretching acting on the vertical velocity that is induced by the change in horizontal velocity u_1 (see Figure 3.2). The vertical velocity seems unlikely to originate from topographic upwelling as there is no flow in the y direction. This fact combined with the ambiguity of ∇H at model level steps means we would advise caution before comparing the discrete vortex stretching that originates from model level steps to the analytic vortex stretching in Equation 3.24.

3.6.3 The B-grid

Altering the grid geometry can significantly change the behaviour of model forces. To highlight this we consider how the Coriolis force behaves on the B-grid. The B-grid excels at representing geostrophic flows as u, and v are located on the same vector point. The streamfunction and relative vorticity are located on the tracer point as shown in Figure 3.15.

On the B-grid the Coriolis acceleration is simply:

$$\mathrm{COR}^x_{i,j,k} = f_{i,j}\, v_{i,j,k}, \tag{3.25}$$

$$\mathrm{COR}^y_{i,j,k} = -f_{i,j}\, u_{i,j,k}. \tag{3.26}$$

The Coriolis acceleration does not rely on multi-point averaging or thickness

weighting of f so numerical contributions do not emerge in the grid point acceleration.

On the B-grid u and v lie on the same point so they share the same mask. This means that non-zero Coriolis accelerations are never masked near model level steps and the depth-integrated Coriolis acceleration is a function of the depth-integrated velocities only:

$$\widehat{\mathrm{COR}}^{x}_{i,j} = f_{i,j}\, V_{i,j}, \tag{3.27}$$

$$\widehat{\mathrm{COR}}^{y}_{i,j} = -f_{i,j}\, U_{i,j}, \tag{3.28}$$

We therefore conclude that the spurious force caused by model level steps on the C-grid (see Section 3.3.3) is not present on the B-grid. The corresponding planetary vorticity diagnostic is equal to $-\nabla_h \cdot (f\mathbf{U})\,|_{i,j}$ calculated over a single tracer cell.

Calculating the curl on a B-grid is consistent with Stokes' law applied to a tracer cell but the vector information is found on the corners of the cell. As the stream function is defined on the tracer point we can approximate that the area enclosed by a streamline is a collection of interior tracer cells. Similarly to the C-grid case in Section 3.3.5 this is an approximation as we are assuming that the streamline follows the rectangular edges of the interior tracer cells so interpolation may be required to remove any significant area error. Unlike the C-grid case, the planetary vorticity diagnostic is equal to $-\nabla_h \cdot (f\mathbf{U})\,|_{i,j}$ calculated over a single tracer cell. Therefore, the area integral of the planetary vorticity diagnostic will satisfy the divergence theorem applied to the internal tracer cells. It seems likely that this discrete integral may vanish on a sufficiently fine grid but further investigation with idealized and realistic streamlines is needed.

Using the B-grid would remove all of the spurious topographic forces identified in this chapter. This highlights how a model circulation's interaction with the sea floor is significantly affected by the grid geometry. Adopting the B-grid would mean missing out on some of the C-grid's advantages. This includes the intuitive centred difference definitions of divergent and rotational terms. Also, Arakawa and Lamb

(1977) found that the C-grid was superior in simulating gravity wave frequencies while the the B-grid is better at representing inertial wave frequencies.

3.6.4 Terrain-following coordinates

The spurious topographic effects found in this chapter are a consequence of how bottom topography is represented in z-coordinates. In the Weddell Gyre especially we see how model level steps can create large spurious contributions to the depth-integrated vorticity budget.

Terrain-following coordinates (or σ-coordinates) are an alternative form of vertical coordinate where the vertical resolution adjusts with the bottom topography so that the same number of model levels are present in all fluid columns (Song and Haidvogel, 1994). σ-coordinates are used in Stewart et al. (2021), Schoonover et al. (2016), and Jackson et al. (2006) and have the advantage of removing spurious terms that emerge from model level steps. The forms of the EEN, ENE, and ENS vorticity schemes are unchanged when using terrain-following coordinates so the horizontal variations in cell thicknesses could still cause a spurious signal.

Terrain-following coordinates are not used widely in climate models because of the difficulty in calculating accurate horizontal pressure gradients (near the equator), advection, and isoneutral tracer diffusion. A full discussion of the current advantages and limitations of terrain following coordinates can be found in Lemarié et al. (2012b).

3.6.5 Isopycnal coordinates and the vertical Lagrangian-remap method

In isopycnal C-grid models, where density is used as a vertical coordinate, cell thicknesses still vary and in models with many density layers the model levels are free to incrop to the sea floor. The forms of the EEN, ENS, and ENE schemes are unchanged when using density coordinates so the spurious signals in the planetary vorticity diagnostic seem to be possible. In configurations where density layers infrequently incrop to the sea floor, the effect of model level steps

will be significantly suppressed as the grid is approaching the limit of a terrain-following coordinate system.

In C-grid models that use the vertical Lagrangian-remap method (Adcroft et al., 2019; Bleck, 2002) the vertical coordinate evolves with the flow and is then conservatively remapped onto a target grid (see Griffies et al. (2020) for a review). The forms of the EEN, ENS, and ENE schemes are unchanged when using this method. If the target coordinate grid still has horizontal variations in cell thicknesses and incrops with the sea floor, we would expect there to be spurious topographic interactions with the sea floor. It is possible that in areas of topographic upwelling the effect of model level steps could be reduced as Coriolis accelerations near the bathymetry are elevated by the vertical motion and are partially projected onto unmasked points when remapped onto the target grid.

3.7 Summary

The depth-integrated vorticity budget is a valuable tool for identifying important model forces in gyre circulations. Vorticity diagnostics can be integrated over the area enclosed by streamlines to identify forces responsible for spinning the gyre up and down. By considering how the vorticity budget is represented on a C-grid with step-like bathymetry we identified spurious forces that emerge from the representation of bottom topography and the discrete Coriolis acceleration. Model level steps and partial cells produce two distinct spurious topographic forces. In the absence of bottom topography, it is shown that the discrete planetary vorticity term does not generally vanish when integrated over the discrete area enclosed by a streamline. This suggests that a spurious non-topographic force, described as a numerical beta effect, is also present.

We first studied the vorticity budget of an idealized double gyre configuration with analytic geometry, forcing, and two bathymetry options. The FLAT variant has a constant depth and the SLOPED variant has a linear slope that extends over half the domain. The subtropical gyre of the FLAT configuration is non-linear at the exterior (wind stress curl balanced by advection) and is in a Stommel (1948)

regime in the interior (wind stress curl balanced by friction). The FLAT subpolar gyre is spun up by wind stress curl and mostly spun down by spurious forces found in the planetary vorticity diagnostic. Spurious forces are significant in both FLAT gyres and are a consequence of the numerical beta effect and partial F cells that are artificially introduced by the EEN vorticity scheme. Artificial partial F cells would not be present in the ENS or ENE vorticity schemes.

The vorticity budget of the SLOPED gyres features bottom pressure torques and an increased influence of partial cells on the planetary vorticity diagnostic. The SLOPED subtropical gyre is an intermediate case between a topographically steered gyre and a non-linear circulation. The SLOPED subpolar gyre is driven by wind stress curl but spun down by the combined effect of bottom pressure torques and spurious interactions with the topography via partial cells. This first case study highlighted how spurious terms can dominate a vorticity budget in idealized configurations with and without variable bathymetry.

The second case study was the Weddell Gyre in a global model where the forcing and geometry are more realistic. By studying the vorticity budget of the Weddell Gyre we conclude that the model circulation is mostly spun up by wind stress curl and spun down by the combined effect of bottom pressure torques and spurious interactions with the topography. The largest of the topographic forces spinning the Weddell Gyre down is the spurious and unrealistic force caused by model level steps.

Switching to alternative vorticity schemes is not effective at reducing spurious contributions to the vorticity budget. By presenting a general form of the discrete Coriolis acceleration we are able to quickly conclude that the topographic and non-topographic spurious forces will remain under all three vorticity schemes and any other scheme that uses this general form. The influence of model level steps is a direct consequence of the C-grid geometry when using vertical coordinates that intersect the bathymetry and is relatively insensitive to the choice of vorticity scheme.

Altering the geometry of the discretisation is an effective method for reducing spurious topographic forces. The B-grid is better at representing the Coriolis force and it is not possible for model level steps or partial cells to influence the Coriolis

acceleration. Model level steps and their influence on the Coriolis acceleration can be avoided altogether by using terrain-following coordinates. Fortunately, many existing vorticity budget studies have used a form of terrain-following coordinate (e.g. Gula et al., 2015; Jackson et al., 2006; Schoonover et al., 2016; Stewart et al., 2021) and future studies should emphasise the relevance of the vertical discretization to C-grid vorticity budgets. In this chapter, the spurious force was easy to identify as the curl of the depth-integrated Coriolis force is expected to vanish when integrated within closed streamlines. Future studies using alternative integrating methods will need to rely on diagnostics to identify and interpret the spurious force.

The B-grid and terrain-following coordinates have their own unique limitations and it is unclear how much the identified spurious forces corrupt circulation variables such as the gyre transport. It is possible that the spurious forces are inadvertently performing the role of one or more real ocean processes that are required for accurate simulations. If a combination of non-spurious forces can fully account for the spurious forces found in this chapter then the identified problem is purely diagnostic in nature. Otherwise, any part of the spurious forcing that cannot be accounted for by non-spurious forces should be considered as a numerical error. This numerical error could be small but may also accumulate under specific conditions and corrupt model circulations. The spurious cooling (Hecht, 2010) that occurs when a dispersive advection scheme is used with the Gent and McWilliams (1990) eddy parametrization highlights the dangers of ignoring numerical errors.

It is also possible that other model forces contain spurious contributions that have not been uncovered in this chapter. These contributions could be significant and may have the potential to cancel the spurious effects found in this chapter. When looking at the integrated diagnostics in Figures 3.9, 3.10, and 3.14 we see that usually the only model force with an opposite contribution to the Coriolis force that is large enough to cancel the found spurious effects is the surface stress. It seems unlikely that the surface stress contains spurious contributions that are closely tied to bathymetry and the Coriolis parameter. However, problematic vertical diffusion of the surface stress in the ocean interior may be a source of spurious contributions.

It is still unclear which circumstances make the identified spurious forces significant in some cases (such as the Weddell Gyre) and less significant in other cases with bathymetry (such as the SLOPED configuration). Many factors could determine this including: the geometry of the sea floor, the circulation properties, the surface forcing, or the resolution (horizontal and vertical). It is not a certainty that refining horizontal and vertical resolution will resolve the problems found in this chapter. When using a z-coordinate model, there will always be the same surface area of vertical sidewall, no matter what the grid spacing is. Diagnosing simulations where the resolution is varied with a similar circulation above may provide insight into this potential sensitivity.

It is important for the ocean modelling community to continue developing new ways of representing bathymetry and we hope that vorticity budgets and the diagnostic method presented in this chapter will provide a valuable tool for assessing and quantifying representations of the sea floor in current and future ocean models.

3.8 End of chapter remarks

In this chapter, we have found that the vorticity budget of a simulated Weddell Gyre simulation has been corrupted by spurious terms from the C-grid discretization. This is unfortunate for our study of the relevant forces for the Weddell Gyre but has brought to light an important limitation of the C-grid that will affect a wide range of future studies. In Chapter 2, we explored how an idealized Weddell Gyre is sensitive to mesoscale eddies and in this chapter we took a deep dive into the numerics of a realistic model. In the following chapter we take a major step back from the details of the mesoscale and model numerics to take a look at the spatial and temporal patterns of ventilation in the Southern Ocean.

4

Spatial and Temporal Patterns of Southern Ocean Ventilation

Contents

In this chapter we study the results of an extensive backwards-in-time trajectory experiment, the first of its kind in a simulated Southern Ocean. By calculating the thirty year history of each subvolume in the Southern Ocean we can identify spatial and temporal patterns across the entire Southern Ocean and identify the local and remote influence of the Weddell Gyre. The content of this chapter is based on a paper that has been submitted to *Geophysical Research Letters*. Unlike Chapters 2 and 3,

this research project was my original idea which I then developed by reaching out to Graeme MacGilchrist (Princeton University). Just like in the previous chapters I took the lead on this project by developing and implementing the calculation of Lagrangian trajectories, conducting the analysis, and writing the paper.

4.1 Introduction

Ocean ventilation describes how mixed layer properties such as temperature, salinity, and dissolved gas concentrations are translated into the interior ocean. The Southern Ocean is an important area for the ventilation of intermediate and abyssal waters (Gebbie and Huybers, 2010) and is also where much of the deep water formed in the North Atlantic returns to the surface to interact with the atmosphere (Liu and Huang, 2012; Talley, 2013). The ventilation of heat and carbon in the Southern Ocean is expected to influence the limits and timescale of anthropogenic climate change (Bopp et al., 2002; Sallée et al., 2012) and it is therefore important to work out where and when the Southern Ocean ventilates.

Subduction is the transfer of water from the mixed layer into the interior ocean and is often assumed to be a rate-limiting step for Southern Ocean ventilation. Localized subduction 'hotspots' can be identified in Argo data (Sallée et al., 2010; Sallée et al., 2012) and reanalysis (Buongiorno Nardelli et al., 2018). These sites have deep mixed layers in late winter and undoubtedly influence the ventilation of the Southern Ocean. However, the ventilating effect of subducted water also depends on the timescale of re-entrainment by the mixed layer which is uncertain near these sites (Jones et al., 2016) and can be influenced by ocean currents (Jones et al., 2019). Re-entrained water has no long term influence on the heat (e.g. Frölicher et al., 2015), carbon (Sallée et al., 2010), or nutrient (Sarmiento et al., 2004) budgets of the global interior ocean. Here, we study the spatial and temporal patterns of ventilation using a method that considers the dynamics of subduction and re-entrainment.

Extensive backwards-in-time trajectory experiments reveal the history of the interior ocean including a record of the position and timing of ventilation. For example, MacGilchrist et al. (2020) find that 60% of ventilation in the Labrador Sea

occurs within the boundary current and only 20% arises from deep ocean convection. Ventilation sites do not require deep mixed layers when the dynamics of subduction, re-entrainment, and ocean currents are considered. Using similar methodology, MacGilchrist et al. (2021) find that the North Atlantic almost entirely ventilates in late winter, in agreement with the earlier passive tracer experiment by Williams et al. (1995) and the theory of 'Stommel's Demon' (Stommel, 1979). The demon has enabled simpler models of the ocean thermocline, where the base of the late-winter mixed layer is adopted as a non-seasonal upper boundary (e.g. Marshall et al., 1993).

Figure 4.1a and 4.1c show the maximum mixed layer depth (MLD) of the Southern Ocean in 2012 from a forced model and reanalysis respectively (details are given in Section 4.2). A feature of the MLD in the Southern Ocean is its variation along the Antarctic Circumpolar Current (ACC). The maximum MLD varies between 100 and 500 m along the ACC's time-averaged streamlines for 2012 and this could influence ventilation timing in the Southern Ocean. Figure 4.1a shows the -10, -60, and -110 Sv streamlines of the ACC (black) alongside the 20 Sv streamlines of the subpolar gyres (red).

Stommel's demon relies on the net movement of subducted water to regions with a similar or deeper maximum MLD. In the ACC, water that subducts outside of late winter may escape re-entrainment by advecting to an area with a shallower maximum MLD. It is also possible that the substantial mesoscale eddy activity of the Southern Ocean will affect the ventilation process (Kamenkovich et al., 2017; Kwon, 2013; Marshall, 1997; Sallée et al., 2010).

We use extensive backwards-in-time trajectories to study the important sites and timing of all ventilation in the Southern Ocean. We also take the unique opportunity to compare the properties of shelf-ventilated and off-shelf-ventilated waters using data from a single experiment.

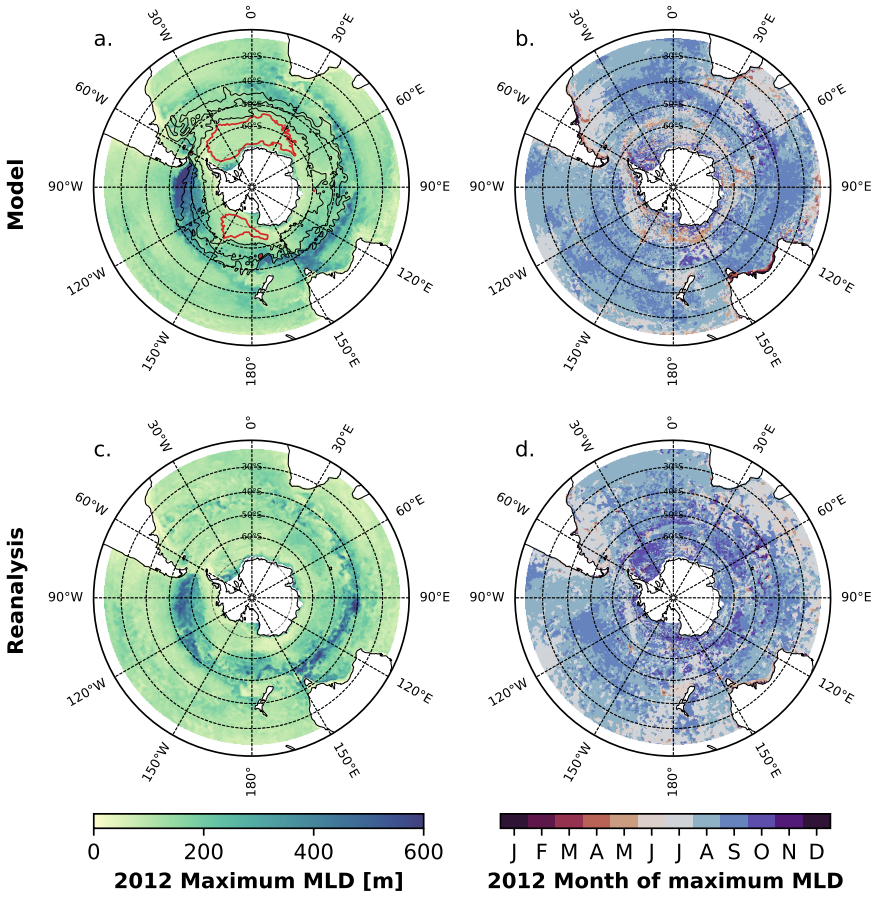

Figure 4.1: The maximum mixed layer depth (MLD) in 2012 (a) simulated by the forced model and (c) estimated by reanalysis. The timing of the MLD maximum is shown in (b) and (d). The red contours in (a) are the 20 Sv streamlines of the subpolar gyres. The black contours in (a) are the -10, -60, and -110 Sv streamlines of the ACC.

4.2 Numerical Simulation and Lagrangian Trajectory Analysis

We use backwards-in-time Lagrangian trajectory analysis in a forced ocean-sea-ice model. The numerical simulation is an implementation of the NEMO model (Madec et al., 2019) coupled with the LIM-2 sea-ice model (Bouillon et al., 2009) and was carried out as part of the Drakkar project (Barnier et al., 2006). The ORCA025 configuration is used, which has a horizontal resolution of 1/4° (∼ 12 km at 65°S and refines with latitude) and 75 irregular vertical model levels. The model is 'eddy-permitting', meaning that only the largest mesoscale eddies are resolved. The simulation runs from 1958 to 2015 and is forced with Drakkar

Forcing Set 5.2 (Dussin et al., 2016).

Figure 4.1 compares the forced model to reanalysis from ORAS5 (Zuo et al., 2019) for 2012. The forced model is able to reproduce a similar maximum MLD at a similar time of the year to the observationally-constrained reanalysis. Throughout this study, we define the MLD as the depth where the potential density (reference pressure of 0 dbar) is within 0.01 of the 10 m depth value. The MLD is deep to the west of the Drake Passage and south of Australia and the deepest mixed layers occur between August and September. This is in agreement with previous studies (Buongiorno Nardelli et al., 2017; de Boyer Montégut et al., 2004; Dong et al., 2008; Hanawa and D.Talley, 2001; Sallée et al., 2008; Sallée et al., 2010). One notable discrepancy is the thin regions of summer maxima (approximately April) that are visible in the forced model. This is not a consistent feature in the years before 2012 and may arise from anomalous wind forcing in the simulation that year.

The trajectories are calculated using the Lagrangian trajectory code, TRACMASS v7.1 (Aldama-Campino et al., 2020). TRACMASS analytically calculates the trajectory through each model grid cell by assuming that each component of the three dimensional velocity field varies linearly with its respective direction (Blanke and Raynaud, 1997). The trajectories are purely advective and calculated using model velocities that are interpolated between successive 5-day-mean velocity fields. By assuming that the velocity field remains stationary between the intermediate time steps, TRACMASS can calculate approximately mass-conserving trajectories (Döös et al., 2017). NEMO is an incompressible model, so the volume associated with each trajectory is approximately conserved.

We evaluate backwards-in-time trajectories for all interior water that is south of 25°S on the 16th December 2012. Each trajectory has an associated subvolume with a maximum volume of 10^9 m^3. Over 480 million trajectories are calculated, meaning there are significantly more trajectories than there are grid cells. Backwards-in-time trajectories reveal the advective history for each of these subvolumes. The earliest point in a subvolume's history is the most recent occurence of one of the following:

- it lies in the mixed layer (*Ventilated*);

- it is located north of 25°S;
- it is more than 30 years old.

In this study, we focus on trajectories with histories starting under the first condition ('ventilated' trajectories hereafter). These are the subvolumes that ventilate south of 25°S between 1982 and 2012 and then remain in the ocean interior of this region until the 16$^{\text{th}}$ December 2012.

4.3 Results

In total, 5.80×10^{16} m^3 of water (62 million trajectories) are ventilated in our experiment via purely advective pathways. Figure 4.2a shows the age distribution of the ventilated volume. During 2012, the mean MLD is largest in August (Figure 4.2b) and in our experiment 34% (2.0×10^{16} m^3) of the ventilated volume subducts after this date. These ventilations are 'short term' because they may not escape seasonal re-entrainment. The remaining 66% (3.8×10^{16} m^3) of the ventilated volume have escaped re-entrainment. We will be considering the statistics of these 'long term' ventilations for the remainder of this chapter.

In Figure 4.2a, there is noticeable inter-annual variabilty in ventilation which may originate from variations in subduction, re-entrainment or the interior circulation. This suggests that the Southern Ocean is more receptive to surface conditions in specific years of its history. Decadal variability, which may be significant in the Southern Ocean (e.g. Ting and Holzer, 2017; Waugh et al., 2013; Waugh et al., 2019), cannot be resolved in our thirty year experiment.

Throughout the study, we consider statistics that are aggregated by horizontal position. A single trajectory has two important locations associated with it:

- their final position: the subvolume's location on the 16th December 2012,
- their ventilation position: where the subvolume most recently subducted before the 1$^{\text{st}}$ August 2012 (MLD maximum).

We use this terminology throughout the chapter and label all figures with 'Final' and 'Vent' accordingly. There are also two important densities, the potential density at subduction (subduction density hereafter) and the approximate neutral density of the subvolume in its final position (final density hereafter). The neutral density is estimated by calculating approximate neutral density surfaces (ω-surfaces) using the methodology of Stanley et al. (2021). Ideally, approximate neutral density surfaces would be used for subduction density as well, but calculating approximate density surfaces for all time steps in this experiment was too computationally expensive. Both the densities use a reference pressure of 0 dbar and agree near the ocean surface where subduction takes place. For the remainder of this chapter, all values of neutral and potential density have had 1000 kg m^{-3} subtracted from them and then trivially divided by 1 kg m^{-3} to form a dimensionless quantity.

4.3.1 Stommel's Demon in the Southern Ocean

We find that the timing of ventilation in the Southern Ocean is highly seasonal. In Figure 4.2b we aggregate all of the ventilated trajectories by their month of ventilation. The majority of subduction occurs between August and November. Everywhere in the Southern Ocean ventilates at approximately the same time of year (Figure 4.2e). Just like in the North Atlantic (MacGilchrist et al., 2021), the common months of ventilation are when the mixed layer is shoaling. There are so few cases of subduction before July that all sub-regions considered in this study show a similarly seasonal distribution. This is strong evidence that Stommel's Demon operates in the Southern Ocean.

Ventilation between August and November, when the mixed layer is shoaling, is skewed towards earlier months in the year. The modal month of ventilation is October but far more ventilation occurs in September compared to November even though the rate of mixed layer shoaling is comparable. This skew may be related to the necessary timescale for escaping re-entrainment. Water that subducts in November only has 4 months before the mean mixed layer depth returns to

a similar depth in March. This is in contrast to the approximate 10 months for September-ventilated water.

The mean trajectory age for each final horizontal position is shown in Figure 4.2d. Water in the subpolar gyres is found to be particularly old (over 20 years) towards the center of the gyres. The white spaces in the centre of the gyre inform us that no subvolumes have ventilated. Figure 4.2f shows that, compared to the Antarctic margins and the ACC, the gyre basins are poorly ventilated regions when considering a thirty year timescale of ventilation. In Section 4.3.3, we investigate the partial ventilation of the Weddell Gyre.

4.3.2 Ventilation sites and their properties

We now aggregate the trajectories by their horizontal location of ventilation to identify the common sites of ventilation and the properties of water that ventilates there. Figure 4.2g shows the volume ventilated at each ventilation position. There is practically no ventilation within the subpolar gyres and ventilation primarily occurs on the continental shelf or at the northern front of the ACC. Any water that subducts within the subpolar gyres is swiftly re-entrained by the dynamic mixed layer. The centre of the subpolar gyres may be exclusive hotspots for upwelling into the mixed layer, which could be revealed using an equivalent forwards-in-time trajectory experiment. Alternatively, the centre of the subpolar gyres offer ventilation via diffusive pathways which could be seen in tracer dye experiments similar to Solodoch et al. (2022).

In the open ocean, there is circumpolar ventilation along the northern front of the ACC and the zonal symmetry is broken by several ventilation hotspots (Figure 4.2g). The ventilation hotspots roughly align with subduction hotspots from observational studies (e.g. Buongiorno Nardelli et al., 2018; Morrison et al., 2022; Sallée et al., 2010; Sallée et al., 2012) and align with areas of deep convection (Figure 4.1a). In Section 4.3.4, we assess the significance of the ventilation hotspots.

Figure 4.2h shows the median final density of the subvolumes based on their ventilation position. This indicates the eventual density of the water that ventilates

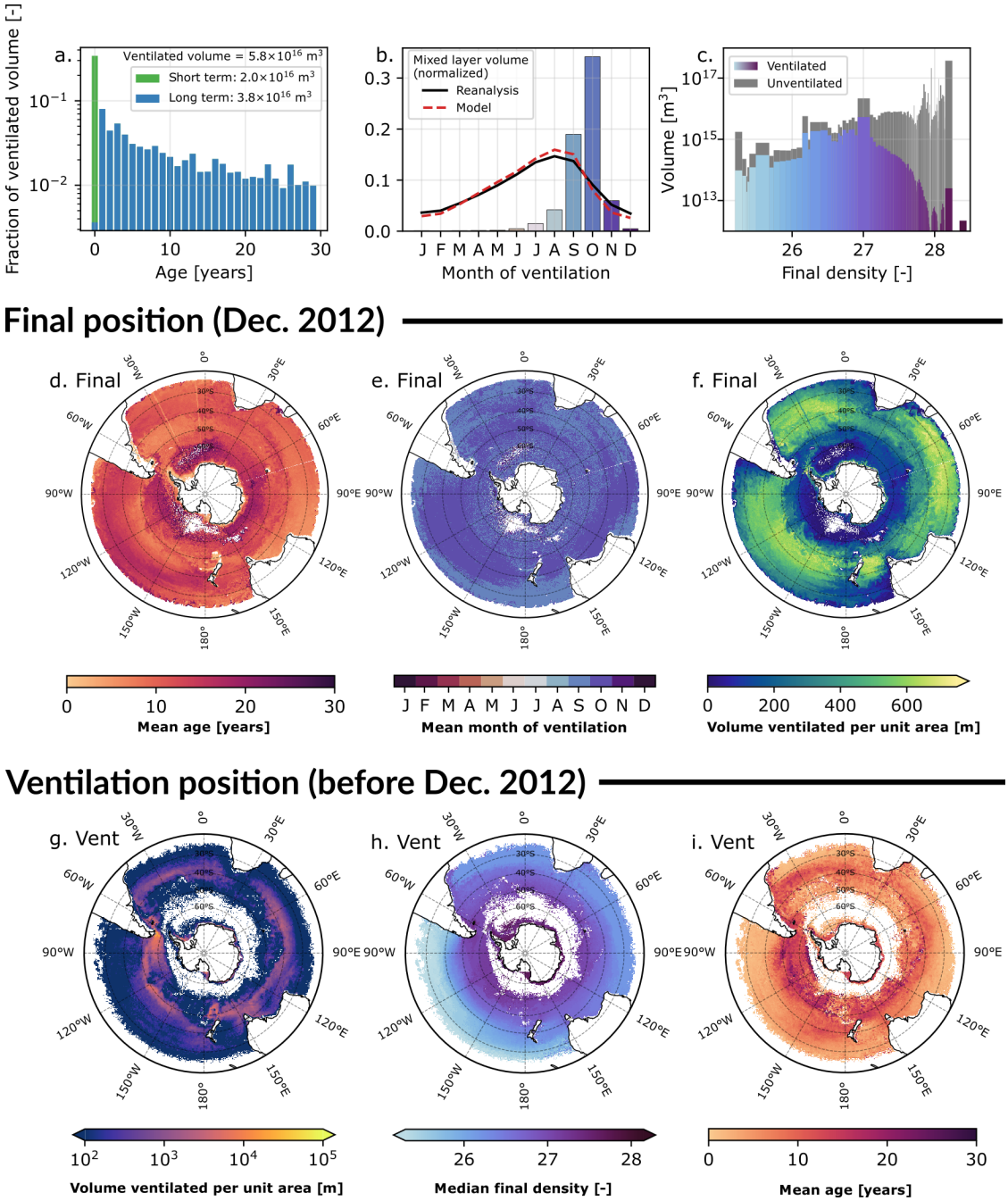

Figure 4.2: (a) The age distribution of the ventilated trajectories. (b) The ventilated volume aggregated by month and the 2012 mixed layer volume distribution. (c) The ventilated and unventilated volume aggregated by the final density. (d)-(f) The mean age, mean month of ventilation and ventilated volume aggregated by final position. (g)-(i) The ventilated volume, median of the final density, and the mean age aggregated by ventilation position.

at these sites. The lightest water masses ventilate in the Pacific sector and as expected, the densest waters in the Southern Ocean ventilate on the Antarctic shelf and the least dense waters ventilate north of the ACC.

This result is not trivial since climate models can exaggerate the frequency of open-ocean deep-convection events (Heuzé et al., 2015; Reintges et al., 2017). The mean age of a subvolume also varies significantly with the location of ventilation (Figure 4.2i). Subvolumes that ventilate in areas with deep mixed layers (e.g. west of the Drake Passage) have a mean age between 10 and 20 years. Elsewhere, subvolumes typically have a mean age between 0 and 10 years.

4.3.3 Ventilation of the Weddell Gyre

We now only consider trajectories that have a final position within the 10 Sv streamline of the Weddell Gyre. The two important sites of ventilation are: the Antarctic Shelf and west of the Drake Passage (Figure 4.3a) where the maximum MLD is deep (Figure 4.1a). Studying both the mean age (Figure 4.3c) and the average final density (Figure 4.3d) reveals discrete sources for water of specific density or age in the Weddell Gyre. The youngest waters (5 years or younger) ventilate close to the Weddell Gyre in the southern limits of the Weddell Sea. These young waters have a median final density between 27.5 and 27.75. A similarly young population of water also ventilates in the ACC between 150 and 90°W. These waters end up as some of the lowest density water masses in the Weddell Gyre interior (approximately 27.25).

The densest waters (above 27.75) found in the Weddell Gyre ventilate on the Antarctic shelf with a mean age between 10 and 20 years. Similarly dense but much older water (25-30 years) also ventilate at the site of deep convection west of the Drake Passage (90-60°W). In Section 4.3.7, we find evidence that this water has experienced interior densification since ventilating.

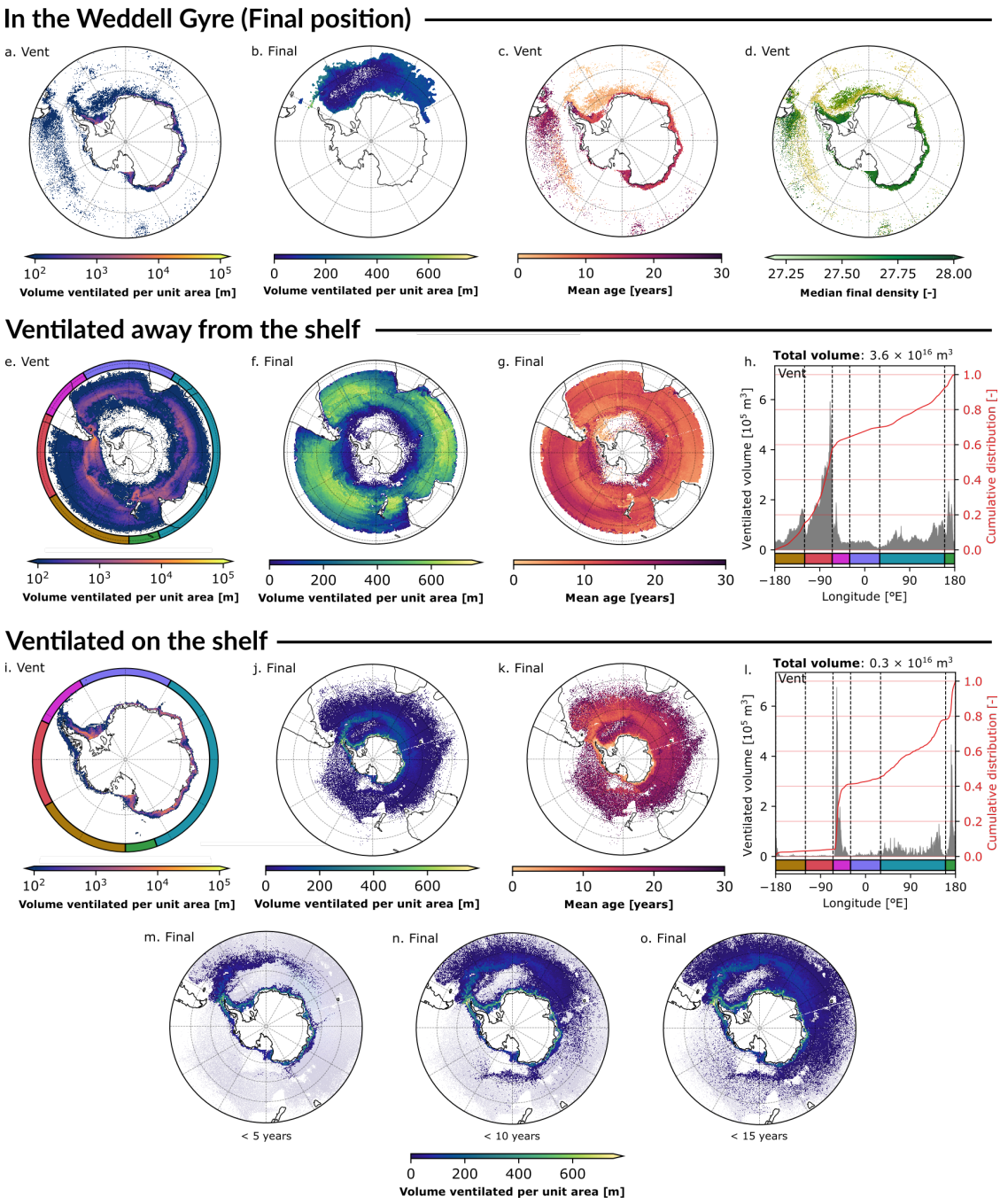

Figure 4.3: The statistics of ventilated trajectories that have a final position in the Weddell Gyre, ventilated away from the Antarctic shelf, or ventilated on the Antarctic shelf. All quantities are calculated and presented in the same way as Figure 4.2. The gray bars in (h) and (l) show the longitudinal variation of off-shelf and on-shelf ventilated volume respectively. The red line is the cumulative distribution function. The colored bars span the same longitudinal range as the colored arcs in (e) and (i). (m)-(o) the ventilated volume for trajectories that are less than 5, 10, and 15 years old.

4.3.4 Ventilation away from the shelf

We now only consider trajectories that ventilate away from the Antarctic shelf. A trajectory is assumed to have ventilated away from the shelf if its ventilation position is outside the closed 2000m isobath surrounding Antarctica. Figure 4.3f shows the final distribution of these ventilation subvolumes. Few subvolumes end up in the subpolar gyres or on the shelf. Although there are clear hotspots of ventilation (Figure 4.3e), the recently subducted water is efficiently spread out across the ACC and north of it, in agreement with Jones et al. (2016), Sallée et al. (2010), and Sallée et al. (2012). These hotspots have been argued to originate from bathymetric constraints which affects the MLD distribution, steers the circulation, and modifies the isopycnal tilt (Sallée et al., 2010).

Figure 4.3h shows how the ventilated volume varies with the longitude of ventilation. Two subduction hotspots dominate the ventilation between 180 and 65°W, where 60% of ventilation occurs. Around the remainder of Antarctica, the hotspots are less apparent as ventilation varies smoothly with longitude, suggesting a more circumpolar pattern of ventilation. This result suggests that subduction hotspots offer a partial view of open Southern Ocean ventilation.

4.3.5 Ventilation on the shelf

We now only consider trajectories that ventilate on the Antarctic shelf, within the closed 2000m isobath surrounding Antarctica (Figure 4.3i). On a thirty year timescale, shelf-ventilated waters are mostly contained south of the ACC but can travel to more northerly latitudes (Figure 4.3j). In Figure 4.3k, the youngest subvolumes in the interior ocean are found on the western boundary of the Weddell Gyre (60°W). This region is the most significant export pathway for shelf-ventilated water. Another weaker pathway follows the western boundary current of the Ross Gyre. Within five years of ventilating on the shelf (Figure 4.3m), some subvolumes have wrapped around the northern limb of the Weddell Gyre and started to traverse the western boundary of the Ross Gyre (160 °E). Within ten years (Figure 4.3n), trajectories have started to wrap around the Ross Gyre and be dispersed by the

ACC. Similar export pathways have been found in the passive tracer experiments of Solodoch et al. (2022). The remote ventilation of the northern limb of the Weddell Gyre may explain the Weddell-Scotia confluence (Patterson and Sievers, 1980), a zone separating the Weddell Sea from the Scotia with temperatures and salinities that are far more homogeneous than the surrounding waters.

The on-shelf ventilation is more localized than the off-shelf ventilation (Figure 4.3l). Approximately 40% of the shelf's ventilation takes place on the eastern side of the Antarctic Peninsula (65-30°W) and an additional 20% takes place in the west Ross Sea (160-180°E). These ventilation hotpots align with two of four observed sites of AABW formation on the Antarctic shelf (Purkey et al., 2018). The other two sites (Prydz Bay and the Adélie Coast) are not clearly pronounced. This may be because insufficient dense water is being formed at these sites in the forced model or alternatively, the dense water that forms at these sites is swiftly re-entrained elsewhere along the Antarctic coastline. The remaining 40% of ventilation is evenly spread over East Antarctica (30-160°E), which contains both fresh and dense shelf regimes (see Figure 1.2a in Chapter 1). If the shelf properties are accurate in this model, then the fresh and dense shelf water regimes across East Antarctica are making comparable contributions to ventilation at a 30 year timescale.. Little ventilation takes place in West Antarctica (180-65°W), which aligns with the 'warm shelf' described in Thompson et al. (2018) (see Figure 1.2a).

4.3.6 Separability of shelf-ventilated water

Almost all of the statistics considered so far have been aggregated by horizontal position and we have ignored vertical variations. This raises the question, how much overlap is there of shelf-ventilated and off-shelf-ventilated water when considering ventilation on a thirty year timescale?

Figure 4.5a shows what fraction of the recorded ventilation in a water column originates from the Antarctic shelf. Most fluid columns in the Southern Ocean can be approximated as entirely ventilated on the shelf (100%, blue) or entirely ventilated off the shelf (0%, red). The interface between these two classes is narrow and aligns

closely with the southern front of the ACC (illustrated by the -10 Sv streamline in Figure 4.5a). In Section 4.3.5, we found that shelf-ventilated trajectories can travel north of the ACC in 30 years, but Figure 4.5 suggests that the volume of these trajectories is negligible compared to the volume of off-shelf-ventilated water.

This result highlights the different rates of ventilation for shelf-ventilated and off-shelf-ventilated water. In thirty years, approximately ten times more water ventilates in the open ocean ($3.6 \times 10^{16}\text{m}^3$) compared to the Antarctic shelf ($0.3 \times 10^{16}\text{m}^3$), even though shelf-ventilated abyssal waters make up most of the Southern Ocean (Figure 4.2c). This behaviour is consistent with the two-dimensional MOC (see Section 1.1 and Figure 1.1b) where shelf-ventilated water is contained south of the ACC as part of the deep cell.

To help the reader relate these findings to observational studies, Figure 4.4 shows the aggregated ventilation properties of the subvolumes based on their final conservative temperature and absolute salinity combination (T-S properties). Figure 4.4a is the T-S distribution in December 2012, when the subvolumes are in their final position alongside the approximate locations of commonly considered water masses (Pardo et al., 2012). Figure 4.4b shows the total ventilated volume in T-S space while 4.4c shows what fraction of the total volume ventilated in the 30 year experiment. A significant fraction of intermediate and mode water masses have ventilated in the experiment ($> 40\%$ ventilated). In contrast, deeper and denser water masses with properties similar to Circumpolar Deep Water, North Atlantic Deep Water, and Antarctic Bottom Water do not fully ventilate in our thirty year experiment ($< 10\%$ ventilated). A backwards-in-time experiment run for a longer period of time may provide further insight into the ventilation of the densest water masses.

4.3.7 Density distribution

Finally, we consider the structure of Southern Ocean ventilation in density-latitude space (Figure 4.5c-4.5j). The circumpolar statistics are considered alongside the statistics of the Atlantic, Indian, and Pacific sectors (Figure 4.5). Following on from the previous subsection, a line in density-latitude space separates shelf-ventilated and

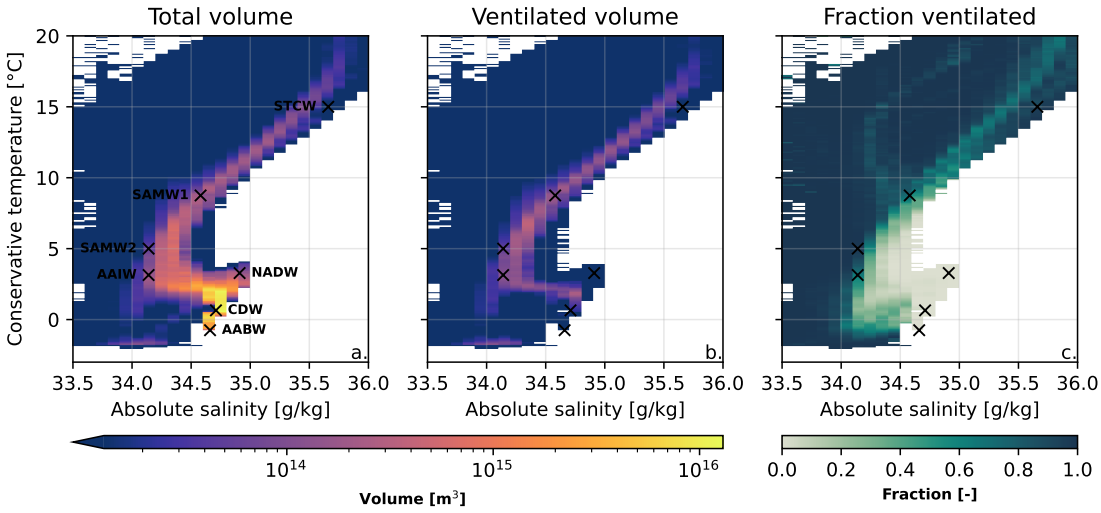

Figure 4.4: (a) The total volume (ventilated plus unventilated) of the Southern Ocean aggregated by the final conservative temperature and final absolute salinity. (b) The ventilated volume aggregated by the final T-S properties of the subvolume. (c) The fraction of water ventilated by location in T-S space. The approximate locations of commonly considered water masses are marked with crosses using tables from Pardo et al. (2012). STCW = Subtropical Central Water, SAMW1 and SAMW2 = Two branches of Sub-Antarctic Mode Water, AAIW = Antarctic Intermediate Water, NADW = North Atlantic Deep Water, CDW = Circumpolar Deep Water, AABW = Antarctic Bottom Water.

off-shelf-ventilated water. The line is not well defined at latitudes greater than 45°S, because so little shelf-ventilated water reaches this latitude on a thirty year timescale.

Most shelf-ventilated water has a final density between 27.25 and 28.00; off-shelf-ventilated water has a final density between 25.50 and 27.75 (Figure 4.5d). The densest shelf-ventilated waters are found in the Atlantic sector (Figure 4.5f), while the lightest shelf-ventilated waters are in the Pacific (Figure 4.5j). Similarly, the lowest density off-shelf-ventilated waters are found in the Pacific and the highest density subvolumes are found in the Atlantic. This suggests that the lower density Pacific-ventilated waters (Figure 4.2h) remain in the Pacific. The tendency for denser waters to ventilate in the Atlantic may be related to the presence of the Atlantic Meridional Overturning Circulation.

To understand the trajectory of these volumes in density space, we need to see their density transformation in the ocean interior. Figure 4.5b compares the subduction density to the final density. The central line shows the median subduction

density while the lower and upper lines show the 5^{th} and 95^{th} percentile. These lines represent the envelope of transformation that 90% of the subvolumes experience and the color shows the shelf water fraction.

A fraction of any transformation found in this study may be numerical and could originate from the following: cumulative errors in the trajectory calculation (van Sebille et al., 2018), the approximation of neutral density surfaces (Stanley et al., 2021), and implicit model mixing (Griffies et al., 2000; Lee et al., 2002). Megann (2018) found implicit mixing to be similar to or greater in magnitude than parameterized mixing in a related NEMO ocean model.

Water with a final density less than 27.0 has a similar median subduction density (Figure 4.5b). On average, little transformation takes place and the spread of the subduction density indicates that the range of transformation is within 0.5 of the median. In contrast, almost all water with a final density greater than 27.0 has become more dense since subduction. The most extreme cases of densification originate from shelf-ventilated trajectories with a final density greater than 27.75 and an age greater than 5 years. In Section 4.3.3, some of this transformed water is identified in the Weddell Gyre (Figure 4.3d). Poorly ventilated dense water and interior densification of lighter water masses indicate that reserves of denser bottom water are being eroded by interior transformation processes. Presumably, the shelf-ventilated waters interact with dense bottom water as they enter the subpolar gyres and/or follow the ACC (Figure 4.3n). Studies indicate this may be happening in the Southern Ocean as a consequence of climate change (e.g. Li et al., 2023; Purkey and Johnson, 2010; Zhou et al., 2023) via glacial melt. The forced model run does include climate change and glacial melt but the effect could be exaggerated by model biases or drifts similar to those found in climate models (Heuzé, 2021; Purich and England, 2021).

4.4 Conclusions

We have used backwards-in-time trajectories to study a thirty year history of the Southern Ocean and identified spatial and temporal patterns of ventilation that will

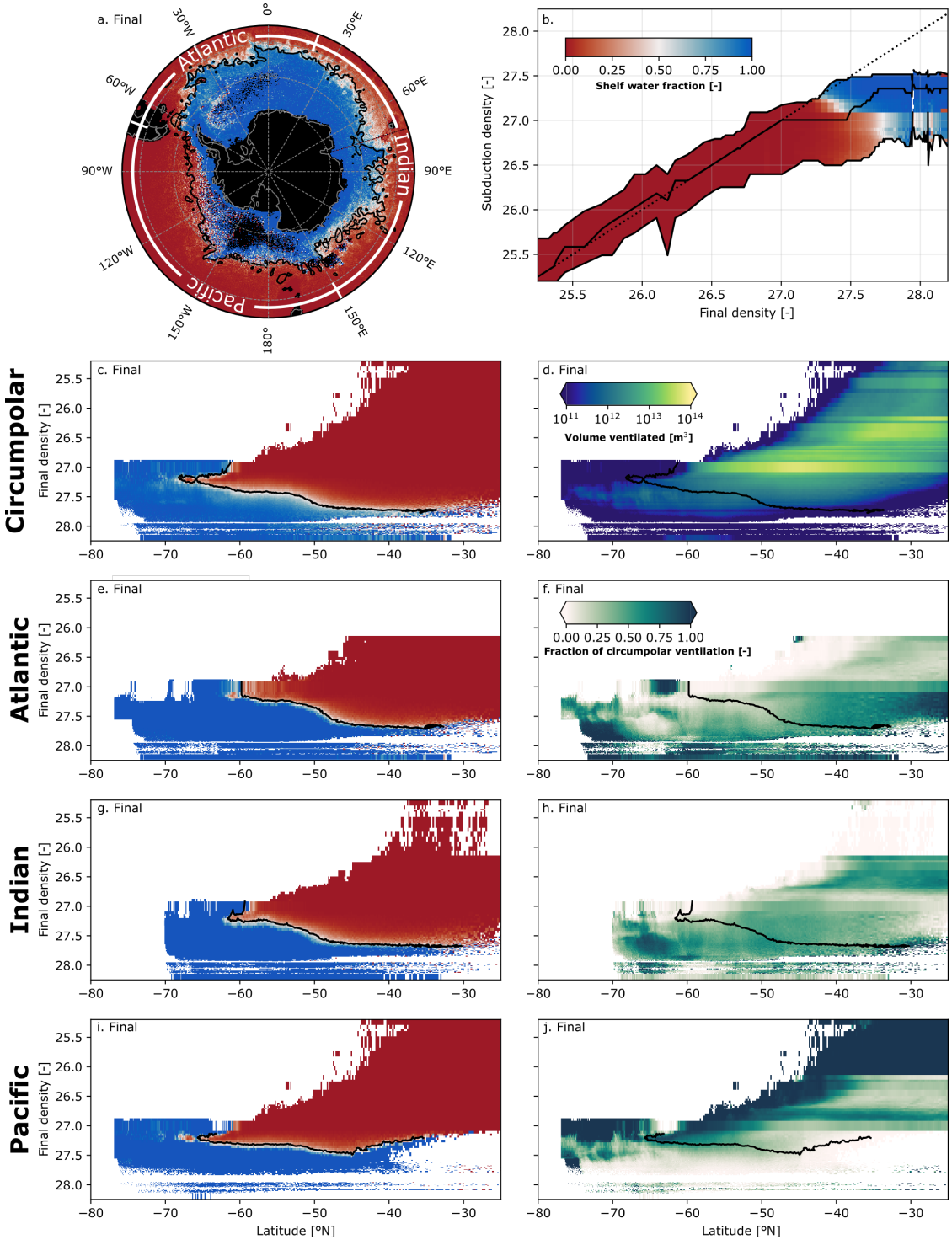

Figure 4.5: (a) The shelf water fraction aggregated by final position. The black contour is the -10 Sv streamline of the ACC in December 2012. (b) Comparing the subduction density to the final density. The central line shows the median subduction density. The upper and lower lines show the respective 5^{th} and 95^{th} percentile. (c),(e),(g),(i) The shelf water fraction in density-latitude space across various sectors of the Southern Ocean. (d),(f),(h),(j) Ventilation in density-latitude space across the same sectors. The black line in (c)-(j) is the approximate boundary between shelf-ventilated and off-shelf-ventilated waters.

simplify conceptual models. We found conclusive evidence that ventilation in the Southern Ocean is highly seasonal. Despite significant variations of the MLD along the streamlines of the ACC and significant eddy activity, Stommel's demon only allows ventilation between August and November. There is also evidence of inter-annual variability (Figure 4.2a); future studies should investigate if an inter-annual demon operates as well using the methodology of MacGilchrist et al. (2021).

We identified spatial patterns of ventilation in the open Southern Ocean. Circumpolar ventilation takes place along the northern front of the ACC and the zonal symmetry is broken by several ventilation hotspots (Figure 4.2g). The hotspots of ventilation overlap with sites of deep convection (Figure 4.1a) and local regions of subduction from observational studies (Buongiorno Nardelli et al., 2017; Sallée et al., 2010; Sallée et al., 2012) but they only account for 60% of open-ocean ventilation. Circumpolar patterns of ventilation and ventilation hotspots have similar levels of influence on the Southern Ocean.

We also calculated the median final density based on the location of ventilation. This describes the average eventual density of water that ventilated at a given location. In the open-ocean, the density distribution has both a circumpolar and regional pattern (Figure 4.2h). At all longitudes, the median final density decreases with latitude but there is clear zonal variation as well. Most noticeably, the lightest water masses of the Southern Ocean tend to ventilate in the south-east Pacific. This may be relevant when considering the well-debated ventilation patterns of Antarctic intermediate water. Sverdrup et al. (1942) argued that the water mass is formed through homogeneous subduction along the ACC while McCartney (1979) argued that Antarctic Intermediate Water originates from deep convection in the south-east Pacific. A dedicated backwards-in-time trajectory experiment which specifically targets Antarctic intermediate water may help to determine where the water mass ventilates in eddy-permitting simulations.

Almost no ventilation takes place in the subpolar gyres (Figure 4.2g). Any subduction that occurs within the streamlines of the gyres is swiftly re-entrained by the following mixed layer seasonal cycle. It is worth remembering that the

experiment only reveals advective pathways of ventilation, so it is possible that ventilation does take place in the gyre centre but via a diffusive mechanism. This could be tested using dedicated dye experiments similar to Solodoch et al. (2022). On a thirty year timescale, water in the Weddell Gyre ventilates remotely. The subvolumes primarily ventilate on the Antarctic shelf but also ventilate west of the Drake Passage where the mixed layer is deep (Figure 4.3a).

The Antarctic shelf is where the densest water masses of the Southern Ocean ventilate and we find that 40% of shelf ventilation occurs on the Antarctic Peninsula and 20% in the west Ross sea (Figure 4.3l). These are two known sites of AABW formation on the Antarctic shelf but other sites are not clear in the model. The remaining 40% of ventilation is spread over East Antarctica. Shelf-ventilated waters are exported to the Southern Ocean via two export pathways, parallel to the western boundaries of the Weddell and Ross Gyre (Figures 4.3m and 4.3n) in agreement with passive tracer experiments (with diffusion) by Solodoch et al. (2022).

Abyssal waters north of the ACC hardly ventilate on a thirty year timescale (Figure 4.2c) because shelf-ventilated waters need significantly more time to cross the ACC. In contrast, off-shelf-ventilated waters experience more rapid ventilation in the open Southern Ocean but rarely travel south of the ACC (Figure 4.2f). Consequently, the southern boundary of the ACC approximately separates columns of shelf-ventilated and off-shelf-ventilated water (Fig 4.5a). This approximation predicts the area of effect for climate change in the Southern Ocean on anthropogenic timescales. Off-shelf-ventilated waters change quickly over a large area, while denser shelf-ventilated waters modify slowly but accumulate in the smaller area south of the ACC.

Finally, we compared the subduction density to the final density. On average, water with a final density lower than 27.0 experiences little transformation. Almost all water with a final density greater than 27.5 experiences densification after subduction (Figure 4.5b). On a thirty year timescale, the densest water masses do not form within the mixed layer; Instead, the dense water masses are being consumed to densify lighter water masses which have made contact with the mixed layer. This result is consistent with a warming world that is forming less AABW (e.g. Li et al.,

2023; Purkey and Johnson, 2010; Zhou et al., 2023) because of glacial melt but could be exaggerated by inaccuracies from the eddy-permitting model or the trajectory calculation. Repeating the experiment without a climate change signal could help to clarify this. If the interior transformation is still present, then it is a bias of the model. Additionally, running similar experiments on higher resolution models and reanalysis products could determine how realistic this climate change signal is.

4.5 End of chapter remarks

The extensive backwards-in-time trajectories presented in this chapter have revealed surprisingly clear spatial and temporal patterns across the entire Southern Ocean. The narrow time window for Southern Ocean ventilation, between August and November, will help simplify conceptual models of subpolar gyres and the Southern Ocean as a whole. In contrast to the spatial hotspots of ventilation, practically no ventilation occurs within the subpolar gyres but their western boundary currents are essential export pathways for shelf-ventilated water (see Figures 4.3m and 4.3n). There is plenty more to explore in the presented data set and future data sets of a similar kind. In the following chapter we conclude the thesis by discussing future avenues of research that branch from all of our results and summarize our main findings.

5 Conclusions

Contents

5.1 Summary

The Weddell Gyre is the largest coherent circulation south of the ACC. Sandwiched between the upwelling of the ACC and the downwelling on the Antarctic shelf, the southern subpolar gyres mediate the transport of water between these two important sites for the MOC. Unfortunately, the dynamics of the Weddell Gyre and its influence on the wider Southern Ocean is understudied compared to northern subpolar gyres. To remedy this, the Weddell Gyre has taken centre stage in this thesis and it has been studied using a wide range of methods.

In Chapter 2, we used an idealized model to investigate how mesoscale eddies and the ACC strength influence the Weddell Gyre. We found that the idealized

gyre is extremely sensitive to horizontal resolution. As shown in Figure 2.7, when the horizontal resolution increases from eddy-parameterized to eddy-permitting values, the gyre transport approximately doubles over smooth bathymetry (from 28.9 Sv to 54.7 Sv) and quadruples over noisy bathymetry (from 11.9 Sv to 44.8 Sv). This is a robust result and cannot be tuned out by adjusting the constant GM eddy parameterization (Figure 2.13). This is similar to the behaviour of the Weddell Gyre in global simulations by the Met Office (Section 1.4 and Figure 1.3).

The idealized ACC is similarly sensitive to horizontal resolution but remarkably we find that large variations in the ACC strength (induced by varying the bathymetry of the Drake Passage) have little influence over the Weddell Gyre transport. As seen in Figure 2.8, the ACC would need to vary its strength by approximately 100 Sv to modify the Weddell Gyre transport by 1 Sv. This result allows us to safely conclude that the Weddell Gyre is sensitive to local variations in the horizontal resolution and not the knock-on effects of a modified ACC transport. A potential mechanism for the insensitivity is discussed later on in this Chapter in Section 5.2.1.

The idealized model lacks a neighbouring Ross Gyre, which many argue is coupled to the Weddell Gyre via a 'supergyre circulation' (Sonnewald et al., 2023; Wang, 2013). The Weddell Gyre may be insensitive to the ACC transport, but it may be strongly coupled to the Ross Gyre transport. The connectivity of the southern subpolar gyres could be explored further using a widened idealized model containing two subpolar gyres.

To quantify how the idealized gyre responds to the resolution of mesoscale eddies, we used a thermal wind and bottom flow decomposition of the circulation (Section 2.4.3). The depth-dependent flow was calculated using the thermal wind equation and the depth-independent flow is determined by the flow at the sea floor. When combined, the two components accurately describe the ACC and Weddell Gyre transport. In simulations with a rough bathymetry, the depth-dependent component of the gyre transport is largest at eddy-permitting resolutions (Figure 2.9c) because the isopycnals in the gyre basin are particularly steep (Figure 2.11). As suggested by Isachsen (2011), eddy buoyancy fluxes can be significantly reduced over steep

topographic features, enabling large horizontal density gradients over the idealized submarine ridge. This effect appears to be exaggerated when only the largest mesoscale eddies are resolved. Steep isopycnals drive a thermal wind transport for the gyre but also fuel tall columns of eddy kinetic energy (Figure 2.6) which can excite the bottom flow via non-linear dynamics (Adcock and Marshall, 2000; Bretherton and Haidvogel, 1976; Holloway, 1987; Holloway, 1992). When smaller eddies are resolved in the eddy-rich simulation, the depth-dependent and depth-independent components of the gyre respond differently. Increased eddy buoyancy fluxes cause the isopycnals to slump and the gyre's thermal wind transport decreases. In contrast, the increased eddy kinetic energy intensifies the depth-independent flow via non-linear dynamics. The reduction in the thermal wind transport is slightly larger than the intensification of the depth-independent flow so the gyre transport slightly decreases when the resolution is increased from eddy-permitting to eddy-rich values.

In Chapter 3, we studied the dynamics of the Weddell Gyre from a different angle. We used vorticity diagnostics to identify the relevant forces balances for the Weddell Gyre. When terms in the vorticity budget are integrated over a large area, the dynamics of a circulation, realistic or idealized, can be straightforward to interpret. Integrating the vorticity diagnostics within the streamlines of a realistic Weddell Gyre simulation reveals a major limitation of the C-grid. Analytically, the Coriolis term of the vorticity budget should vanish when integrated within the area of a closed streamline. However, when calculated on the C-grid, this is not necessarily true. This spurious force dominates the vorticity budget of the simulated Weddell Gyre and is similar in size to the wind stress (Figure 3.14).

For the benefit of the ocean modelling community, we explored the origins of the spurious force. We identified five components of the spurious force which can survive the contour integration process. In the case of the Weddell Gyre the two dominant terms emerge from the model's representation of the sea floor (Figure 3.14b). The largest term originates from steps in the model bathymetry (Section 3.3.3 and Figure 3.2) where an explicit force balance cannot be resolved. The second term arises from varying cell thicknesses which are typical in a partial cell representation of the sea

floor. The magnitude of the spurious force makes the vorticity budget of the Weddell Gyre difficult to interpret and it is unclear whether the spurious force corrupts the overall circulation or if it is simply a diagnostic limitation of the C-grid. We tackle this question later on in this chapter in Section 5.2.3. One conclusion is clear though: the vorticity budget of a C-grid model should be approached with caution.

From the analysis presented in this thesis, we know for certain that the spurious force strictly arises from the geometry of the C-grid and not a specific method of calculating the Coriolis acceleration (see Appendix A.3 for a demonstration of this). However, what determines the magnitude of the spurious force is still nebulous and should be investigated further. Possible determining factors include the sea floor geometry, the circulation properties, the surface forcing, and the resolution (horizontal and vertical). We are confident though that the only way to remove the spurious force completely is by changing the grid geometry. For example, all four components of the spurious force vanish when the B-grid is adopted. Alternatively, using a terrain-following coordinate prevents model level steps from corrupting the vorticity budget of C-grid models.

In Chapter 4, we took a step back from the fine details of model numerics and mesoscale eddies to look at the spatial and temporal patterns of ventilation. We used backwards-in-time trajectories to calculate the thirty year history of subvolumes in the Southern Ocean (south of 25°S) and found conclusive evidence that the ventilation of the Southern Ocean is similarly seasonal to the North Atlantic. Stommel's demon (Stommel, 1979) operates in the Southern Ocean and only allows ventilation between August and November (Figure 4.2b).

The experiment revealed several important sites for ventilation of the Southern Ocean. Sites which align with subduction hotspots from observational studies (e.g. Buongiorno Nardelli et al., 2018; Sallée et al., 2012) ventilate 60% of the open Southern Ocean on a thirty year timescale (Figure 4.3h). The remaining 40% ventilates in a circumpolar pattern along the northern front of the ACC. This suggests that subduction hotspots only offer a partial view of Southern Ocean ventilation.

Practically no ventilation takes place within the Weddell Gyre or the Ross Gyre because any subduction that occurs within the streamlines of the subpolar gyres is swiftly re-entrained by the following mixed layer seasonal cycle. This is a more extreme case of the behaviour found in the Labrador Sea using similar backwards-in-time trajectories (MacGilchrist et al., 2020). In the Labrador Sea, approximately 25% of ventilated North Atlantic Deep Water ventilates in the gyre centre where there is variable deep convection while 60% ventilates in the boundary current.

The densest water masses ventilate on the Antarctic shelf and we find that 40% of the ventilation occurs on the Antarctic Peninsula and 20% in the west Ross Sea (see Figure 4.3l). These are two known sites of AABW formation (Purkey et al., 2018) but other sites (e.g. Prydz Bay and the Adélie Coast) are less clear. The remaining 40% is spread over East Antarctica. Figures 4.3m and 4.3n show that the western boundary currents of the Weddell Gyre and the Ross Gyre are the primary export pathways for shelf-ventilated water in our experiment. This result is consistent with observational evidence that Weddell Sea slope water export is closely tied to the Weddell Gyre's western boundary current (Meijers et al., 2016). This is further evidence that the Weddell Gyre transport is an important quantity in the global ocean and is a bridge for water that is exported from the Antarctic shelf. Whether the gyre is a bridge or barrier for water getting onto the shelf is still an open question. An equivalent forward-in-time trajectory experiment could be insightful, revealing the advective pathways onto the Antarctic shelf and the density transformation that subvolumes undergo during the process.

In thirty years, approximately ten times more water ventilates in the open ocean compared to the Antarctic Shelf, even though shelf-ventilated abyssal water make up most of the Southern Ocean. On a thirty year timescale, shelf-ventilated water can travel north of the ACC (see Figure 4.3j) but the volume is negligible compared to the amount of off-shelf-ventilated water. Similarly, negligible volumes of off-shelf-ventilated water travels south of the ACC. This means that the southern front of the ACC acts as an approximate boundary between shelf-ventilated and off-shelf-ventilated columns of water. This result predicts the area of effect for climate

change in the Southern Ocean on anthropogenic timescales. Off-shelf-ventilated water will respond quickly and affect a wide area, while denser shelf-ventilated waters will respond slowly but accumulate in the smaller area south of the ACC.

5.2 Outstanding Questions

The results presented in this thesis have not only expanded our understanding of the Weddell Gyre but also raised further questions about the circulation and its role in the Southern Ocean. Before concluding the thesis, we discuss some outstanding questions and highlight exciting avenues for future research.

5.2.1 Why is the Weddell Gyre so insensitive to the ACC strength?

One of the most surprising results of Chapter 2 is the idealized Weddell Gyre's insensitivity to the ACC strength (Figure 2.8). This result was convenient for our analysis but is also physically interesting. The ACC sensitivity study (Section 2.4.2) was conducted at eddy-parameterized and eddy-permitting resolutions with a rough bathymetry. Under these conditions the ACC strength is largely determined by thermal wind balance (see Figure 2.9d). We therefore expect the ACC isopycnals to slump when the ACC transport is reduced. Approximately half of the Weddell Gyre transport is controlled by horizontal density gradients, so why does the gyre transport not respond to the slumping of the ACC isopycnals?

One possible explanation is that the density structure of the gyre is largely controlled by Ekman upwelling south of the submarine ridge. Figure 5.1 shows the surface density of an eddy-permitting (20 km horizontal grid spacing) simulation alongside the surface forcing of the model used in Chapter 2. In simulations with explicit eddies, the highest surface densities are found on the shelf and immediately south of the submarine ridge (between the dashed lines in Figure 5.1). This region is also the area of peak negative wind stress curl and weak buoyancy forcing compared to the remainder of the gyre basin. It is therefore possible that there is an Ekman control on the maximum surface density which constrains the horizontal density

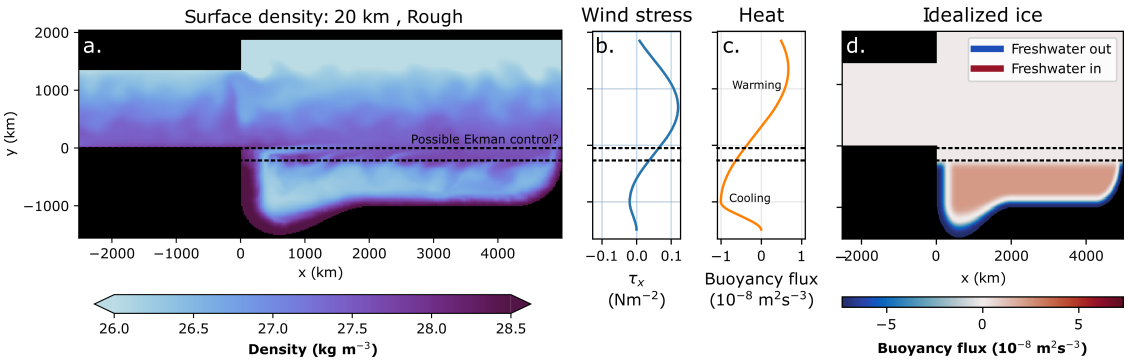

Figure 5.1: (a) The time-averaged surface density of an eddy-permitting simulation from Chapter 2. The simulation has a regular horizontal grid spacing of 20 km (eddy-permitting and a rough bathymetry). The surface forcing of the model is the same as Figure 2.2. The gyre's surface density structure might be controlled by Ekman upwelling between the dashed lines. (b) The zonal wind stress profile for the configuration. (c) The zonal heat flux profile for the configuration in units of buoyancy flux. (d) The freshwater fluxes used to represent sea ice for the configuration in units of buoyancy flux. In this model, a buoyancy flux of 10^{-8} m^{2}s^{-3} corresponds to 14.9 Wm^{-2} of surface heating or approximately $4{\times}10^{-5}$ kg m^{-2}s^{-1} of freshwater input (assuming a surface salinity of 35 psu).

gradients found in the gyre basin. It is unclear if a similar Ekman control operates further north, away from the submarine ridge and towards the ACC centre. It is possible that the steep topography of the submarine ridge is essential for the Ekman control. Alternatively, the intense eddy activity within the idealized ACC may disrupt the Ekman control mechanism.

In Chapter 2, we found that the Weddell Gyre is extremely sensitive to the resolution of mesoscale eddies so the gyre transport cannot be fully determined by surface forcing. However, it is possible that the large body of dense water upwelling against the submarine ridge is shielding the gyre's density structure from changes to the ACC's isopycnals. This mechanism would insulate the thermal wind transport of the gyre from large changes in the ACC transport, but does not explain why the depth-independent component of the gyre is also insulated. Further study may reveal that the steep topography of the submarine ridge shields the depth-independent gyre transport from the ACC. In eddy-parameterized simulations, indications of an Ekman control are not visible in the surface density structure. An alternative mechanism may be needed for the more diffusive simulations with parameterized eddies.

The insensitivity could be investigated further by varying the surface forcing in the idealized model and/or varying other properties of the ACC. For example, strengthening the depth-independent component of the ACC transport may be more effective at changing the gyre transport. It would also be interesting to see if the ACC insensitivity can be recreated in a realistic simulation. The realistic ACC transport could be modified by smoothing or coarsening the bathymetry of the Drake Passage.

5.2.2 Eddies in the Weddell Gyre

In Chapter 2, we found that the Weddell Gyre is extremely sensitive to the resolution of mesoscale eddies. The locations of eddy activity are flagged by the eddy kinetic energy (Figure 2.6) but a more in-depth eddy energy budget could be used. A complete eddy energy budget would describe the locations and mechanisms of energy exchange between the mean state and the eddy field. This method has been used in a wide range of studies (e.g. Guo et al., 2022; Zhai et al., 2010; Zhan et al., 2016). Advection terms in the energy budget could also clarify if the eddy kinetic energy found in the eastern limb of the Weddell Gyre (see Figure 2.6e) is imported from the ACC or generated there.

In our study, we were unable to fully resolve mesoscale eddies because of computational cost. The eddy-rich simulation in Chapter 2, has a regular horizontal grid spacing of 3 km which is above the Rossby deformation radius in the southern margins of the model. Looking at Figure 2.7c, it is natural to wonder if the Weddell Gyre transport will continue to decrease as the resolution is increased further. A future study with more computational resources or a more optimized model could answer this question. The performance of the model could be improved by shrinking the domain size, adopting an irregular grid, or by spinning up from the final state of a lower resolution model.

5.2.3 How problematic is the spurious force?

In Chapter 3, we identified a spurious force which is capable of dominating the vorticity budget of realistic (Figure 3.14) and idealized (Figures 3.9 and 3.10) gyres.

It is clear that this makes interpreting gyre vorticity budgets difficult but it is less clear if this spurious force corrupts the circulation itself. Here, we discuss three possible ways the spurious force may or may not affect circulation variables.

Firstly, it is possible that the spurious force performs the role of one or more real ocean processes which are required for an accurate simulation. In this case, the spurious force is simply a mislabelled physical force. In the case of the Weddell Gyre, it is tempting to suggest that the contribution from model level steps (Figure 3.14b) is simply a mislabelled component of the bottom pressure torque. If this is the case, then the topographic interactions that shape the simulated gyre are unrealistic and localized to steps in the model bathymetry (see Figure 3.13k). This would suggest that the partial cell representation of the sea floor is not creating a sufficiently smooth bathymetry for the gyre.

It is also possible that other model forces contain spurious contributions that have not been uncovered yet. Additional spurious terms may cancel the spurious effects found in Chapter 3 and the acceleration of the gyre would be uncorrupted. Confirming this would require a studying of the other model forces at a similar level of detail to Chapter 3. In the case of the Weddell Gyre, an equal and opposite spurious force would have to at least partially reside in the wind stress. Presently, it is unclear how a prescribed atmospheric wind stress can balance a spurious force that is so closely tied to steps in the model bathymetry. However, problematic vertical diffusion of the surface stress in the ocean interior may be a source of spurious contributions.

The final possibility is the most alarming. The spurious force has no physical interpretation and is not cancelled by other spurious contributions. In this case, the Weddell Gyre and other gyre circulations are determined by numerical errors that are uncontrollable and uninterpretable. If this is the case, then how robust is the strength and structure of the simulated gyre?

All three of these possibilities could be tested by studying the vorticity budgets of simple configurations where certain model forces have strong integral constraints. This testing method is used in Arakawa and Suarez (1983) and Song and Wright

(1998). For example, consider a variable bathymetry with a zero gradient along the domain edge. In this case the domain area integral of the bottom pressure torque should equal zero. This is a consequence of Stokes' theorem,

$$\iint_A \boldsymbol{\nabla} \times (P_b \boldsymbol{\nabla} H) \cdot \hat{\mathbf{n}} dA = \oint_\Gamma (P_b \boldsymbol{\nabla} H) \cdot \mathbf{dl} = 0, \tag{5.1}$$

where P_b is the bottom pressure, H is the sea floor depth, A is the domain area, and Γ is the domain perimeter. If the integrated bottom pressure torque is non-zero on the C-grid, then this may indicate an additional spurious term in the model's calculation of bottom pressure. Furthermore, any spurious component of the Coriolis force that vanishes when integrated in the same way as Equation 5.1 may be related to bottom pressure torques. By devising a series of experiments where specific forces should theoretically vanish upon integration, we could develop our understanding of the spurious force found in chapter 3 and identify additional limitations of the C-grid.

Refining horizontal and vertical resolution may not resolve the problems found in Chapter 3. When using a z-coordinate model, there will always be the same surface area of vertical sidewall, no matter what the grid spacing is. Diagnosing simulations where the horizontal resolution is varied may prove to be helpful. It is important to remember however that the circulation itself will also respond to the change in resolution which may modify the results. The ideal experiment would involve calculating and decomposing the spurious force acting on a fixed circulation at various resolutions.

The idealized model used in Chapter 2 is susceptible to the spurious forces in Chapter 3. This raises a natural question, how do the findings of Chapter 3 influence our interpretation of the idealized simulations from Chapter 2? Both chapters agree that topographic interaction (spurious or otherwise) is central to the dynamics of the Weddell Gyre. The thermal wind component of the idealized gyre circulation is determined by a density structure (Figures 2.11 and 2.12) which resembles observations (Figures 2.1). In Chapter 2, we also argue that the intensification of the bottom flow is driven by baroclinic eddies which emerge from the same density structure. Based on this we believe that the idealized simulations offer a qualitative

description of the real Weddell Gyre. However, the significance of spurious forces in the idealized model would need to be assessed before making more quantitative conclusions about the Weddell Gyre. For example, determining the vorticity budget or eddy energy budget of the idealized simulations would require the diagnostics from Chapter 3 to assess what exact processes are taking place at the sea floor.

5.2.4 Interannual ventilation processes

In Chapter 4, we found conclusive evidence that Stommel's demon (Stommel, 1979) operates on a seasonal timescale in the Southern Ocean. In Figure 4.2a, we can also identify another temporal pattern of ventilation. In general, the ventilated volume decreases with trajectory age but there is notable interannual variability. In some cases, the ventilated volume increases with trajectory age. This suggests that the Southern Ocean interior is more receptive to surface forcing in specific years of its history.

In the North Atlantic, MacGilchrist et al. (2021) found that ocean ventilation can be mediated by year-to-year variations in the late winter mixed layer depth. MacGilchrist et al. (2021) measured this by launching backwards-in-time trajectories in every year between 1976 and 2015. This can be considered as an ensemble of backwards-in-time trajectory experiments. The age distribution of the ensemble average describes a baseline distribution of ventilation timing for the region. By comparing the age distribution of a specific year to the baseline, you can more clearly identify the interannual variability of ventilation. The methodology of MacGilchrist et al. (2021) could also be applied to the Southern Ocean. The interannual variability of ventilation may be correlated with the mean mixed layer depth or other variables such as the ACC transport, Weddell Gyre transport, or sea ice extent.

5.3 Concluding remarks

Throughout the course of this thesis, we have started to unravel the complexities of the Weddell Gyre using a wide variety of methods. An idealized model exposed the gyre's sensitivity to mesoscale eddies and highlighted potential difficulties simulating

the gyre at eddy-permitting resolutions. A vorticity budget of the Weddell Gyre revealed the leading order force balances of a simulated Weddell Gyre and exposed a major limitation of C-grid models. Our backwards-in-time trajectory experiment demonstrated the importance of the subpolar gyres in the Southern Ocean as a bridge between the Antarctic shelf and the ACC. The experiment also revealed the highly seasonal nature of ventilation in the wider Southern Ocean alongside clear spatial patterns of ventilation. Focused observational studies of the Weddell Gyre are essential to test the findings of this thesis and assess the accuracy of ocean models in this region. Increasing the deployment of ARGO floats across the Weddell Gyre or continuing development of under-ice altimetry may help constrain the true gyre transport. Furthermore, continuous monitoring of the circulation immediately above the submarine ridge or Antarctic shelf may reveal the important sea floor interactions which shape the Weddell Gyre circulation.

Appendices

A

Deriving the Vorticity Equation and Discretization Details.

Contents

A.1 Deriving the depth-integrated vorticity equation

Here we derive the depth-integrated vorticity equation (Equation 3.2) including the omitted contributions from surface undulations and atmospheric pressure torques. We start from the vector invariant form of the momentum equation,

$$\frac{\partial \mathbf{u_h}}{\partial t} = -\left[(\nabla \times \mathbf{u}) \times \mathbf{u} + \frac{1}{2}\nabla(\mathbf{u}\cdot\mathbf{u})\right]_h - f\left(\hat{\mathbf{k}} \times \mathbf{u}\right)_h - \frac{1}{\rho_0}\nabla_h P + \mathcal{F}^{\mathbf{u}} + \mathcal{D}^{\mathbf{u}}, \quad \text{(A.1)}$$

which has already been introduced in Section 3.2.1. To derive the depth-integrated vorticity equation, we must first depth-integrate the equation and then calculate the vertical component of the curl. In this appendix, we consider how each term in Equation A.1 is transformed by this operation.

When depth-integrating the time derivative term in Equation A.1, we must respect the time dependency of the free surface, η. We therefore use the Leibniz integration rule,

$$\nabla \times \left(\int_{-H(x,y)}^{\eta(x,y,t)} \frac{\partial \mathbf{u_h}}{\partial t}\, dz \right) \cdot \hat{\mathbf{k}} = \frac{\partial}{\partial t} \left(\nabla \times \mathbf{U} \right) \cdot \hat{\mathbf{k}} - \nabla \times \left(\mathbf{u}_h(z=\eta) \frac{\partial \eta}{\partial t} \right) \cdot \hat{\mathbf{k}}, \quad \text{(A.2)}$$

where the second term on the right hand side of Equation A.2 is the contribution from free surface undulations.

The non-linear term in Equation A.1 can be rewritten as,

$$\Big[(\nabla \times \mathbf{u}) \times \mathbf{u} + \frac{1}{2} \nabla \left(\mathbf{u} \cdot \mathbf{u} \right) \Big]_h = \frac{1}{2} \nabla_h (\mathbf{u}_h \cdot \mathbf{u}_h) + \zeta \left(\hat{\mathbf{k}} \times \mathbf{u} \right)_h + w \frac{\partial \mathbf{u}_h}{\partial z}. \quad \text{(A.3)}$$

The non-linear term emerges as the advection term in the depth-integrated vorticity equation and we note that,

$$\nabla \times \left[\int_{-H}^{\eta} \zeta \left(\hat{\mathbf{k}} \times \mathbf{u} \right)_h \, dz \right] \cdot \hat{\mathbf{k}} = \nabla_h \cdot \left(\int_{-H}^{\eta} \zeta \mathbf{u}_h \, dz \right). \quad \text{(A.4)}$$

Similarly the curl of the depth-integrated Coriolis acceleration is the planetary vorticity term,

$$\nabla \times \left[\int_{-H}^{\eta} -f \left(\hat{\mathbf{k}} \times \mathbf{u} \right)_h \, dz \right] \cdot \hat{\mathbf{k}} = -\nabla_h \cdot (f \mathbf{U}). \quad \text{(A.5)}$$

When depth-integrating the pressure gradient in Equation A.1, we must respect the x and y dependency of the sea floor and the free surface. We therefore use the Leibniz integration rule,

$$\nabla \times \left(\int_{-H(x,y)}^{\eta(x,y,t)} -\frac{1}{\rho_0} \nabla_h P \, dz \right) \cdot \hat{\mathbf{k}} = \frac{1}{\rho_0} \left(\nabla P_b \times \nabla H \right) \cdot \hat{\mathbf{k}} + \frac{1}{\rho_0} \left(\nabla P_a \times \nabla \eta \right) \cdot \hat{\mathbf{k}}, \quad \text{(A.6)}$$

where P_a is the atmospheric pressure at the free surface. The second term on the right hand side of Equation A.6 is the atmospheric pressure torque.

The surface forcing term, $\mathcal{F}^{\mathbf{u}}$, in Equation A.1 emerges as the difference between the curl of the top and bottom stresses,

$$\nabla \times \left(\int_{-H}^{\eta} \mathcal{F}^{\mathbf{u}} \, dz \right) \cdot \hat{\mathbf{k}} = \frac{1}{\rho_0} \left(\nabla \times \boldsymbol{\tau}_{\text{top}} \right) \cdot \hat{\mathbf{k}} - \frac{1}{\rho_0} \left(\nabla \times \boldsymbol{\tau}_{\text{bot}} \right) \cdot \hat{\mathbf{k}}, \tag{A.7}$$

and the diffusion term is denoted as $\mathcal{D}^{\zeta}$,

$$\nabla \times \left(\int_{-H}^{\eta} \mathcal{D}^{\mathbf{u}} \, dz \right) \cdot \hat{\mathbf{k}} = \mathcal{D}^{\zeta}. \tag{A.8}$$

By combining all the equations above we can derive the depth-integrated vorticity equation,

$$\begin{aligned} \frac{\partial}{\partial t} \left(\nabla \times \mathbf{U} \right) \cdot \hat{\mathbf{k}} = \; & - \; \nabla_h \cdot (f \mathbf{U}) + \frac{1}{\rho_0} \left(\nabla P_b \times \nabla H \right) \cdot \hat{\mathbf{k}} + \frac{1}{\rho_0} \left(\nabla \times \boldsymbol{\tau}_{\text{top}} \right) \cdot \hat{\mathbf{k}} \\ & - \; \frac{1}{\rho_0} \left(\nabla \times \boldsymbol{\tau}_{\text{bot}} \right) \cdot \hat{\mathbf{k}} + \mathcal{D}^{\zeta} \\ & - \; \nabla_h \cdot \left(\int_{-H(x,y)}^{\eta(x,y,t)} \zeta \mathbf{u} \, dz \right) \\ & - \; \left[\nabla \times \left(\int_{-H(x,y)}^{\eta(x,y,t)} \frac{1}{2} \nabla_h \left(\mathbf{u}_h^2 \right) + w \frac{\partial \mathbf{u}_h}{\partial z} \right) \right] \cdot \hat{\mathbf{k}} \\ & + \; \underbrace{\frac{1}{\rho_0} \left(\nabla P_a \times \nabla \eta \right) \cdot \hat{\mathbf{k}}}_{\text{Atmospheric pressure torque}} \\ & + \; \underbrace{\left[\nabla \times \left(\mathbf{u}_h (z = \eta) \frac{\partial \eta}{\partial t} \right) \right] \cdot \hat{\mathbf{k}}}_{\text{Surface undulations}} . \end{aligned} \tag{A.9}$$

A.2 Explicit forms of the Coriolis schemes

Here we explicitly state the forms of the discrete Coriolis acceleration in the ENE, ENS, and EEN vorticity schemes for a z-coordinate system. In the ENE vorticity scheme the x and y components of the Coriolis acceleration are:

$$
\begin{aligned}
\mathrm{COR}^{x}_{i,j,k} &= \frac{1}{4e^{1u}_{i,j}}\Big[f_{i,j-1}\left(\left(ve^{1v}\right)_{i,j-1,k}+\left(ve^{1v}\right)_{i+1,j-1,k}\right)\\
&\quad +f_{i,j}\left(\left(ve^{1v}\right)_{i,j,k}+\left(ve^{1v}\right)_{i+1,j,k}\right)\Big],\\
\mathrm{COR}^{y}_{i,j,k} &= \frac{1}{4e^{2v}_{i,j}}\Big[f_{i-1,j}\left(\left(ue^{2u}\right)_{i-1,j,k}+\left(ue^{2u}\right)_{i-1,j+1,k}\right)\\
&\quad +f_{i,j}\left(\left(ue^{2u}\right)_{i,j,k}+\left(ue^{2u}\right)_{i,j+1,k}\right)\Big].
\end{aligned}
\tag{A.10}
$$

In the ENS vorticity scheme the x and y components of the Coriolis acceleration are:

$$
\begin{aligned}
\mathrm{COR}^{x}_{i,j,k} &= \frac{1}{8e^{1u}_{i,j}}\Big[\left(ve^{1v}\right)_{i,j-1,k}+\left(ve^{1v}\right)_{i+1,j-1,k}\\
&\quad +\left(ve^{1v}\right)_{i,j,k}+\left(ve^{1v}\right)_{i+1,j,k}\Big]\left[f_{i,j-1}+f_{i,j}\right],\\
\mathrm{COR}^{y}_{i,j,k} &= \frac{-1}{8e^{2v}_{i,j}}\Big[\left(ue^{2u}\right)_{i-1,j-1,k}+\left(ue^{2u}\right)_{i-1,j+1,k}\\
&\quad +\left(ue^{2u}\right)_{i,j,k}+\left(ue^{2u}\right)_{i,j+1,k}\Big]\left[f_{i-1,j}+f_{i,j}\right].
\end{aligned}
\tag{A.11}
$$

We note that each term in the ENE and ENS forms can be written in the general form of Equations 3.8 and 3.9 as $ve^{1v}=\tilde{V}/e^{3v}$ and $ue^{2u}=\tilde{U}/e^{3u}$. In the ENE and ENS cases $e^{3}_{k}(\mathbf{b}_n)=e^{3}_{k}(\mathbf{c}_n)$ in Equations 3.8 and 3.9.

In the EEN vorticity scheme, the x and y components of the Coriolis acceleration are:

$$
\begin{aligned}
\mathrm{COR}^{x}_{i,j,k} &= \frac{1}{12e^{1u}_{i,j}}\Big[F^{NE}_{i,j,k}\left(ve^{3v}e^{1v}\right)_{i,j,k}+F^{NW}_{i+1,j,k}\left(ve^{3v}e^{1v}\right)_{i+1,j,k}\\
&\quad +F^{SE}_{i,j,k}\left(ve^{3v}e^{1v}\right)_{i,j-1,k}+F^{SW}_{i+1,j,k}\left(ve^{3v}e^{1v}\right)_{i+1,j-1,k}\Big],\\
\mathrm{COR}^{y}_{i,j,k} &= \frac{-1}{12e^{2v}_{i,j}}\Big[F^{NE}_{i,j,k}\left(ue^{3u}e^{2u}\right)_{i,j,k}+F^{NW}_{i,j,k}\left(ue^{3u}e^{2u}\right)_{i-1,j,k}\\
&\quad +F^{SE}_{i,j+1,k}\left(ue^{3u}e^{2u}\right)_{i,j+1,k}+F^{SW}_{i,j+1,k}\left(ue^{3u}e^{2u}\right)_{i-1,j+1,k}\Big],
\end{aligned}
\tag{A.12}
$$

where F^{NE}, F^{NW}, F^{SE}, and F^{SW} are thickness-weighted triads of the Coriolis parameter:

$$F^{NE}_{i,j,k} = \left(\tilde{f}_{i,j,k} + \tilde{f}_{i-1,j,k} + \tilde{f}_{i,j-1,k}\right), \tag{A.13}$$

$$F^{NW}_{i,j,k} = \left(\tilde{f}_{i,j,k} + \tilde{f}_{i-1,j,k} + \tilde{f}_{i-1,j-1,k}\right), \tag{A.14}$$

$$F^{SE}_{i,j,k} = \left(\tilde{f}_{i,j,k} + \tilde{f}_{i,j-1,k} + \tilde{f}_{i-1,j-1,k}\right), \tag{A.15}$$

$$F^{SW}_{i,j,k} = \left(\tilde{f}_{i-1,j,k} + \tilde{f}_{i,j-1,k} + \tilde{f}_{i-1,j-1,k}\right), \tag{A.16}$$

where $\tilde{f} = f/e^{3f}$ using the EEN definition of e^{3f} shown in Equation 3.13.

To calculate the planetary vorticity diagnostic we take the curl of the depth-integrated Coriolis acceleration using Equations 3.15 and 3.22. In general the resulting equation of the vorticity diagnostic is very difficult to interpret. We only present the form of the planetary vorticity diagnostic for the EEN scheme on a grid with no partial cells or model level steps as it is used to derive the numerical beta effect in Section 3.3.5:

$$\begin{aligned}
\mathrm{PVO}_{i,j} = \frac{1}{12\left(e^{1f}e^{2f}\right)_{i,j}}\Bigg[& -f^{NE}_{i,j+1}\left(Ve^{1v}\right)_{i,j+1} - f^{NW}_{i+1,j+1}\left(Ve^{1v}\right)_{i+1,j+1} \\
& + f^{SE}_{i,j}\left(Ve^{1v}\right)_{i,j-1} + f^{SW}_{i+1,j}\left(Ve^{1v}\right)_{i+1,j-1} \\
& - f^{SE}_{i+1,j+1}\left(Ue^{2u}\right)_{i+1,j+1} - f^{NE}_{i+1,j}\left(Ue^{2u}\right)_{i+1,j} \\
& + f^{SW}_{i,j+1}\left(Ue^{2u}\right)_{i-1,j+1} + f^{NW}_{i,j}\left(Ue^{2u}\right)_{i-1,j} \\
& - \left(f_{i,j+1} - f_{i,j-1}\right)\left(\left(Ve^{1v}\right)_{i+1,j} + \left(Ve^{1v}\right)_{i,j}\right) \\
& - \left(f_{i+1,j} - f_{i-1,j}\right)\left(\left(Ue^{2u}\right)_{i,j+1} + \left(Ue^{2u}\right)_{i,j}\right)\Bigg].
\end{aligned} \tag{A.17}$$

A.3 Alternative vorticity schemes in the double gyre model

In this section we present various integrations of the SLOPED double gyre configuration using different vorticity schemes: EEN, ENS, and ENE. All other aspects of the experiment are as described in Section 3.4.1. The results are shown in Figure A.1. The vorticity budget is qualitatively similar between the three cases as well as the decomposition of the planetary vorticity diagnostic. It should be noted

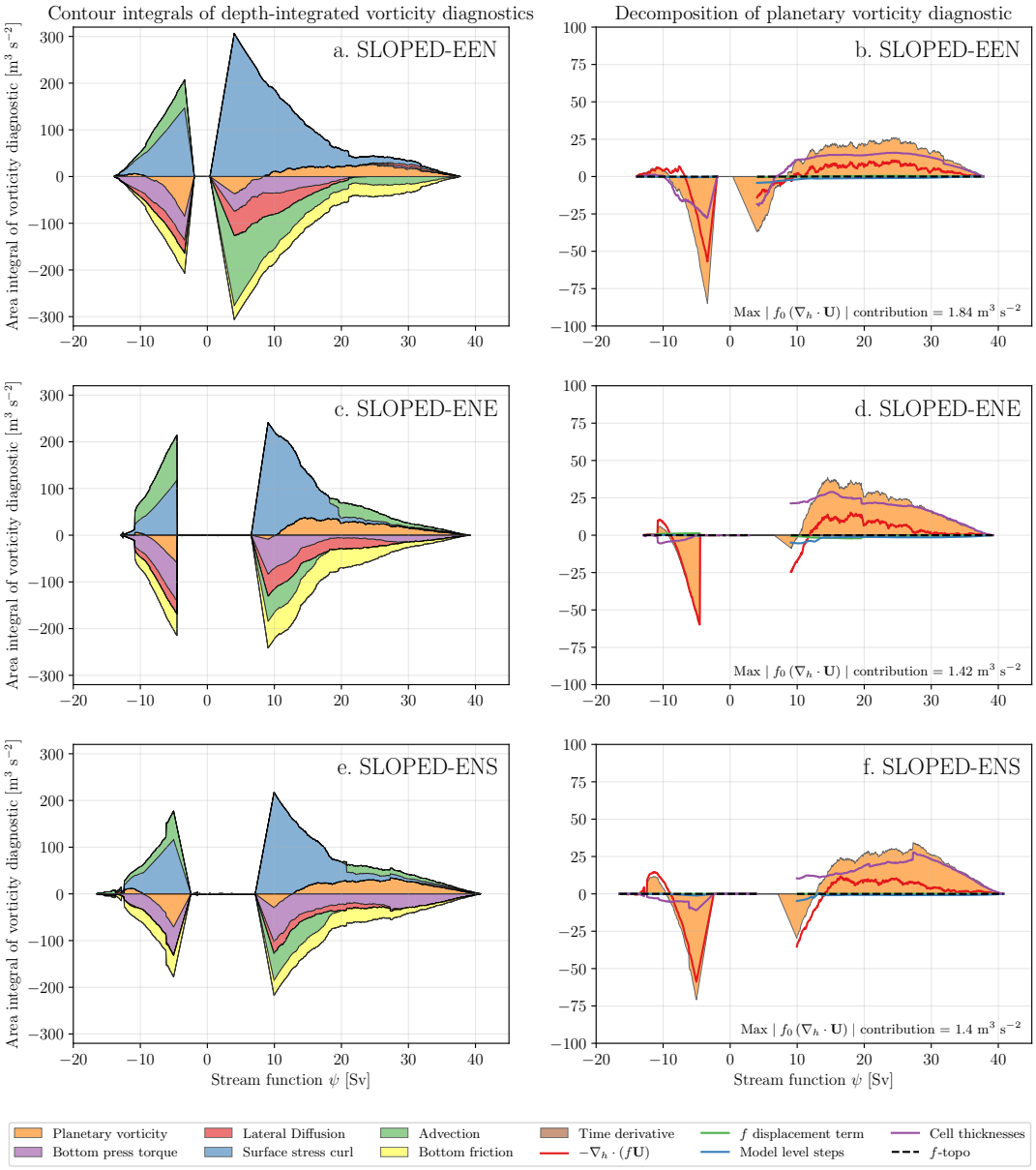

Figure A.1: Stacked area plots showing the integrals of depth-integrated vorticity diagnostics for the SLOPED configuration (time-averaged) using the EEN, ENE, and ENS vorticity schemes. Positive values correspond to a force that spins the subtropical ($\psi > 0$) or subpolar ($\psi < 0$) gyre up. A decomposition of the planetary vorticity diagnostic integrals are given on the right (b,d,f).

that the circulations do differ as the transports vary and the separation points of the western boundary currents change.

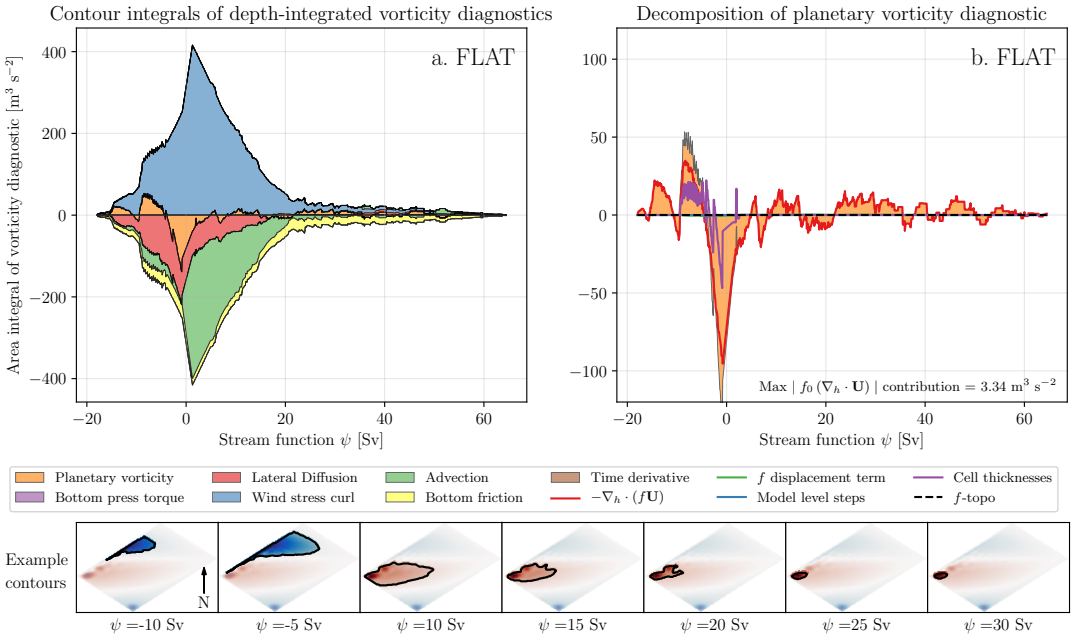

Figure A.2: Stacked area plots showing the integrals of depth-integrated vorticity diagnostics (time-averaged) for the FLAT configuration without using interpolated fields. Positive values correspond to a force that spins the subtropical ($\psi > 0$) or subpolar ($\psi < 0$) gyre up. (b) Shows the area integrals of the planetary vorticity diagnostic and its components. The vorticity budget and decomposition are qualitatively similar to that shown in Figure 3.9.

A.4 Contour integration without interpolation

The interpolation of vorticity diagnostic fields and the streamfunction is discussed in Section 3.4.2. Linear interpolation is used to minimise the difference between the enclosed area of the true streamline and the total area of the interior F cells. In this section we present results that use uninterpolated fields from the FLAT double gyre configuration. The results are shown in Figure A.2 and are qualitatively similar to the interpolated results shown in Figure 3.9. This example is selected to demonstrate both the qualitative similarity to interpolated results but also the reduced coherence that comes from using non-interpolated data. The non-interpolated results from the Weddell Gyre are in fact more coherent than the results shown in Figure A.2.

Data and Code Availability

Every effort has been made to ensure the reader has access to all relevant code and data for the thesis. In Chapter 2, the input files for the idealized model integrations are archived on Zenodo (Styles et al., 2023b). The idealized configuration, designed for NEMO release 4.0.1, is available on Zenodo (Styles et al., 2023c). The software used to analyse the model outputs is also archived on Zenodo (Styles et al., 2023a).

In Chapter 3, the software used to calculate, integrate, and plot the vorticity budget is available from https://github.com/afstyles/VorticityContourAnalysisForNemo/tree/917f337/. The model integrations can be found on Zenodo (Styles et al., 2021). The global configuration used in this chapter uses NEMO version 4.0.4 with the following merged branches:

- branches/UKMO/NEMO_4.0.4_mirror @ 14075,
- branches/UKMO/NEMO_4.0.4_GO8_package @ 14474,
- branches/UKMO/NEMO_4.0.4_GO6_mixing @ 14099,
- branches/UKMO/NEMO_4.0.4_old_tidal_mixing @ 14096,
- branches/UKMO/NEMO_4.0.4_momentum_trends @ 15194.

The double gyre configuration uses NEMO version 4.0.1 and any modified source code is archived on Zenodo (Styles et al., 2021). The versions of NEMO and the mentioned branches can be found at https://forge.ipsl.jussieu.fr/nemo/browser/NEMO/.

In Chapter 4, the data for the trajectories used in this study are archived on Zenodo (Styles et al., 2023f) alongside the calculated statistics. The software used to analyze the model outputs is also archived on Zenodo (Styles et al., 2023e).

References

Abernathey, R. P., Cerovecki, I., Holland, P. R., Newsom, E., Mazloff, M., & Talley, L. D. (2016). Water-mass transformation by sea ice in the upper branch of the Southern Ocean overturning. *Nature Geoscience*, *9*(8), 596–601. https://doi.org/10.1038/ngeo2749

Abernathey, R. P., & Ferreira, D. (2015). Southern Ocean isopycnal mixing and ventilation changes driven by winds. *Geophysical Research Letters*, *42*(23), 10, 357–10, 365. https://doi.org/10.1002/2015GL066238

Abernathey, R. P., Marshall, J., & Ferreira, D. (2011). The dependence of southern ocean meridional overturning on wind stress. *Journal of Physical Oceanography*, *41*(12), 2261–2278. https://doi.org/10.1175/JPO-D-11-023.1

Adcock, S. T., & Marshall, D. P. (2000). Interactions between Geostrophic Eddies and the Mean Circulation over Large-Scale Bottom Topography. *Journal of Physical Oceanography*, *30*(12), 3223–3238. https://doi.org/10.1175/1520-0485(2000)030<3223:IBGEAT>2.0.CO;2

Adcroft, A., Anderson, W., Balaji, V., Blanton, C., Bushuk, M., Dufour, C. O., Dunne, J. P., Griffies, S. M., Hallberg, R., Harrison, M. J., Held, I. M., Jansen, M. F., John, J. G., Krasting, J. P., Langenhorst, A. R., Legg, S., Liang, Z., McHugh, C., Radhakrishnan, A., … Zhang, R. (2019). The GFDL Global Ocean and Sea Ice Model OM4.0: Model Description and Simulation Features. *Journal of Advances in Modeling Earth Systems*, *11*(10), 3167–3211. https://doi.org/10.1029/2019MS001726

Adcroft, A., & Marshall, D. (1998). How slippery are piecewise-constant coastlines in numerical ocean models? *50*(1), 95. https://doi.org/10.3402/tellusa.v50i1.14514

Aldama-Campino, A., Döös, K., Kjellsson, J., & Jönsson, B. (2020). TRACMASS: Formal release of version 7.0. https://doi.org/10.5281/zenodo.4337926

Amante, C., & Eakins, B. W. (2009). ETOPO1 arc-minute global relief model: Procedures, data sources and analysis. *NOAA Technical Memorandum NESDIS NGDC-24*.

Arakawa, A., & Lamb, V. R. (1981). A potential enstrophy and energy conserving scheme for the shallow water equations. *Monthly Weather Review*, *109*(1), 18–36. https://doi.org/10.1175/1520-0493(1981)109<0018:APEAEC>2.0.CO;2

Arakawa, A., & Lamb, V. R. (1977). Computational design of the basic dynamical processes of the UCLA general circulation model. *General circulation models of the atmosphere*, *17*(Supplement C), 173–265.

Arakawa, A., & Suarez, M. J. (1983). Vertical Differencing of the Primitive Equations in Sigma Coordinates. *Monthly Weather Review*, *111*(1), 34–45. https://doi.org/10.1175/1520-0493(1983)111<0034:VDOTPE>2.0.CO;2

Argo. (2020). Argo float data and metadata from Global Data Assembly Centre (Argo GDAC). https://doi.org/10.17882/42182

Armitage, T. W. K., Bacon, S., Ridout, A. L., Thomas, S. F., Aksenov, Y., & Wingham, D. J. (2016). Arctic sea surface height variability and change from satellite radar altimetry and GRACE, 2003–2014. *Journal of Geophysical Research: Oceans*, *121*(6), 4303–4322. https://doi.org/10.1002/2015JC011579

Armitage, T. W. K., Kwok, R., Thompson, A. F., & Cunningham, G. (2018). Dynamic Topography and Sea Level Anomalies of the Southern Ocean: Variability and Teleconnections. *Journal of Geophysical Research: Oceans*, *123*(1), 613–630. https://doi.org/10.1002/2017JC013534

Arndt, J. E., Schenke, H. W., Jakobsson, M., Nitsche, F. O., Buys, G., Goleby, B., Rebesco, M., Bohoyo, F., Hong, J., Black, J., Greku, R., Udintsev, G., Barrios, F., Reynoso-Peralta, W., Taisei, M., & Wigley, R. (2013). The International Bathymetric Chart of the Southern Ocean (IBCSO) Version 1.0-A new bathymetric compilation covering circum-Antarctic waters. *Geophysical Research Letters*, *40*(12), 3111–3117. https://doi.org/10.1002/grl.50413

Barnier, B., Madec, G., Penduff, T., Molines, J. M., Treguier, A. M., Le Sommer, J., Beckmann, A., Biastoch, A., Böning, C., Dengg, J., Derval, C., Durand, E., Gulev, S., Remy, E., Talandier, C., Theetten, S., Maltrud, M., McClean, J., & De Cuevas, B. (2006). Impact of partial steps and momentum advection schemes in a global ocean circulation model at eddy-permitting resolution. *Ocean Dynamics*, *56*(5-6), 543–567. https://doi.org/10.1007/s10236-006-0082-1

Bell, M. J. (1999). Vortex stretching and bottom torques in the Bryan-Cox ocean circulation model. *Journal of Geophysical Research: Oceans*. https://doi.org/10.1029/1999jc900064

Blanke, B., & Raynaud, S. (1997). Kinematics of the Pacific Equatorial Undercurrent: An Eulerian and Lagrangian Approach from GCM Results. *Journal of Physical Oceanography*, *27*(6), 1038–1053. https://doi.org/10.1175/1520-0485(1997)027<1038:KOTPEU>2.0.CO;2

Bleck, R. (2002). An oceanic general circulation model framed in hybrid isopycnic-Cartesian coordinates. *Ocean Modelling*, *4*(1), 55–88. https://doi.org/10.1016/S1463-5003(01)00012-9

Blumsack, S. L., & Gierasch, P. J. (1972). Mars: The Effects of Topography on Baroclinic Instability. *Journal of the Atmospheric Sciences*, *29*(6), 1081–1089. https://doi.org/10.1175/1520-0469(1972)029<1081:MTEOTO>2.0.CO;2

Bopp, L., Le Quéré, C., Heimann, M., Manning, A. C., & Monfray, P. (2002). Climate-induced oceanic oxygen fluxes: Implications for the contemporary carbon budget. *Global Biogeochemical Cycles*, *16*(2), 6-1-6–13. https://doi.org/10.1029/2001GB001445

Bougeault, P., & Lacarrere, P. (1989). Parameterization of Orography-Induced Turbulence in a Mesobeta–Scale Model. *Monthly Weather Review*, *117*(8), 1872–1890. https://doi.org/10.1175/1520-0493(1989)117<1872:POOITI>2.0.CO;2

Bouillon, S., Morales Maqueda, M. Á., Legat, V., & Fichefet, T. (2009). An elastic–viscous–plastic sea ice model formulated on Arakawa B and C grids. *Ocean Modelling*, *27*(3), 174–184. https://doi.org/10.1016/j.ocemod.2009.01.004

Bretherton, F. P., & Haidvogel, D. B. (1976). Two-dimensional turbulence above topography. *Journal of Fluid Mechanics*, *78*(1), 129–154. https://doi.org/10.1017/S002211207600236X

Buongiorno Nardelli, B., Guinehut, S., Verbrugge, N., Cotroneo, Y., Zambianchi, E., & Iudicone, D. (2017). Southern Ocean Mixed-Layer Seasonal and Interannual Variations From Combined Satellite and In Situ Data. *Journal of Geophysical Research: Oceans*, *122*(12), 10042–10060. https://doi.org/10.1002/2017JC013314

Buongiorno Nardelli, B., Mulet, S., & Iudicone, D. (2018). Three-Dimensional Ageostrophic Motion and Water Mass Subduction in the Southern Ocean. *Journal of Geophysical Research: Oceans*, *123*(2), 1533–1562. https://doi.org/10.1002/2017JC013316

Canadell, J., Monteiro, P., Costa, M., Cotrim da Cunha, L., Cox, P., Eliseev, A., Henson, S., Ishii, M., Jaccard, S., Koven, C., Lohila, A., Patra, P., Piao, S., Rogelj, J., Syampungani, S., Zaehle, S., & Zickfeld, K. (2021). Global carbon and other biogeochemical cycles and feedbacks. In V. Masson-Delmotte, P. Zhai, A. Pirani, S. Connors, C. Péan, S. Berger, N. Caud, Y. Chen, L. Goldfarb, M. Gomis, M. Huang, K. Leitzell, E. Lonnoy, J. Matthews, T. Maycock, T. Waterfield, O. Yelekçi, R. Yu, & B. Zhou (Eds.), *Climate change 2021: The physical science basis. Contribution of working group I to the sixth assessment report of the intergovernmental panel on climate change* (pp. 673–816). Cambridge University Press. https://doi.org/10.1017/9781009157896.007

Cane, M. A., Kamenkovich, V. M., & Krupitsky, A. (1998). On the utility and disutility of JEBAR. *Journal of Physical Oceanography*. https://doi.org/10.1175/1520-0485(1998)028<0519:OTUADO>2.0.CO;2

Cazenave, A., Dieng, H.-B., Meyssignac, B., von Schuckmann, K., Decharme, B., & Berthier, E. (2014). The rate of sea-level rise. *Nature Climate Change*, *4*(5), 358–361. https://doi.org/10.1038/nclimate2159

Cheng, L., von Schuckmann, K., Abraham, J. P., Trenberth, K. E., Mann, M. E., Zanna, L., England, M. H., Zika, J. D., Fasullo, J. T., Yu, Y., Pan, Y., Zhu, J., Newsom, E. R., Bronselaer, B., & Lin, X. (2022). Past and future ocean warming. *Nature Reviews Earth & Environment*, *3*(11), 776–794. https://doi.org/10.1038/s43017-022-00345-1

Chidichimo, M. P., Donohue, K. A., Watts, D. R., & Tracey, K. L. (2014). Baroclinic Transport Time Series of the Antarctic Circumpolar Current Measured in Drake Passage. *Journal of Physical Oceanography*, *44*(7), 1829–1853. https://doi.org/10.1175/JPO-D-13-071.1

Cisewski, B., Strass, V. H., & Leach, H. (2011). Circulation and transport of water masses in the Lazarev Sea, Antarctica, during summer and winter 2006. *Deep Sea Research Part I: Oceanographic Research Papers*, *58*(2), 186–199. https://doi.org/10.1016/j.dsr.2010.12.001

Danabasoglu, G., McWilliams, J. C., & Gent, P. R. (1994). The Role of Mesoscale Tracer Transports in the Global Ocean Circulation. *Science*, *264*(5162), 1123–1126. https://doi.org/10.1126/science.264.5162.1123

de Boyer Montégut, C., Madec, G., Fischer, A. S., Lazar, A., & Iudicone, D. (2004). Mixed layer depth over the global ocean: An examination of profile data and a profile-based climatology. *Journal of Geophysical Research: Oceans*, *109*(C12). https://doi.org/10.1029/2004JC002378

Deacon, G. E. R. (1979). The Weddell gyre. *Deep Sea Research Part A. Oceanographic Research Papers*, *26*(9), 981–995. https://doi.org/10.1016/0198-0149(79)90044-X

Desbruyères, D. G., Mercier, H., Maze, G., & Daniault, N. (2019). Surface predictor of overturning circulation and heat content change in the subpolar North Atlantic. *Ocean Science*, *15*(3), 809–817. https://doi.org/10.5194/os-15-809-2019

Dong, S., Sprintall, J., Gille, S. T., & Talley, L. (2008). Southern Ocean mixed-layer depth from Argo float profiles. *Journal of Geophysical Research: Oceans*, *113*(C6). https://doi.org/10.1029/2006JC004051

Donohue, K. A., Tracey, K. L., Watts, D. R., Chidichimo, M. P., & Chereskin, T. K. (2016). Mean Antarctic Circumpolar Current transport measured in Drake Passage. *Geophysical Research Letters*, *43*(22), 11, 760–11, 767. https://doi.org/10.1002/2016GL070319

Döös, K., Jönsson, B., & Kjellsson, J. (2017). Evaluation of oceanic and atmospheric trajectory schemes in the TRACMASS trajectory model v6.0. *Geoscientific Model Development*, *10*(4), 1733–1749. https://doi.org/10.5194/gmd-10-1733-2017

Drijfhout, S. S., Marshall, D. P., & Dijkstra, H. A. (2013). Conceptual Models of the Wind-Driven and Thermohaline Circulation. In G. Siedler, S. M. Griffies, J. Gould, & J. A. Church (Eds.), *Ocean Circulation and Climate* (pp. 257–282, Vol. 103). Academic Press. https://doi.org/10.1016/B978-0-12-391851-2.00011-8

Dupont, F., Straub, D. N., & Lin, C. A. (2003). Influence of a step-like coastline on the basin scale vorticity budget of mid-latitude gyre models. *Tellus A: Dynamic Meteorology and Oceanography*, *55*(3), 255–272. https://doi.org/10.3402/tellusa.v55i3.12094

Dussin, R., Barnier, B., Brodeau, L., & Molines, J. M. (2016). *Drakkar forcing set DFS5* (tech. rep.). Laboratoire de glaciologie et géophysique de l'environnement.

Eady, E. T. (1949). Long Waves and Cyclone Waves. *Tellus*, *1*(3), 33–52. https://doi.org/10.3402/tellusa.v1i3.8507

Fahrbach, E., Knoche, M., & Rohardt, G. (1991). An estimate of water mass transformation in the southern Weddell Sea. *Marine Chemistry*, *35*(1-4), 25–44. https://doi.org/10.1016/S0304-4203(09)90006-8

Fox-Kemper, B., Hewitt, H., Xiao, C., Aðalgeirsdóttir, G., Drijfhout, S., Edwards, T., Golledge, N., Hemer, M., Kopp, R., Krinner, G., Mix, A., Notz, D., Nowicki, S., Nurhati, I., Ruiz, L., Sallée, J.-B., Slangen, A., & Yu, Y. (2021). Ocean, cryosphere and sea level change. In V. Masson-Delmotte, P. Zhai, A. Pirani, S. Connors, C. Péan, S. Berger, N. Caud, Y. Chen, L. Goldfarb, M. Gomis, M. Huang, K. Leitzell, E. Lonnoy, J. Matthews, T. Maycock, T. Waterfield, O. Yelekçi, R. Yu, & B. Zhou (Eds.), *Climate change 2021: The physical science basis. Contribution of working group I to the sixth assessment report of the intergovernmental panel on climate change* (pp. 1211–1362). Cambridge University Press. https://doi.org/10.1017/9781009157896.011

Fox-Kemper, B. (2018). Notions for the Motions of the Oceans. In E. P. Chassignet, A. Pascual, J. Tintoré, & J. Verron (Eds.), *New Frontiers in Operational Oceanography*. GODAE OceanView. https://doi.org/10.17125/gov2018.ch02

Franco, B. C., Mata, M. M., Piola, A. R., & Garcia, C. A. E. (2007). Northwestern Weddell Sea deep outflow into the Scotia Sea during the austral summers of 2000 and 2001 estimated by inverse methods. *Deep Sea Research Part I: Oceanographic Research Papers*, *54*(10), 1815–1840. https://doi.org/10.1016/j.dsr.2007.06.003

Frölicher, T. L., Sarmiento, J. L., Paynter, D. J., Dunne, J. P., Krasting, J. P., & Winton, M. (2015). Dominance of the Southern Ocean in Anthropogenic Carbon

and Heat Uptake in CMIP5 Models. *Journal of Climate*, *28*(2), 862–886. https://doi.org/10.1175/JCLI-D-14-00117.1

Garabato, A. C. N., Stevens, D. P., Watson, A. J., & Roether, W. (2007). Short-circuiting of the overturning circulation in the Antarctic Circumpolar Current. *Nature*, *447*(7141), 194–197. https://doi.org/10.1038/nature05832

Gaspar, P., Grégoris, Y., & Lefevre, J.-M. (1990). A simple eddy kinetic energy model for simulations of the oceanic vertical mixing: Tests at station Papa and long-term upper ocean study site. *Journal of Geophysical Research: Oceans*, *95*(C9), 16179–16193. https://doi.org/10.1029/JC095iC09p16179

Gebbie, G., & Huybers, P. (2010). Total Matrix Intercomparison: A Method for Determining the Geometry of Water-Mass Pathways. *Journal of Physical Oceanography*, *40*(8), 1710–1728. https://doi.org/10.1175/2010JPO4272.1

Gent, P. R., & McWilliams, J. C. (1990). Isopycnal Mixing in Ocean Circulation Models. *Journal of Physical Oceanography*. https://doi.org/10.1175/1520-0485(1990)020<0150:imiocm>2.0.co;2

Giles, K. A., Laxon, S. W., Ridout, A. L., Wingham, D. J., & Bacon, S. (2012). Western Arctic Ocean freshwater storage increased by wind-driven spin-up of the Beaufort Gyre. *Nature Geoscience*, *5*(3), 194–197. https://doi.org/10.1038/ngeo1379

Gill, A. E., & Niller, P. P. (1973). The theory of the seasonal variability in the ocean. *Deep Sea Research and Oceanographic Abstracts*, *20*(2), 141–177. https://doi.org/10.1016/0011-7471(73)90049-1

Gordon, A. L., Martinson, D. G., & Taylor, H. W. (1981). The wind-driven circulation in the Weddell-Enderby Basin. *Deep Sea Research Part A, Oceanographic Research Papers*, *28*(2), 151–163. https://doi.org/10.1016/0198-0149(81)90087-X

Griffies, S. M., Adcroft, A., & Hallberg, R. W. (2020). A Primer on the Vertical Lagrangian-Remap Method in Ocean Models Based on Finite Volume Generalized Vertical Coordinates. *Journal of Advances in Modeling Earth Systems*, *12*(10), 1–38. https://doi.org/10.1029/2019MS001954

Griffies, S. M., Pacanowski, R. C., & Hallberg, R. W. (2000). Spurious Diapycnal Mixing Associated with Advection in a z-Coordinate Ocean Model. *Monthly Weather Review*, *128*(3), 538–564. https://doi.org/10.1175/1520-0493(2000)128<0538:SDMAWA>2.0.CO;2

Gruber, N., Gloor, M., Mikaloff Fletcher, S. E., Doney, S. C., Dutkiewicz, S., Follows, M. J., Gerber, M., Jacobson, A. R., Joos, F., Lindsay, K., Menemenlis, D., Mouchet, A., Müller, S. A., Sarmiento, J. L., & Takahashi, T. (2009). Oceanic sources, sinks, and transport of atmospheric CO2. *Global Biogeochemical Cycles*, *23*(1). https://doi.org/10.1029/2008GB003349

Gula, J., Molemaker, M. J., & McWilliams, J. C. (2015). Gulf stream dynamics along the southeastern U.S. seaboard. *Journal of Physical Oceanography*, *45*(3), 690–715. https://doi.org/10.1175/JPO-D-14-0154.1

Guo, Y., Bishop, S., Bryan, F., & Bachman, S. (2022). A Global Diagnosis of Eddy Potential Energy Budget in an Eddy-Permitting Ocean Model. *Journal of Physical Oceanography*, *52*(8), 1731–1748. https://doi.org/10.1175/JPO-D-22-0029.1

Haid, V., & Timmermann, R. (2013). Simulated heat flux and sea ice production at coastal polynyas in the southwestern Weddell Sea. *Journal of Geophysical Research: Oceans*, *118*(5), 2640–2652. https://doi.org/10.1002/jgrc.20133

Hallberg, R. (2013). Using a resolution function to regulate parameterizations of oceanic mesoscale eddy effects. *Ocean Modelling*, *72*, 92–103. https://doi.org/10.1016/j.ocemod.2013.08.007

Hanawa, K., & D.Talley, L. (2001). Chapter 5.4 Mode waters. In G. Siedler, J. Church, & J. Gould (Eds.), *International Geophysics* (pp. 373–386, Vol. 77). Academic Press. https://doi.org/10.1016/S0074-6142(01)80129-7

Hattermann, T. (2018). Antarctic Thermocline Dynamics along a Narrow Shelf with Easterly Winds. *Journal of Physical Oceanography*, *48*(10), 2419–2443. https://doi.org/10.1175/JPO-D-18-0064.1

Hecht, M. W. (2010). Cautionary tales of persistent accumulation of numerical error: Dispersive centered advection. *Ocean Modelling*, *35*(3), 270–276. https://doi.org/10.1016/j.ocemod.2010.07.005

Hetland, R. (2017). Suppression of baroclinic instabilities in buoyancy-driven flow over sloping bathymetry. *Journal of Physical Oceanography*, *47*(1), 49–68. https://doi.org/10.1175/JPO-D-15-0240.1

Heuzé, C., Ridley, J. K., Calvert, D., Stevens, D. P., & Heywood, K. J. (2015). Increasing vertical mixing to reduce Southern Ocean deep convection in NEMO3.4. *Geoscientific Model Development*, *8*(10), 3119–3130. https://doi.org/10.5194/gmd-8-3119-2015

Heuzé, C. (2021). Antarctic Bottom Water and North Atlantic Deep Water in CMIP6 models. *Ocean Science*, *17*(1), 59–90. https://doi.org/10.5194/os-17-59-2021

Heuzé, C., Heywood, K. J., Stevens, D. P., & Ridley, J. K. (2013). Southern Ocean bottom water characteristics in CMIP5 models. *Geophysical Research Letters*, *40*(7), 1409–1414. https://doi.org/10.1002/grl.50287

Hewitt, H. T., Roberts, M., Mathiot, P., Biastoch, A., Blockley, E., Chassignet, E. P., Fox-Kemper, B., Hyder, P., Marshall, D. P., Popova, E., Treguier, A.-M., Zanna, L., Yool, A., Yu, Y., Beadling, R., Bell, M., Kuhlbrodt, T., Arsouze, T., Bellucci, A., ... Zhang, Q. (2020). Resolving and Parameterising the Ocean Mesoscale in Earth System Models. *Current Climate Change Reports*, *6*(4), 137–152. https://doi.org/10.1007/s40641-020-00164-w

Holloway, G. (1987). Systematic forcing of large-scale geophysical flows by eddy-topography interaction. *Journal of Fluid Mechanics*, *184*, 463–476. https://doi.org/10.1017/S0022112087002970

Holloway, G. (1992). Representing Topographic Stress for Large-Scale Ocean Models. *Journal of Physical Oceanography*, *22*(9), 1033–1046. https://doi.org/10.1175/1520-0485(1992)022<1033:RTSFLS>2.0.CO;2

Hughes, C. W., & de Cuevas, B. A. (2001). Why western boundary currents in realistic oceans are inviscid: A link between form stress and bottom pressure torques. *Journal of Physical Oceanography*, *31*(10), 2871–2885. https://doi.org/10.1175/1520-0485(2001)031<2871:WWBCIR>2.0.CO;2

Isachsen, P. E. (2011). Baroclinic instability and eddy tracer transport across sloping bottom topography: How well does a modified Eady model do in primitive equation simulations? *Ocean Modelling*, *39*(1), 183–199. https://doi.org/10.1016/j.ocemod.2010.09.007

Jackson, L., Hughes, C. W., & Williams, R. G. (2006). Topographic control of basin and channel flows: The role of bottom pressure torques and friction. *Journal of Physical Oceanography*, *36*(9), 1786–1805. https://doi.org/10.1175/JPO2936.1

Jagannathan, A., Srinivasan, K., McWilliams, J. C., Molemaker, M. J., & Stewart, A. L. (2021). Boundary layer-mediated vorticity generation in currents over sloping bathymetry. *Journal of Physical Oceanography*, 1757–1778. https://doi.org/10.1175/jpo-d-20-0253.1

Johnson, G. C., & Bryden, H. L. (1989). On the size of the Antarctic Circumpolar Current. *Deep Sea Research Part A. Oceanographic Research Papers*, *36*(1), 39–53. https://doi.org/10.1016/0198-0149(89)90017-4

Jones, D. C., Boland, E., Meijers, A. J., Forget, G., Josey, S. A., Sallee, J.-B., & Shuckburgh, E. (2019). Heat Distribution in the Southeast Pacific Is Only Weakly Sensitive to High-Latitude Heat Flux and Wind Stress. *Journal of Geophysical Research: Oceans*, *124*(12), 8647–8666. https://doi.org/10.1029/2019JC015460

Jones, D. C., Meijers, A. J. S., Shuckburgh, E., Sallée, J.-B., Haynes, P., McAufield, E. K., & Mazloff, M. R. (2016). How does Subantarctic Mode Water ventilate the Southern Hemisphere subtropics? *Journal of Geophysical Research: Oceans*, *121*(9), 6558–6582. https://doi.org/10.1002/2016JC011680

Jullion, L., Garabato, A. C. N., Bacon, S., Meredith, M. P., Brown, P. J., Torres-Valdés, S., Speer, K. G., Holland, P. R., Dong, J., Bakker, D., Hoppema, M., Loose, B., Venables, H. J., Jenkins, W. J., Messias, M.-J., & Fahrbach, E. (2014). The contribution of the Weddell Gyre to the lower limb of the Global Overturning Circulation. *Journal of Geophysical Research: Oceans*, *119*(6), 3357–3377. https://doi.org/10.1002/2013JC009725

Kamenkovich, I., Garraffo, Z., Pennel, R., & Fine, R. A. (2017). Importance of mesoscale eddies and mean circulation in ventilation of the Southern Ocean. *Journal of Geophysical Research: Oceans*, *122*(4), 2724–2741. https://doi.org/10.1002/2016JC012292

Katsumata, K., Purkey, S. G., Cowley, R., Sloyan, B. M., Diggs, S. C., Moore, T. S., Talley, L. D., & Swift, J. H. (2022). GO-SHIP Easy Ocean: Gridded ship-based hydrographic section of temperature, salinity, and dissolved oxygen. *Scientific Data*, *9*(1), 103. https://doi.org/10.1038/s41597-022-01212-w

Khatiwala, S., Tanhua, T., Mikaloff Fletcher, S., Gerber, M., Doney, S. C., Graven, H. D., Gruber, N., McKinley, G. A., Murata, A., Ríos, A. F., & Sabine, C. L. (2013). Global ocean storage of anthropogenic carbon. *Biogeosciences*, *10*(4), 2169–2191. https://doi.org/10.5194/bg-10-2169-2013

Kimura, N. (2004). Sea Ice Motion in Response to Surface Wind and Ocean Current in the Southern Ocean. *Journal of the Meteorological Society of Japan. Ser. II*, *82*(4), 1223–1231. https://doi.org/10.2151/JMSJ.2004.1223

Kiss, A. E., Hogg, A. M., Hannah, N., Boeira Dias, F., Brassington, G. B., Chamberlain, M. A., Chapman, C., Dobrohotoff, P., Domingues, C. M., Duran, E. R., England, M. H., Fiedler, R., Griffies, S. M., Heerdegen, A., Heil, P., Holmes, R. M., Klocker, A., Marsland, S. J., Morrison, A. K., … Zhang, X. (2020). ACCESS-OM2 v1.0: A global ocean–sea ice model at three resolutions. *Geoscientific Model Development*, *13*(2), 401–442. https://doi.org/10.5194/gmd-13-401-2020

Klatt, O., Fahrbach, E., Hoppema, M., & Rohardt, G. (2005). The transport of the Weddell Gyre across the Prime Meridian. *Deep Sea Research Part II: Topical Studies in Oceanography*, *52*(3), 513–528. https://doi.org/10.1016/j.dsr2.2004.12.015

Koenig, Z., Provost, C., Ferrari, R., Sennéchael, N., & Rio, M.-H. (2014). Volume transport of the Antarctic Circumpolar Current: Production and validation of a 20 year long time series obtained from in situ and satellite observations. *Journal of Geophysical Research: Oceans*, *119*(8), 5407–5433. https://doi.org/10.1002/2014JC009966

Kwok, R., Pang, S. S., & Kacimi, S. (2017). Sea ice drift in the Southern Ocean: Regional patterns, variability, and trends. *Elementa*, *5*, 32. https://doi.org/10.1525/ELEMENTA.226/112431

Kwon, E. Y. (2013). Temporal variability of transformation, formation, and subduction rates of upper Southern Ocean waters. *Journal of Geophysical Research: Oceans*, *118*(11), 6285–6302. https://doi.org/10.1002/2013JC008823

Large, W. G., & Yeager, S. G. (2009). The global climatology of an interannually varying air - Sea flux data set. *Climate Dynamics*, *33*(2-3), 341–364. https://doi.org/10.1007/s00382-008-0441-3

Le Bras, I. A. A., Sonnewald, M., & Toole, J. M. (2019). A barotropic vorticity budget for the subtropical north atlantic based on observations. *Journal of Physical Oceanography*, *49*(11), 2781–2797. https://doi.org/10.1175/JPO-D-19-0111.1

Le Corre, M., Gula, J., & Tréguier, A. M. (2020). Barotropic vorticity balance of the North Atlantic subpolar gyre in an eddy-resolving model. *Ocean Science*. https://doi.org/10.5194/os-16-451-2020

Leach, H., Strass, V., & Cisewski, B. (2011). Modification by lateral mixing of the Warm Deep Water entering the Weddell Sea in the Maud Rise region. *Ocean Dynamics*, *61*(1), 51–68. https://doi.org/10.1007/s10236-010-0342-y

Lee, M.-M., Coward, A. C., & Nurser, A. J. G. (2002). Spurious Diapycnal Mixing of the Deep Waters in an Eddy-Permitting Global Ocean Model. *Journal of Physical Oceanography*, *32*(5), 1522–1535. https://doi.org/10.1175/1520-0485(2002)032<1522:SDMOTD>2.0.CO;2

Lemarié, F., Debreu, L., Shchepetkin, A. F., & McWilliams, J. C. (2012a). On the stability and accuracy of the harmonic and biharmonic isoneutral mixing operators in ocean models. *Ocean Modelling*, *52–53*, 9–35. https://doi.org/10.1016/J.OCEMOD.2012.04.007

Lemarié, F., Kurian, J., Shchepetkin, A. F., Jeroen Molemaker, M., Colas, F., & McWilliams, J. C. (2012b). Are there inescapable issues prohibiting the use of terrain-following coordinates in climate models? *Ocean Modelling*, *42*, 57–79. https://doi.org/10.1016/j.ocemod.2011.11.007

Lévy, M., Klein, P., Tréguier, A. M., Iovino, D., Madec, G., Masson, S., & Takahashi, K. (2010). Modifications of gyre circulation by sub-mesoscale physics. *Ocean Modelling*, *34*(1-2), 1–15. https://doi.org/10.1016/j.ocemod.2010.04.001

Lévy, M., Jahn, O., Dutkiewicz, S., Follows, M. J., & D'Ovidio, F. (2015). The dynamical landscape of marine phytoplankton diversity. *Journal of the Royal Society Interface*. https://doi.org/10.1098/rsif.2015.0481

Li, Q., England, M. H., Hogg, A. M., Rintoul, S. R., & Morrison, A. K. (2023). Abyssal ocean overturning slowdown and warming driven by Antarctic meltwater. *Nature*, *615*(7954), 841–847. https://doi.org/10.1038/s41586-023-05762-w

Liu, L. L., & Huang, R. X. (2012). The Global Subduction/Obduction Rates: Their Interannual and Decadal Variability. *Journal of Climate*, *25*(4), 1096–1115. https://doi.org/10.1175/2011JCLI4228.1

Lohmann, K., Drange, H., & Bentsen, M. (2009). Response of the North Atlantic subpolar gyre to persistent North Atlantic oscillation like forcing. *Climate Dynamics*, *32*(2), 273–285. https://doi.org/10.1007/s00382-008-0467-6

Lumpkin, R., & Speer, K. (2007). Global Ocean Meridional Overturning. *Journal of Physical Oceanography*, *37*(10), 2550–2562. https://doi.org/10.1175/JPO3130.1

MacGilchrist, G. A., Johnson, H. L., Lique, C., & Marshall, D. P. (2021). Demons in the North Atlantic: Variability of Deep Ocean Ventilation. *Geophysical Research Letters*, *48*(9), 1–9. https://doi.org/10.1029/2020GL092340

MacGilchrist, G. A., Johnson, H. L., Marshall, D. P., Lique, C., Thomas, M., Jackson, L. C., & Wood, R. A. (2020). Locations and Mechanisms of Ocean Ventilation in the High-Latitude North Atlantic in an Eddy-Permitting Ocean Model. *Journal of Climate*, *33*(23), 10113–10131. https://doi.org/10.1175/JCLI-D-20-0191.1

MacGilchrist, G. A., Naveira Garabato, A. C., Brown, P. J., Jullion, L., Bacon, S., Bakker, D. C. E., Hoppema, M., Meredith, M. P., & Torres-Valdés, S. (2019). Reframing the carbon cycle of the subpolar Southern Ocean. *Science Advances*, *5*(8), eaav6410. https://doi.org/10.1126/sciadv.aav6410

Madec, G., Bourdallé-Badie, R., Chanut, J., Samson, E. C., Coward, A., Ethé, C., Iovino, D., Lea, D., Lévy, C., Lovato, T., Martin, N., Masson, S., Mocavero, S., Rousset, C., Storkey, D., Vancoppenolle, M., Müeller, S., Nurser, G., Bell, M., & Samson, G. (2019). NEMO ocean engine. https://doi.org/10.5281/zenodo.1464816

Madec, G., & Imbard, M. (1996). A global ocean mesh to overcome the North Pole singularity. *Climate Dynamics*, *12*(6), 381–388. https://doi.org/10.1007/BF00211684

Marshall, D. (1997). Subduction of water masses in an eddying ocean. *Journal of Marine Research*, *55*(2), 201–222. https://doi.org/10.1357/0022240973224373

Marshall, D. P., Ambaum, M. H., Maddison, J. R., Munday, D. R., & Novak, L. (2017). Eddy saturation and frictional control of the Antarctic Circumpolar Current. *Geophysical Research Letters*, *44*(1), 286–292. https://doi.org/10.1002/2016GL071702

Marshall, D. P., & Pillar, H. R. (2011). Momentum balance of the wind-driven and meridional overturning circulation. *Journal of Physical Oceanography*, *41*(5), 960–978. https://doi.org/10.1175/2010JPO4528.1

Marshall, J., & Speer, K. (2012). Closure of the meridional overturning circulation through Southern Ocean upwelling. *Nature Geoscience*, *5*(3), 171–180. https://doi.org/10.1038/ngeo1391

Marshall, J. C., Williams, R. G., & Nurser, A. J. G. (1993). Inferring the Subduction Rate and Period over the North Atlantic. *Journal of Physical Oceanography*, *23*(7), 1315–1329. https://doi.org/10.1175/1520-0485(1993)023<1315:ITSRAP>2.0.CO;2

Martinson, D. G. (1990). Evolution of the southern ocean winter mixed layer and sea ice: Open ocean deepwater formation and ventilation. *Journal of Geophysical Research: Oceans*, *95*(C7), 11641–11654. https://doi.org/10.1029/JC095iC07p11641

Mazloff, M. R., Heimbach, P., & Wunsch, C. (2010). An Eddy-Permitting Southern Ocean State Estimate. *Journal of Physical Oceanography*, *40*(5), 880–899. https://doi.org/10.1175/2009JPO4236.1

McCartney, M. S. (1979). Subantarctic Mode Water. *Woods Hole Oceanographic Institution Contribution*, *3773*, 103–119.

McDougall, T. J., & Barker, P. M. (2011). Getting started with TEOS-10 and the Gibbs Seawater (GSW) oceanographic toolbox. *SCOR/IAPSO WG*, *127*, 1–28.

Mechoso, C. R. (1980). Baroclinic Instability of Flows Along Sloping Boundaries. *Journal of the Atmospheric Sciences*, *37*(6), 1393–1399. https://doi.org/10.1175/1520-0469(1980)037<1393:BIOFAS>2.0.CO;2

Megann, A. (2018). Estimating the numerical diapycnal mixing in an eddy-permitting ocean model. *Ocean Modelling*, *121*, 19–33. https://doi.org/10.1016/j.ocemod.2017.11.001

Meijers, A. J., Meredith, M. P., Abrahamsen, E. P., Morales Maqueda, M. A., Jones, D. C., & Naveira Garabato, A. C. (2016). Wind-driven export of Weddell Sea slope water. *Journal of Geophysical Research: Oceans*. https://doi.org/10.1002/2016JC011757

Meredith, M., Sommerkorn, M., Cassota, S., Derksen, C., Ekaykin, A., Hollowed, A., Kofinas, G., Mackintosh, A., Melbourne-Thomas, J., Muelbert, M. M. C., Ottersen, G., Pritchard, H., & Schuur, E. A. G. (2022). Polar regions. In H.-O. Pörtner, D. C. Roberts, V. Masson-Delmotte, P. Zhai, M. Tignor, E. Poloczanska, K. Mintenbeck, A. Alegría, M. Nicolai, A. Okem, J. Petzold, B. Rama, & N. M. Weyer (Eds.), *IPCC Special Report on the Ocean and Cryosphere in a Changing Climate* (pp. 203–320). Cambridge University Press. https://doi.org/10.1017/9781009157964.005

Mesinger, F., & Arakawa, A. (1976). Numerical methods used in atmospheric models. *GARP Publications Series, 17 . Global Atmospheric Research Programme (GARP), 64 pp.*

Morrison, A. K., Waugh, D. W., Hogg, A. M., Jones, D. C., & Abernathey, R. P. (2022). Ventilation of the Southern Ocean Pycnocline. *Annual Review of Marine Science*, *14*(1), 405–430. https://doi.org/10.1146/annurev-marine-010419-011012

Nasser, A.-A., Madec, G., de Lavergne, C., Debreu, L., Lemarié, F., & Blayo, E. (2023). Sliding or Stumbling on the Staircase: Numerics of Ocean Circulation Along Piecewise-Constant Coastlines. *Journal of Advances in Modeling Earth Systems*, *15*(5), e2022MS003594. https://doi.org/10.1029/2022MS003594

Naveira Garabato, A. C., McDonagh, E. L., Stevens, D. P., Heywood, K. J., & Sanders, R. J. (2002). On the export of Antarctic Bottom Water from the Weddell Sea. *Deep Sea Research Part II: Topical Studies in Oceanography*, *49*(21), 4715–4742. https://doi.org/10.1016/S0967-0645(02)00156-X

Naveira Garabato, A. C., Williams, A. P., & Bacon, S. (2014). The three-dimensional overturning circulation of the Southern Ocean during the WOCE era. *Progress in Oceanography*, *120*, 41–78. https://doi.org/10.1016/j.pocean.2013.07.018

Naveira Garabato, A. C., Zika, J. D., Jullion, L., Brown, P. J., Holland, P. R., Meredith, M. P., & Bacon, S. (2016). The thermodynamic balance of the Weddell Gyre. *Geophysical Research Letters*, *43*(1), 317–325. https://doi.org/10.1002/2015GL066658

Neme, J., England, M. H., & Hogg, A. M. C. (2021). Seasonal and Interannual Variability of the Weddell Gyre From a High-Resolution Global Ocean-Sea Ice Simulation During 1958–2018. *Journal of Geophysical Research: Oceans*, *126*(11), 1–19. https://doi.org/10.1029/2021JC017662

Neme, J., England, M. H., Hogg, A. M., Khatri, H., & Griffies, S. M. (2023). The role of bottom friction in mediating the response of the Weddell Gyre circulation to changes in surface stress and buoyancy fluxes. https://doi.org/10.22541/essoar.169228895.55803191/v1

Nicholls, K. W., Østerhus, S., Makinson, K., Gammelsrød, T., & Fahrbach, E. (2009). Ice-ocean processes over the continental shelf of the southern Weddell Sea, Antarctica: A review. *Reviews of Geophysics*, *47*(3). https://doi.org/10.1029/2007RG000250

Niiler, P. P. (1966). On the theory of wind-driven ocean circulation. *Deep-Sea Research and Oceanographic Abstracts*, *13*(4), 597–606. https://doi.org/10.1016/0011-7471(66)90591-2

Orsi, A. H., Johnson, G. C., & Bullister, J. L. (1999). Circulation, mixing, and production of Antarctic Bottom Water. *Progress in Oceanography*, *43*(1), 55–109. https://doi.org/10.1016/S0079-6611(99)00004-X

Orsi, A. H., Nowlin, W. D., & Whitworth, T. (1993). On the circulation and stratification of the Weddell Gyre. *Deep Sea Research Part I: Oceanographic Research Papers*, *40*(1), 169–203. https://doi.org/10.1016/0967-0637(93)90060-G

Orsi, A. H., Smethie Jr., W. M., & Bullister, J. L. (2002). On the total input of Antarctic waters to the deep ocean: A preliminary estimate from chlorofluorocarbon measurements. *Journal of Geophysical Research: Oceans*, *107*(C8), 31-1-31–14. https://doi.org/10.1029/2001JC000976

Orsi, A. H., Whitworth, T., & Nowlin, W. D. (1995). On the meridional extent and fronts of the Antarctic Circumpolar Current. *Deep Sea Research Part I: Oceanographic Research Papers*, *42*(5), 641–673. https://doi.org/10.1016/0967-0637(95)00021-W

Pardo, P. C., Pérez, F. F., Velo, A., & Gilcoto, M. (2012). Water masses distribution in the Southern Ocean: Improvement of an extended OMP (eOMP) analysis. *Progress in Oceanography*, *103*, 92–105. https://doi.org/10.1016/j.pocean.2012.06.002

Park, Y.-H., Charriaud, E., Craneguy, P., & Kartavtseff, A. (2001). Fronts, transport, and Weddell Gyre at 30°E between Africa and Antarctica. *Journal of Geophysical Research: Oceans*, *106*(C2), 2857–2879. https://doi.org/10.1029/2000JC900087

Patterson, S. L., & Sievers, H. A. (1980). The Weddell-Scotia Confluence. *Journal of Physical Oceanography*, *10*(10), 1584–1610. https://doi.org/10.1175/1520-0485(1980)010<1584:TWSC>2.0.CO;2

Pellichero, V., Sallée, J. B., Chapman, C. C., & Downes, S. M. (2018). The southern ocean meridional overturning in the sea-ice sector is driven by freshwater fluxes. *Nature Communications*, *9*(1), 1–9. https://doi.org/10.1038/s41467-018-04101-2

Perezhogin, P. (2019). Deterministic and stochastic parameterizations of kinetic energy backscatter in the NEMO ocean model in Double-Gyre configuration. *IOP Conference Series: Earth and Environmental Science*. https://doi.org/10.1088/1755-1315/386/1/012025

Petit, T., Lozier, M. S., Josey, S. A., & Cunningham, S. A. (2020). Atlantic Deep Water Formation Occurs Primarily in the Iceland Basin and Irminger Sea by Local Buoyancy Forcing. *Geophysical Research Letters*, *47*(22), e2020GL091028. https://doi.org/10.1029/2020GL091028

Phillips, N. A. (1954). Energy Transformations and Meridional Circulations associated with simple Baroclinic Waves in a two-level, Quasi-geostrophic Model. *Tellus*, *6*(3), 274–286. https://doi.org/10.3402/tellusa.v6i3.8734

Purich, A., & England, M. H. (2021). Historical and Future Projected Warming of Antarctic Shelf Bottom Water in CMIP6 Models. *Geophysical Research Letters*, *48*(10), e2021GL092752. https://doi.org/10.1029/2021GL092752

Purkey, S. G., & Johnson, G. C. (2010). Warming of Global Abyssal and Deep Southern Ocean Waters between the 1990s and 2000s: Contributions to Global Heat and Sea Level Rise Budgets. *Journal of Climate*, *23*(23), 6336–6351. https://doi.org/10.1175/2010JCLI3682.1

Purkey, S. G., Smethie, W. M., Gebbie, G., Gordon, A. L., Sonnerup, R. E., Warner, M. J., & Bullister, J. L. (2018). A Synoptic View of the Ventilation and Circulation of Antarctic Bottom Water from Chlorofluorocarbons and Natural Tracers. *Annual Review of Marine Science*, *10*(1), 503–527. https://doi.org/10.1146/annurev-marine-121916-063414

Reeve, K. A., Boebel, O., Strass, V., Kanzow, T., & Gerdes, R. (2019). Horizontal circulation and volume transports in the Weddell Gyre derived from Argo float data. *Progress in Oceanography*, *175*(August 2017), 263–283. https://doi.org/10.1016/j.pocean.2019.04.006

Reintges, A., Martin, T., Latif, M., & Park, W. (2017). Physical controls of Southern Ocean deep-convection variability in CMIP5 models and the Kiel Climate Model. *Geophysical Research Letters*, *44*(13), 6951–6958. https://doi.org/10.1002/2017GL074087

Rintoul, S. R., Hughes, C. W., & Olbers, D. (2001). Chapter 4.6 The antarctic circumpolar current system. In G. Siedler, J. Church, & J. Gould (Eds.), *International Geophysics* (pp. 271–XXXVI, Vol. 77). Academic Press. https://doi.org/10.1016/S0074-6142(01)80124-8

Roberts, M. J., Baker, A., Blockley, E. W., Calvert, D., Coward, A., Hewitt, H. T., Jackson, L. C., Kuhlbrodt, T., Mathiot, P., Roberts, C. D., Schiemann, R., Seddon, J., Vannière, B., & Vidale, P. L. (2019). Description of the resolution hierarchy of the global coupled HadGEM3-GC3.1 model as used in CMIP6 HighResMIP experiments. *Geoscientific Model Development*, *12*(12), 4999–5028. https://doi.org/10.5194/gmd-12-4999-2019

Ruggiero, G. A., Ourmières, Y., Cosme, E., Blum, J., Auroux, D., & Verron, J. (2015). Data assimilation experiments using diffusive back-and-forth nudging for the NEMO ocean model. *Nonlinear Processes in Geophysics*. https://doi.org/10.5194/npg-22-233-2015

Ryan, S., Schröder, M., Huhn, O., & Timmermann, R. (2016). On the warm inflow at the eastern boundary of the Weddell Gyre. *Deep Sea Research Part I: Oceanographic Research Papers*, *107*, 70–81. https://doi.org/10.1016/j.dsr.2015.11.002

Sabine, C. L., Feely, R. A., Gruber, N., Key, R. M., Lee, K., Bullister, J. L., Wanninkhof, R., Wong, C. S., Wallace, D. W. R., Tilbrook, B., Millero, F. J., Peng, T.-H., Kozyr, A., Ono, T., & Rios, A. F. (2004). The Oceanic Sink for Anthropogenic CO2. *Science*, *305*(5682), 367–371. https://doi.org/10.1126/science.1097403

Sadourny, R. (1975). The Dynamics of Finite-Difference Models of the Shallow-Water Equations. *Journal of Atmospheric Sciences*, *32*(4), 680–689. https://doi.org/10.1175/1520-0469(1975)032<0680:TDOFDM>2.0.CO;2

Sallée, J.-B., Morrow, R., & Speer, K. (2008). Eddy heat diffusion and Subantarctic Mode Water formation. *Geophysical Research Letters*, *35*(5). https://doi.org/10.1029/2007GL032827

Sallée, J.-B., Matear, R. J., Rintoul, S. R., & Lenton, A. (2012). Localized subduction of anthropogenic carbon dioxide in the Southern Hemisphere oceans. *Nature Geoscience*, *5*(8), 579–584. https://doi.org/10.1038/ngeo1523

Sallée, J.-B., Speer, K., Rintoul, S., & Wijffels, S. (2010). Southern Ocean Thermocline Ventilation. *Journal of Physical Oceanography*, *40*(3), 509–529. https://doi.org/10.1175/2009JPO4291.1

Sarmiento, J. L., Gruber, N., Brzezinski, M. A., & Dunne, J. P. (2004). High-latitude controls of thermocline nutrients and low latitude biological productivity. *Nature*, *427*(6969), 56–60. https://doi.org/10.1038/nature02127

Schoonover, J., Dewar, W., Wienders, N., Gula, J., McWilliams, J. C., Molemaker, M. J., Bates, S. C., Danabasoglu, G., & Yeager, S. (2016). North Atlantic barotropic vorticity balances in numerical models. *Journal of Physical Oceanography*. https://doi.org/10.1175/JPO-D-15-0133.1

Schröder, M., & Fahrbach, E. (1999). On the structure and the transport of the eastern Weddell Gyre. *Deep Sea Research Part II: Topical Studies in Oceanography*, *46*(1), 501–527. https://doi.org/10.1016/S0967-0645(98)00112-X

Sloyan, B. M., & Rintoul, S. R. (2001). The Southern Ocean Limb of the Global Deep Overturning Circulation. *Journal of Physical Oceanography*, *31*(1), 143–173. https://doi.org/10.1175/1520-0485(2001)031<0143:TSOLOT>2.0.CO;2

Solodoch, A., Stewart, A. L., Hogg, A. M., Morrison, A. K., Kiss, A. E., Thompson, A. F., Purkey, S. G., & Cimoli, L. (2022). How Does Antarctic Bottom Water Cross the Southern Ocean? *Geophysical Research Letters*, *49*(7), e2021GL097211. https://doi.org/10.1029/2021GL097211

Song, Y. T., & Wright, D. G. (1998). A General Pressure Gradient Formulation for Ocean Models. Part II: Energy, Momentum, and Bottom Torque Consistency. *Monthly Weather Review*, *126*(12), 3231–3247. https://doi.org/10.1175/1520-0493(1998)126<3231:AGPGFF>2.0.CO;2

Song, Y., & Haidvogel, D. (1994). A Semi-implicit Ocean Circulation Model Using a Generalized Topography-Following Coordinate System. *Journal of Computational Physics*, *115*(1), 228–244. https://doi.org/10.1006/jcph.1994.1189

Sonnewald, M., Reeve, K. A., & Lguensat, R. (2023). A Southern Ocean supergyre as a unifying dynamical framework identified by physics-informed machine learning. *Communications Earth & Environment*, *4*(1), 1–20. https://doi.org/10.1038/s43247-023-00793-7

Speer, K., Rintoul, S. R., & Sloyan, B. (2000). The Diabatic Deacon Cell. *Journal of Physical Oceanography*, *30*(12), 3212–3222. https://doi.org/10.1175/1520-0485(2000)030<3212:TDDC>2.0.CO;2

Spencer, K. (2022). OpenSimplex Noise.

Stanley, G. J., McDougall, T. J., & Barker, P. M. (2021). Algorithmic Improvements to Finding Approximately Neutral Surfaces. *Journal of Advances in Modeling Earth Systems*, *13*(5), e2020MS002436. https://doi.org/10.1029/2020MS002436

Stern, A., Nadeau, L.-P., & Holland, D. (2015). Instability and Mixing of Zonal Jets along an Idealized Continental Shelf Break. *Journal of Physical Oceanography*, *45*(9), 2315–2338. https://doi.org/10.1175/JPO-D-14-0213.1

Stewart, A. L., Klocker, A., & Menemenlis, D. (2019). Acceleration and Overturning of the Antarctic Slope Current by Winds, Eddies, and Tides. *Journal of Physical Oceanography*, *49*(8), 2043–2074. https://doi.org/10.1175/JPO-D-18-0221.1

Stewart, A. L., McWilliams, J. C., & Solodoch, A. (2021). On the Role of Bottom Pressure Torques in Wind-Driven Gyres. *Journal of Physical Oceanography*, *51*(5), 1441–1464. https://doi.org/10.1175/jpo-d-20-0147.1

Stommel, H. (1979). Determination of water mass properties of water pumped down from the Ekman layer to the geostrophic flow below. *Proceedings of the National Academy of Sciences*, *76*(7), 3051–3055. https://doi.org/10.1073/pnas.76.7.3051

Stommel, H. (1948). The westward intensification of wind-driven ocean currents. *Eos, Transactions American Geophysical Union*. https://doi.org/10.1029/TR029i002p00202

Storkey, D., Blaker, A. T., Mathiot, P., Megann, A., Aksenov, Y., Blockley, E. W., Calvert, D., Graham, T., Hewitt, H. T., Hyder, P., Kuhlbrodt, T., Rae, J. G., & Sinha, B. (2018). UK Global Ocean GO6 and GO7: A traceable hierarchy of model resolutions. *Geoscientific Model Development*, *11*(8), 3187–3213. https://doi.org/10.5194/gmd-11-3187-2018

Styles, A. F., Bell, M. J., Marshall, D. P., & Storkey, D. (2021). Data for "Spurious forces can dominate the vorticity budget of ocean gyres on the C-grid". https://doi.org/https://zenodo.org/doi/10.5281/zenodo.5513824

Styles, A. F., Bell, M. J., & Marshall, D. P. (2023a). Analysis software for "The Sensitivity of an Idealized Weddell Gyre to Horizontal Resolution". https://doi.org/10.5281/zenodo.7969645

Styles, A. F., Bell, M. J., & Marshall, D. P. (2023b). Data for "The Sensitivity of an Idealized Weddell Gyre to Horizontal Resolution". https://doi.org/10.5281/zenodo.7602478

Styles, A. F., Bell, M. J., & Marshall, D. P. (2023c). Model configuration for "The Sensitivity of an Idealized Weddell Gyre to Horizontal Resolution". https://doi.org/10.5281/zenodo.7969659

Styles, A. F., Bell, M. J., & Marshall, D. P. (2023d). The Sensitivity of an Idealized Weddell Gyre to Horizontal Resolution. *Journal of Geophysical Research: Oceans*, *128*(10), e2023JC019711. https://doi.org/10.1029/2023JC019711

Styles, A. F., Bell, M. J., Marshall, D. P., & Storkey, D. (2022). Spurious Forces Can Dominate the Vorticity Budget of Ocean Gyres on the C-Grid. *Journal of Advances in Modeling Earth Systems*, *14*(5), e2021MS002884. https://doi.org/10.1029/2021MS002884

Styles, A. F., MacGilchrist, G., Bell, M. J., & Marshall, D. P. (2023e). Analysis software for "Spatial and Temporal Patterns of Southern Ocean Ventilation". https://doi.org/10.5281/zenodo.8413773

Styles, A. F., MacGilchrist, G., Bell, M. J., & Marshall, D. P. (2023f). Data for "Spatial and Temporal patterns of Southern Ocean Ventilation". https://doi.org/https://zenodo.org/doi/10.5281/zenodo.8413705

Sun, J., Latif, M., & Park, W. (2021). Subpolar Gyre–AMOC–Atmosphere Interactions on Multidecadal Timescales in a Version of the Kiel Climate Model. *Journal of Climate*, *34*(16), 6583–6602. https://doi.org/10.1175/JCLI-D-20-0725.1

Sverdrup, H. U., Johnson, M. W., & Fleming, R. H. (1942). *The Oceans: Their physics, chemistry, and general biology* (Vol. 1087). New York: Prentice-Hall.

Talley, L. (2013). Closure of the Global Overturning Circulation Through the Indian, Pacific, and Southern Oceans: Schematics and Transports. *Oceanography*, *26*(1), 80–97. https://doi.org/10.5670/oceanog.2013.07

Talley, L. D., Reid, J. L., & Robbins, P. E. (2003). Data-Based Meridional Overturning Streamfunctions for the Global Ocean. *Journal of Climate*, *16*(19), 3213–3226. https://doi.org/10.1175/1520-0442(2003)016<3213:DMOSFT>2.0.CO;2

Thompson, A. F., & Heywood, K. J. (2008). Frontal structure and transport in the northwestern Weddell Sea. *Deep-Sea Research Part I: Oceanographic Research Papers*, *55*(10), 1229–1251. https://doi.org/10.1016/j.dsr.2008.06.001

Thompson, A. F., Stewart, A. L., Spence, P., & Heywood, K. J. (2018). The Antarctic Slope Current in a Changing Climate. *Reviews of Geophysics*, *56*(4), 741–770. https://doi.org/10.1029/2018RG000624

Ting, Y.-H., & Holzer, M. (2017). Decadal changes in Southern Ocean ventilation inferred from deconvolutions of repeat hydrographies. *Geophysical Research Letters*, *44*(11), 5655–5664. https://doi.org/10.1002/2017GL073788

Tooth, O. J., Johnson, H. L., Wilson, C., & Evans, D. G. (2023). Seasonal overturning variability in the eastern North Atlantic subpolar gyre: A Lagrangian perspective. *Ocean Science*, *19*(3), 769–791. https://doi.org/10.5194/os-19-769-2023

Turner, J., Phillips, T., Hosking, J. S., Marshall, G. J., & Orr, A. (2013). The Amundsen Sea low. *International Journal of Climatology*, *33*(7), 1818–1829. https://doi.org/10.1002/joc.3558

Vallis, G. K. (2017). Atmospheric and oceanic fluid dynamics: Fundamentals and large-scale circulation, second edition. *Atmospheric and Oceanic Fluid Dynamics: Fundamentals and Large-Scale Circulation, Second Edition*, 1–946. https://doi.org/10.1017/9781107588417

Van Der Walt, S., Schönberger, J. L., Nunez-Iglesias, J., Boulogne, F., Warner, J. D., Yager, N., Gouillart, E., & Yu, T. (2014). Scikit-image: Image processing in python. *PeerJ*, *2014*(1), e453. https://doi.org/10.7717/peerj.453

van Sebille, E., Griffies, S. M., Abernathey, R., Adams, T. P., Berloff, P., Biastoch, A., Blanke, B., Chassignet, E. P., Cheng, Y., Cotter, C. J., Deleersnijder, E., Döös, K., Drake, H. F., Drijfhout, S., Gary, S. F., Heemink, A. W., Kjellsson, J., Koszalka, I. M., Lange, M., … Zika, J. D. (2018). Lagrangian ocean analysis: Fundamentals and practices. *Ocean Modelling*, *121*, 49–75. https://doi.org/10.1016/j.ocemod.2017.11.008

Vernet, M., Geibert, W., Hoppema, M., Brown, P. J., Haas, C., Hellmer, H. H., Jokat, W., Jullion, L., Mazloff, M., Bakker, D. C., Brearley, J. A., Croot, P., Hattermann, T., Hauck, J., Hillenbrand, C. D., Hoppe, C. J., Huhn, O., Koch, B. P., Lechtenfeld, O. J., … Verdy, A. (2019). The Weddell Gyre, Southern Ocean: Present Knowledge and Future Challenges. *Reviews of Geophysics*, *57*(3), 623–708. https://doi.org/10.1029/2018RG000604

Wang, Z. (2013). On the response of Southern Hemisphere subpolar gyres to climate change in coupled climate models. *Journal of Geophysical Research: Oceans*, *118*(3), 1070–1086. https://doi.org/10.1002/jgrc.20111

Waugh, D. W., Hogg, A. M., Spence, P., England, M. H., & Haine, T. W. N. (2019). Response of Southern Ocean Ventilation to Changes in Midlatitude Westerly Winds. *Journal of Climate*, *32*(17), 5345–5361. https://doi.org/10.1175/JCLI-D-19-0039.1

Waugh, D. W., Primeau, F., DeVries, T., & Holzer, M. (2013). Recent Changes in the Ventilation of the Southern Oceans. *Science*, *339*(6119), 568–570. https://doi.org/10.1126/science.1225411

Wei, H., Wang, Y., Stewart, A. L., & Mak, J. (2022). Scalings for Eddy Buoyancy Fluxes Across Prograde Shelf/Slope Fronts. *Journal of Advances in Modeling Earth Systems*, *14*(12), e2022MS003229. https://doi.org/10.1029/2022MS003229

Willebrand, J., Barnier, B., Böning, C., Dieterich, C., Killworth, P. D., Le Provost, C., Jia, Y., Molines, J. M., & New, A. L. (2001). Circulation characteristics in three eddy-permitting models of the North Atlantic. *Progress in Oceanography*, *48*(2-3), 123–161. https://doi.org/10.1016/S0079-6611(01)00003-9

Williams, R. G., Marshall, J. C., & Spall, M. A. (1995). Does Stommel's Mixed Layer "Demon" Work? *Journal of Physical Oceanography*, *25*(12), 3089–3102. https://doi.org/10.1175/1520-0485(1995)025<3089:DSMLW>2.0.CO;2

Wilson, E. A., Riser, S. C., Campbell, E. C., & Wong, A. P. S. (2019). Winter Upper-Ocean Stability and Ice–Ocean Feedbacks in the Sea Ice–Covered Southern Ocean. *Journal of Physical Oceanography*, *49*(4), 1099–1117. https://doi.org/10.1175/JPO-D-18-0184.1

Wilson, E. A., Thompson, A. F., Stewart, A. L., & Sun, S. (2022). Bathymetric Control of Subpolar Gyres and the Overturning Circulation in the Southern Ocean. *Journal of Physical Oceanography*, *52*(2), 205–223. https://doi.org/10.1175/JPO-D-21-0136.1

Yaremchuk, M., Nechaev, D., Schroter, J., & Fahrbach, E. (1998). A dynamically consistent analysis of circulation and transports in the southwestern Weddell Sea. *Annales Geophysicae*, *16*(8), 1024–1038. https://doi.org/10.1007/s00585-998-1024-7

Yeager, S. (2015). Topographic coupling of the atlantic overturning and gyre circulations. *Journal of Physical Oceanography*. https://doi.org/10.1175/JPO-D-14-0100.1

Zhai, X., Johnson, H. L., & Marshall, D. P. (2010). Significant sink of ocean-eddy energy near western boundaries. *Nature Geoscience*, *3*(9), 608–612. https://doi.org/10.1038/ngeo943

Zhan, P., Subramanian, A. C., Yao, F., Kartadikaria, A. R., Guo, D., & Hoteit, I. (2016). The eddy kinetic energy budget in the Red Sea. *Journal of Geophysical Research: Oceans*, *121*(7), 4732–4747. https://doi.org/10.1002/2015JC011589

Zhang, R. (2008). Coherent surface-subsurface fingerprint of the Atlantic meridional overturning circulation. *Geophysical Research Letters*, *35*(20). https://doi.org/10.1029/2008GL035463

Zhou, S., Meijers, A. J. S., Meredith, M. P., Abrahamsen, E. P., Holland, P. R., Silvano, A., Sallée, J.-B., & Østerhus, S. (2023). Slowdown of Antarctic Bottom Water export driven by climatic wind and sea-ice changes. *Nature Climate Change*, *13*(7), 701–709. https://doi.org/10.1038/s41558-023-01695-4

Zika, J. D., Sloyan, B. M., & McDougall, T. J. (2009). Diagnosing the Southern Ocean Overturning from Tracer Fields. *Journal of Physical Oceanography*, *39*(11), 2926–2940. https://doi.org/10.1175/2009JPO4052.1

Zuo, H., Balmaseda, M. A., Tietsche, S., Mogensen, K., & Mayer, M. (2019). The ECMWF operational ensemble reanalysis–analysis system for ocean and sea ice: A description of the system and assessment. *Ocean Science*, *15*(3), 779–808. https://doi.org/10.5194/os-15-779-2019